CHIRAL SPIN GLASSES, CONTINUUM OF DEVIL'S STAIRCASES, AND THRESHOLDED ROUGHENING FROM FROZEN IMPURITIES

by

TOLGA ÇAĞLAR

Submitted to the Graduate School of Engineering and Natural Sciences
in partial fulfillment of
the requirements for the degree of
Doctor of Philosophy

Sabancı University
June 2017

Chiral Spin Glasses, Continuum of Devil's Staircases, and Thresholded
Roughening from Frozen Impurities

APPROVED BY:

Prof. Dr. A. Nihat Berker
(Thesis Supervisor) A. Nihat Berker

Prof. Dr. Bandan Durukanoglu Feyiz
Bandan D. Fay

Asst. Prof. Dr. KAMER KAYA
KAYA

Assoc. Prof. Dr. Haluk Özbek
ÖZBEK

Prof. Dr. MEHRAN KARDAR
Mehran Kardar

DATE OF APPROVAL: 22 / 06 / 2017

ABSTRACT

CHIRAL SPIN GLASSES, CONTINUUM OF DEVIL'S STAIRCASES, AND THRESHOLDED ROUGHENING FROM FROZEN IMPURITIES

TOLGA ÇAĞLAR

PhD Dissertation, June 2017

Thesis Supervisor: Prof. A. Nihat Berker

Keywords: Quenched random systems, chiral spin glass, renormalization-group theory, interface roughening, devil's staircases

The roughening phase diagram of the three-dimensional Ising model with uniaxially anisotropic interactions is calculated for the entire range of anisotropy, using hard-spin mean-field theory. Quenched random pinning centers and missing bonds on the interface of isotropic and anisotropic Ising models show domain boundary roughening that exhibits consecutive thresholding transitions as a function of interaction anisotropy. Quenched random chirality is introduced and investigated using renormalization-group theory for three examples: The global phase diagram of $3-$state chiral Potts spin glass with competing left-right chiral interactions is obtained for chirality concentration, chirality breaking concentration and temperature, showing a new spin-glass phase. An unusual fibrous patchwork of microreentrances of all four (ferromagnetic, left chiral, right chiral, chiral spin glass) ordered phases is seen. The spin-glass phase boundary to disordered phase shows, unusually, more chaotic behavior than the chiral spin-glass phase itself. The $q-$state chiral clock double spin-glass model has competing left-right chiral and ferromagnetic-antiferromagnetic interactions. The global phase diagram is obtained for antiferromagnetic bond concentration, chirality-breaking concentration, random chirality strength, and temperature. The global phase diagram for $q = 5$ includes a ferromagnetic, a multitude of chiral phases with different pitches, a chiral spin glass, an algebraically ordered critical phases. The ferromagnetic and chiral phases intercede with each other to form a widely varying continuum of Devil's staircase structures. The global phase diagram for $q = 4$ shows, four different spin-glass phases, including conventional, chiral, and quadrupolar spin-glass phases, and phase transitions between spin-glass phases. Chaotic behaviors are measured through Lyapunov exponents.

ÖZET

HELEZONİ SPIN CAMLARI, SÜREKLİ ŞEYTAN MERDİVENLERİ VE DONMUŞ DÜZENSİZLİKLERDEN EŞİKLENMİŞ KABALAŞMA

TOLGA ÇAĞLAR

Doktora Tezi, Haziran 2017

Tez Danışmanı: Prof. A. Nihat Berker

Anahtar Kelimeler: Donmuş düzensiz sistemler, helezoni spin camı, renormalizasyon grubu kuramı, arayüz kabalaşma, şeytan merdivenleri

Tek eksenli anizotropik üç boyutlu Ising modelinin kabalaşma faz diyagramı, sert spin ortalama alan yöntemiyle çıkarılmıştır. Rastgele donuk iğnelenmiş merkezler ve eksiltilmiş bağlar ile izotropik ve anizotropik Ising modelinin arayüzünün, ardışık eşikli anizotropi etkileşmelerinde kabalaştığı görülmüştür. Ortaya koyduğumuz donmuş karmaşık helezoni, renormalizasyon grubu kuramıyla üç örnekte incelenmiştir: $3-$durumlu helezoni Potts spin camındaki karşıt sol-sağ helezoni etkileşmeler ile bütünsel faz diyagramı çıkarılmış ve yeni spin camı elde edilmiştir. Bütünsel faz diyagramı, sıcaklık, helezoni yoğunluğu, ve helezoni bozma yoğunluğu değişkenlerine bağlı olarak çıkarılmıştır. Daha önce görülmemiş lifli mikroreentrans bölgeleri ferromanyetik, sol helezonik, sağ helezonik ve helezonik spin camı fazlarını iç içe barındırdığı gösterilmiştir. Helezonik spin camının düzensiz faz ile yaptığı hududun, beklentinin aksi yönde, helezonik spin camından daha kaotik olduğu belirtilmiştir. $q-$durumlu helezoni saat çifte spin camının bütünsel faz diyagramı, donmuş karşıt sol-sağ helezoni ve ferromanyetik-antiferromanyetik etkileşmeler ile hesaplanmıştır. Bu faz diyagramı sıcaklık, helezoni şiddeti, antiferromanyetik etkileşme yoğunluğu ve helezoni bozma yoğunluğu değişkenlerine bağlı olarak çıkarılmıştır. $q = 5$ için çıkarılan bütünsel faz diyagramında ferromanyetik, çok sayıda farklı atımlı helezoni, helezoni spin camı ve her noktada kritik olan cebirsel fazlar bulunmuştur. Ferromanyetik ve helezoni fazlar iç içe girerek sürekli değişen şeytan merdiven yapılarını oluşturmaktadır. $q = 4$ için oluşturulan faz diyagramı, alışılagelmiş, helezoni ve kuadrupolar spin camlarını içermektedir. Kaotik davranışlar, spin camları ve spin camlarının diğer fazlarla hudutlarında Lyapunov üstelleri ile belirlenmiştir.

TABLE OF CONTENTS

LIST OF TABLES

LIST OF FIGURES

Chapter 1

INTRODUCTION

Phase transitions and critical phenomena have been studied since the occurrence of the 'equation of state' of liquid-gas systems. The concept was first put forward by van der Waals, on his doctoral thesis in 1873 [1]. However, the current understanding of phase transitions below the critical temperatures is due to the corrections from Maxwell [2], since the mean-field solutions obtained from van der Walls theory are inconsistent with experimental systems [3]. Later, similar mean-field calculations are introduced in the phase transitions of ferromagnets [4, 5]. Finally, these different systems were combined to generalize the phase transitions through universality of critical points [6, 7].

Critical phenomena studies the thermodynamics of systems around critical points, where infinite-range fluctuations are present. The correlation length due to these fluctuations diverges, hence the systems are scale-free, meaning that identical behavior is seen at every scale. Therefore scaling laws are introduced [8], which studies the thermodynamics of systems around critical points. Although mean-field theories can be accurate in continuous media where long-range forces are present, it fails drastically in many systems with typical, atomic-range interactions.

The study of phase transitions and critical phenomena undoubtedly shows its importance in our daily life. The criticality from collective behaviors of many particles have been described extensively in homogeneous systems [6, 9]. However, these homogeneous systems are applicable to a small number of real-world problems. We know that many of the real-world problems include impurities, hence quenched random systems are introduced for correct identification and classification of these systems.

Chapter 2

PHASE TRANSITIONS AND RENORMALIZATION-GROUP THEORY

The aim of this preliminary chapter is to give a brief introduction to the subject and to introduce the fundamentals of the methods used in following chapters. We begin by a brief description of the critical phenomena, including some analogies of fluid systems with the magnetic systems. We continue the description of thermodynamics, from the partition function, and the Ising model, which is generally considered as the basis for models, as is done in this thesis. Lastly, we will mention the well-defined methods of statistical mechanics, in the study of quenched random systems.

2.1. Critical Phenomena

2.1.1. Phases of Matter

The collective behaviors of many particles are usually unclear from a single-particle perspective. Graphite is a fragile and slippery material, hence it provides the core of a pencil, whereas diamond is one of the strongest materials, used in precision cutting of glass. These are different phases obtained from different arrangement of the same carbon atoms, resulting from varying thermodynamic parameters, such as pressure and temperature, also mentioned in Ref. [10].

Let us examine the phase diagram of H_2O, shown on the left of Fig. 2.1. Although each molecule bears identical properties, the behavior of liquid and vapor is very different. This difference occurs due to a change in their collective behaviors, at different temperatures T and pressures P. The lines in Fig. 2.1 represent the phase boundaries, where two phases coexist at the same time, and the point T is the triple point, where all three phases coexist. A transition between different phases, through the lines of coexisting phases, is called a first-order phase transition. The point where the first-order phase transition line
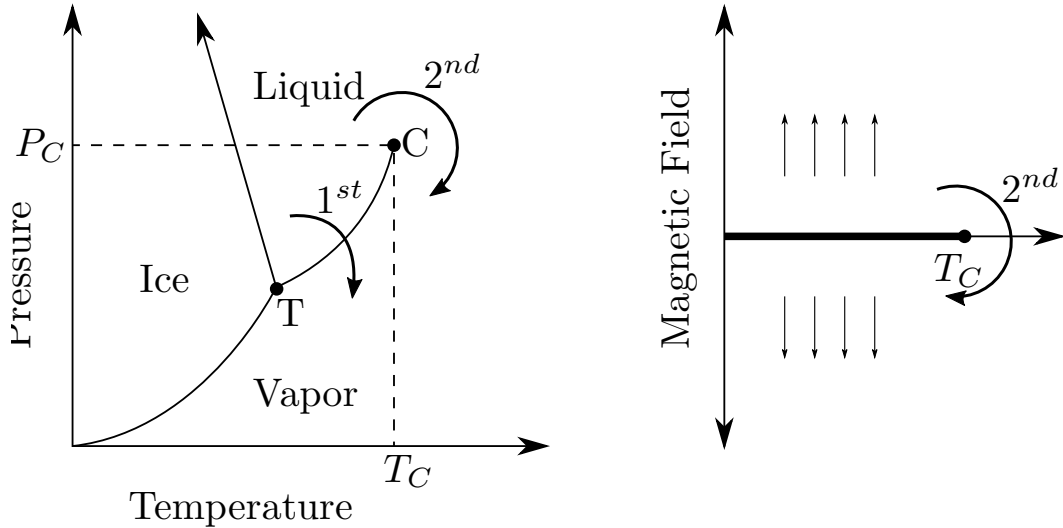
Figure 2.1: On the left, the phase diagram of H_2O molecules is given. Liquid and vapor are differentiated from their densities, and separated by a first-order phase transition line, where both phases coexist. The first- and second-order phase transitions are indicated. The critical point, where the first-order phase transition terminates is shown with C. The temperature and the pressure at which this criticality occurs is respectively the critical temperature T_C and the critical pressure P_C. On the right, the phase diagram of a magnetic system under external magnetic field. The two phases, 'up' and 'down', are differentiated from their magnetizations, and are separated by a first-order phase transition line, where the two phases coexist, and form domains. The point where this line is terminated is the critical point, occurs at temperature T_C.

terminates is called the critical point, shown with C in Fig. 2.1. The temperature and pressure at which this critical point occurs is, respectively, the critical temperature T_C, and the critical pressure P_C. A phase transition at the terminus of the line of coexisting phases is called the second-order phase transition.

Analogous to the fluid systems, the phase diagram of a magnetic system is given on the right of Fig. 2.1, also indicating the phase boundary between 'up' and 'down' spins (lines of coexisting phases), where a first-order phase transition occurs. A second-order phase transition occurs at the terminus of the first-order phase boundary, where the magnetization changes continuously but singularly, and is also shown, indicating the critical temperature T_C. Before we further examine this critical point, we should first mention the fundamental function that forms the building blocks of statistical mechanics.

Partition function

The discussion of the partition function should begin by examining the degrees of freedom of the systems that statistical mechanics treats. In classical systems with small number of degrees of freedom, the action is straightforward and derived from equations of motion, in position and momentum parameters, making six degrees of freedom for

each particle. In order to find the motion of N particles, we therefore need to solve a system of differential equations with $6N$ variables. The usual size of a system in statistical mechanics is 10^{23} particles. In this scale, the equations are not yet solvable in today's technology, therefore we seek the methods derived from partition theory.

For simplicity, we consider N interacting particles, freely moving confined to a volume of a container, as shown in Fig. 2.2(a). The internal energy of the system is given as

$$\mathcal{H} = \sum_i \frac{\boldsymbol{p}_i^2}{2m} + \sum_{ij} V(\boldsymbol{x}_i - \boldsymbol{x_j}), \tag{2.1}$$

where the second summation runs over each interacting pairs, $\boldsymbol{p}_i$ is the momentum of each particle i, and $V(\boldsymbol{x}_i - \boldsymbol{x_j})$ is the interaction between the particles i and j. At fixed temperature T, the energy of the system, due to interactions between neighboring particles, is not fixed, and randomly distributed with corresponding Boltzmann factors $e^{-\mathcal{H}/k_B T}$, where k_B is called Boltzmann constant, implying a probability for the system to have energy $\mathcal{H}$. The average energy is therefore calculated as

$$\langle \mathcal{H} \rangle = \frac{1}{\mathcal{Z}} \int \prod_i d\boldsymbol{p}_i d\boldsymbol{x}_i \mathcal{H} e^{-\mathcal{H}/k_B T}, \tag{2.2}$$

where the integral is over all possible values of the momentum and space variables, and $\mathcal{Z}$ is the normalization constant

$$\mathcal{Z} = \int \prod_i d\boldsymbol{p}_i d\boldsymbol{x}_i e^{-\mathcal{H}/k_B T}, \tag{2.3}$$

which is called the partition function of the system. Note that in the partition function $\mathcal{Z}$, the possible arrangements of the system is embedded into a single summation, in terms of their energies. In thermodynamics, the measurable quantities are averages using these distributions. The average internal energy for non-interacting particles therefore can be calculated from Eq. (2.2) with $V = 0$. In this way, the temperature of the system is related to the average internal energy as

$$\langle \mathcal{H} \rangle = \frac{3}{2} N k_B T, \tag{2.4}$$

which is obtained for ideal gases in three dimensions. In fact, the fraction $\frac{3}{2}N$ comes from $3N$ degrees of freedom, with each having square dependence to the energy of the system Eq. (2.1). If, for example, the interactions also contain square dependence, as in the case of harmonic oscillators, $\frac{1}{2}k_B T$ energy would be included in the average internal energy for each square-dependent term. However, usually systems do not possess this

type of simplicity, and in a typical problem, simplifications have to be made for further examination.

The Ising model

The complex systems mentioned above can be simplified by mapping of thermodynamic properties. For example, increased pressure inside the container in Fig. 2.2(a) increases the density of the fluid, whereas increased external magnetic field for a ferromagnetic crystal shown in Fig. 2.2(b) aligns the atoms in the direction of the field and thereby increases the magnetization of the system. Hence the pressure in fluid systems

(a)   (b)
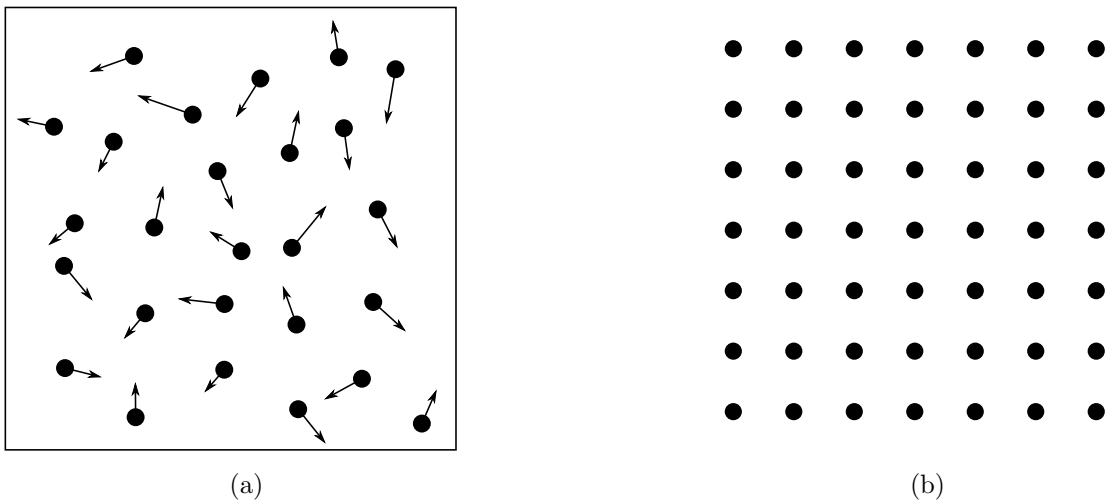
Figure 2.2: (a) A two-dimensional container has particles moving in random directions, with random velocities, chosen from the Boltzmann distribution. (b) A square lattice has fixed sites, but has properties called spins with random values assigned from the Boltzmann distribution. In both cases, the thermodynamics of the system is examined through calculation of averages, using the partition function mentioned in Section 2.1.1.

is analogous to the external magnetic field in magnetic systems. Another analogy can be found in the critical behavior of He^3-He^4 mixtures with the Blume-Emery-Griffiths model [11], in terms of their corresponding chemical potentials.

In order to examine the behaviors of the structures mentioned earlier, we consider a simpler case of a two-dimensional square lattice with N lattice points (sites) as shown in Fig. 2.2(b). In the Ising model, we further simplify by fixing the position of each site, and giving each a binary variable, called spins, with $s_i = +1$ or -1 possible values only, such that there are 2^N possible arrangements. In statistical mechanics, we can physically examine this system by assigning an energy, called the Hamiltonian, to each possible

arrangement,

$$-\beta\mathcal{H} = \sum_{\langle ij \rangle} J s_i s_j + \sum_i H s_i, \qquad (2.5)$$

where $\beta = 1/k_B T$, the summation on the left is over the interacting nearest-neighboring sites with bond strength J, and H is the external magnetic field, and in most of the cases below, taken zero. The bond strength, therefore, is the only parameter of the system, and inversely proportional to the temperature. From now on, we consider J^{-1}, the dimensionless parameter, as the temperature of the system.

The Hamiltonian forms the statistical basis for the methods that are used and further improved in this thesis. At low temperatures, the system tries to maximize this Hamiltonian, in order to fulfill the requirements of thermodynamics, by choosing best possible values for the spins s_i, and maximize the probability $e^{-\beta\mathcal{H}}$. For example, in zero-field ferromagnetic systems, where the interactions are ferromagnetic, $J > 0$, the aligned spins are favored with all $s_i = +1$, or all with $s_i = -1$.

The possible arrangements of the system is embedded into a single summation, in terms of their energies, which is the partition function, also mentioned in Section 2.1.1. The Boltzmann factors obtained from each energy are summed up over all possible arrangements of spins as

$$\mathcal{Z} = \sum_{\{s\}} e^{-\beta\mathcal{H}\{s\}}, \qquad (2.6)$$

where the summation runs over each possible arrangement of sites, forming the set of $\{s\}$, and $\beta\mathcal{H}\{s\}$ is the Hamiltonian of the system calculated from (2.5) at corresponding arrangement of the spin values. Note that the summation is analogous to the integral in Eq. (2.3), which also runs over all possible position-momentum space of the system.

The Ising model is a special case of a more general one, clock models. In the q-state clock model, the sites have spin values of unit vectors that are confined to a plane and that can only point along q angularly equidistant directions, with Hamiltonian

$$-\beta\mathcal{H} = \sum_{\langle ij \rangle} J \vec{s_i} \cdot \vec{s_j} = \sum_{\langle ij \rangle} J \cos\theta_{ij}, \qquad (2.7)$$

where $\beta = 1/k_B T$, $\theta_{ij} = \theta_i - \theta_j$, at each site i the spin angle θ_i takes on the values $(2\pi/q)\sigma_i$ with $\sigma_i = 0, 1, 2, \ldots, (q-1)$, and $\langle ij \rangle$ denotes that the sum runs over all nearest-neighbor pairs of sites.

The Ising model can also be further generalized by the q-state Potts model with the
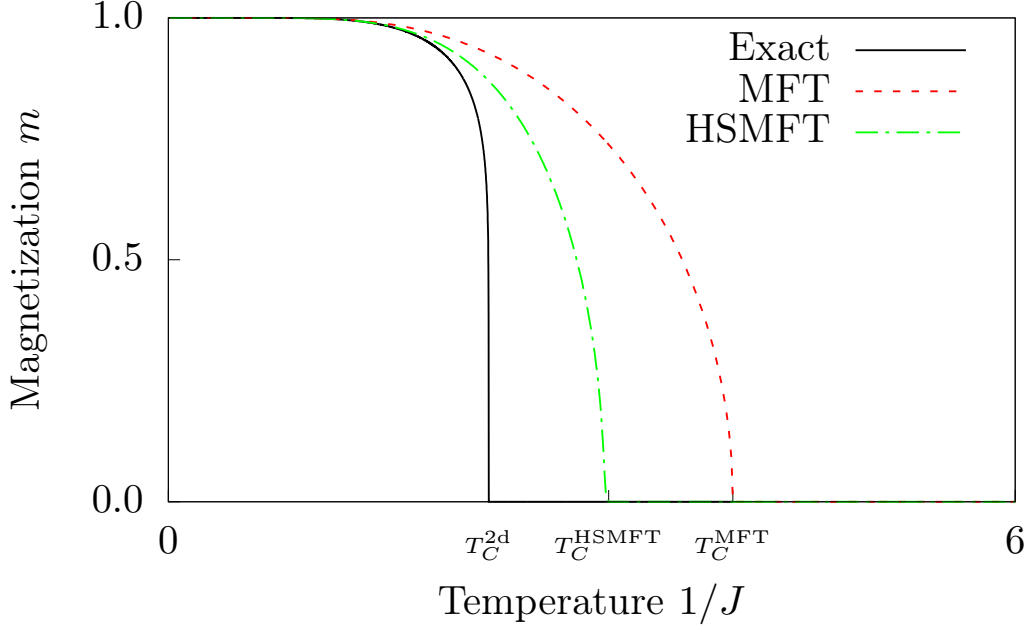
Figure 2.3: The calculated magnetizations of $d = 2$ Ising Model, obtained from the exact solution (solid) [14], from the mean-field approximation (dashed) using Eq. (2.20), and from the hard-spin mean-field approximation (dash-dotted), using Eq. (2.21), indicating the critical temperatures of for each case, T_C^{2d} for exact, T_C^{MFT} for mean-field approximation, T_C^{HSMFT} for hard-spin mean-field approximation.

Hamiltonian

$$-\beta\mathcal{H} = \sum_{\langle ij \rangle} J_{ij}\delta(s_i, s_j), \tag{2.8}$$

where $\delta(s_i, s_j) = 1(0)$ for $s_i = s_j(s_i \neq s_j)$. The spin values of the Potts model can be defined by unit vectors, which point to q symmetric directions in a hypertetrahedron in $q - 1$ dimensions. The Ising model can be mapped to the $q = 2$ Potts and $q = 2$ clock models, and $q = 3$ and 4 Potts models can be mapped to $q = 3$ and 4 clock models respectively [12, 13].

2.1.2. The Critical Point and Universality

Phases are differentiated by the order parameter. In the diamond example, the order parameter is the arrangement of the carbon atoms, and differentiates diamond from graphite. Liquid and gas phases are differentiated by their densities. In ferromagnetic systems mentioned previously, the order parameter is the magnetization per site m calculated as the average of the spins per site. This average is calculated using the partition function, as well as any other measurable quantity, as

$$m = \langle s_i \rangle = \frac{1}{\mathcal{Z}} \sum_{\{s\}} \left(\frac{1}{N} \sum_i s_i \right) e^{-\beta\mathcal{H}\{s\}}. \tag{2.9}$$

7

The disordered phase has uncorrelated sites to the rest of the system, hence the sites can have randomly $+1$ or -1 spin values, setting $m = 0$. In an ordered (ferromagnetic) phase, when no external magnetic field is present, the system is on the phase boundary, described in Section 2.1.1, where two differently ordered phase coexist, leading to domain formations of $+1$ or -1 valued spins. As the temperature is increased, these domains are lost, leaving a disordered (paramagnetic) phase, hence the system undergoes a phase transition. The temperature at which this transition occurs is the critical temperature $J_c^{-1} = T_c$, where at the critical point, the typical size of the fluctuations, called the correlation length ξ, diverges. The exactly calculated magnetization of the $d = 2$ Ising model is shown in Fig. 2.3, also indicating the exact critical temperature T_C^{2d}. The other two temperatures T_C^{HSMFT} and T_C^{MFT} show the calculated critical temperatures from mean-field theories, mentioned in Section 2.2.4.

The study of critical phenomena is based on the diverging behavior of thermodynamic properties around the critical point. As the critical point is reached, also shown in Fig. 2.3, the magnetization approaches to zero. The thermodynamics of the Ising model (see Eq. (2.5)) is observed through the partition function mentioned in Eq. (2.6), which is a function of temperature T and external magnetic field H as $\mathcal{Z} = \mathcal{Z}(T, H)$. Therefore, the total magnetization of the system, obtained from partition function as

$$M = \frac{\partial log\mathcal{Z}}{\partial H}, \tag{2.10}$$

is also a function of temperature T and external magnetic field H as $M = M(T, H)$. Therefore, the critical point can be studied through the magnetization in two independent directions: (1) In zero-field, $H = 0$, the magnetization approaches to zero, with the temperature approaching to critical temperature $T \to T_C$ as

$$M \sim \left| \frac{T - T_C}{T_C} \right|^{\beta}, \tag{2.11}$$

where β is one of the many critical exponents, also mentioned in Table 2.1. (2) At the critical temperature, $T = T_C$, the magnetic field is tuned down, $H \to 0$, hence the magnetization approaches to zero as

$$M \sim H^{1/\delta}, \tag{2.12}$$

where δ is another critical exponent. The formation of the large fluctuations implies a diverging correlation length, $\xi \to \infty$. The behavior of this correlation length can be measured from the spin-spin correlation function of the system. Table 2.1 gives a list of common critical exponents used in the thermodynamics of magnetic materials, and mea-

Exponent	Direction of Approach	Behavior	Description
β	$H = 0, T \to T_C$	$M \sim \left\| \dfrac{T - T_C}{T_C} \right\|^{\beta}$	magnetization
δ	$H \to 0, T = T_C$	$M \sim H^{1/\delta}$	
α	$H = 0, T \to T_C$	$C_H \sim \left\| \dfrac{T - T_C}{T_C} \right\|^{-\alpha}$	specific heat
γ	$H = 0, T \to T_C$	$\chi_T \sim \left\| \dfrac{T - T_C}{T_C} \right\|^{-\gamma}$	susceptibility
ν	$H = 0, T \to T_C$	$\xi \sim \left\| \dfrac{T - T_C}{T_C} \right\|^{-\nu}$	correlation length
η	$H = 0, T \to T_C$	$\Gamma(r) \sim \|r\|^{d-2+\eta}$	correlation function (d is dimensionality)

Table 2.1: The behavior of thermodynamic functions as the critical point is reached, and their corresponding critical exponents.

sured from different experimental systems. Although the critical temperature T_C varies in different systems, the critical exponents might collude, forming a universality class. One widely used example in phase transitions is the measured β for eight different fluid systems from Ref. [7].

2.2. Quenched Random Systems

2.2.1. Interface Roughening

The ordering phase transition, in a crystal causes the formation of macroscopic domains, differently ordered with respect to each other. The interface between such domains incorporates static and dynamic phenomena of fundamental and applied importance. Of singular importance is the occurrence of yet another phase transition, distinct from the ordering phase transition, which is the interface roughening phase transition [15, 16]. The temperature at which the interface roughening phase transition occurs is called the roughening temperature T_R. Below the roughening temperatures $T < T_R$, the domains are separated by a localized smooth interface width, while for temperatures above the roughening temperature, the interface is rough and moves arbitrarily away from its localized position [15]. The roughening transition in $d = 3$ uniaxially anisotropic Ising models is studied for at finite temperatures in Chpt. 3, and at low temperatures in the presence of frozen impurities Chpt. 4.

2.2.2. Spin-Glass Systems

The glass phase obtained from SiO_2, has randomly located silica molecules, whereas in the crystal form, the silica molecules are well defined with the corresponding unit cells. The interactions between neighboring molecules is therefore randomly chosen for the glass phase. In the statistical models used and briefly explained in Section 2.2.3, the position of the sites have no effect on the physics of the system. However, the identical effect can be obtained from competing ferromagnetic-antiferromagnetic interactions [17]. The random locations of the silica molecules are analogous to the spin-glass systems, in the sense that the interactions are randomly distributed, and frozen (quenched). The Ising spin-glass is defined with the Hamiltonian

$$-\beta\mathcal{H} = \sum_{\langle ij \rangle} J_{ij} s_i s_j,$$ (2.13)

where the bond strengths J_{ij}, with quenched (frozen) ferromagnetic-antiferromagnetic randomness, are $+J > 0$ (ferromagnetic) with probability $1 - p$ and $-J$ (antiferromagnetic) with probability p, with $0 \leq p \leq 1$. The obtained phase diagram of the Ising spin-glass system is shown qualitatively in Fig. 2.6. Chapters 5–7 show the extension of these spin-glass systems with competing left- and right-chiral interactions.

2.2.3. Statistical Models

In the following paragraphs, we present some of the statistical models, which our studies have used, and extended further to examine the thermodynamics of quenched random systems, using well-defined methods of hard-spin mean-field theory[18, 19] and Migdal-Kadanoff renormalization-group theory [20, 21].

$d = 3$ anisotropic Ising model

The uniaxially anisotropic $d = 3$ Ising model is defined by the Hamiltonian

$$-\beta\mathcal{H} = J_{xy} \sum_{\langle ij \rangle}^{xy} s_i s_j + J_z \sum_{\langle ij \rangle}^{z} s_i s_j,$$ (2.14)

where, at each site i of a $d = 3$ cubic lattice with periodic boundary conditions, $s_i = \pm1$. The first sum is over nearest-neighbor pairs of sites along the x and y spatial directions, and the second sum is over the nearest-neighbor pairs of sites along the z spatial direction. In Chpts. 3 and 4, we study the interface roughening phase transitions, briefly described in Section 2.2.1, by inducing an interface to the system, either via antiperiodic boundary

conditions [Chpt. 3], or oppositely fixed boundary conditions [Chpt. 4] at the two terminal planes in the z spatial direction.

Another well studied model is the anisotropic next-nearest neighbor Ising model (ANNNI), with Hamiltonian

$$-\beta\mathcal{H} = J_1 \sum_{\langle ij \rangle_1} s_i s_j + J_2 \sum_{\langle ij \rangle_2}^{z} s_i s_j, \qquad (2.15)$$

where the first summation is over the nearest neighbor pairs with bond strengths $J_1 > 0$ (ferromagnetic), and the second summation is along the next-nearest neighbor pairs along the z spatial direction only, with bond strengths $J_2 < 0$ (antiferromagnetic). The phase diagram of this model is obtained through mean-field calculations including a disordered, a ferromagnetic and a 'modulated phase' [22]. The modulated phase is characterized by a wavevector, measured in the z spatial direction. The pitch of this wavevector varies with J_2/J_1 and temperature, presenting many phases inside a modulated phase. This pitch varies in two ways: (i) Discrete jumps in the wavevector form a devil's staircase. A system is said to be in a commensurate order when the pitch is an integer multiple of its lattice spacing, and incommensurate order when it is an irrational multiple of its lattice spacing. It is found that there are infinitely many commensurate phases in the one-dimensional Ising model with long range antiferromagnetic interactions [23] and in low temperatures of the $d > 2$ ANNNI model [24]. (ii) In the two-dimensional ANNNI model, a 'sinusoidal' phase is found [25], where the magnetization varies sinusoidally and a continuously varying pitch is seen for threshold temperatures as a function of J_2/J_1. In the obtained phase diagram of the two-dimensional ANNNI model [25], the sinusoidal phase has a boundary to the ferromagnetic phase in lower J_2/J_1, a boundary to the disordered phase in higher temperatures and a boundary to the modulated phase in lower temperatures. The phase boundary between the sinusoidal phase and the modulated phase meets with its boundary to the ferromagnetic phase at the multiphase point [24], where infinitely many number of ordered phases meet. In Chpt. 6, we show the formation of the devil's staircases due to doubly competing ferromagnetic-antiferromagnetic and left-right chiral interactions, and also discuss the continuous variation of the pitches.

q-state chiral Potts model

Here, we mention the chiral Potts model, which was originally introduced [26–30] to model the full phase diagram of krypton monolayers, including the epitaxial and incommensurate ordered phases. In addition to being useful in the analysis of surface layers, the chiral Potts model has become an important model of phase transitions and critical

phenomena.

The chiral Potts model is defined by the Hamiltonian

$$-\beta\mathcal{H} = \sum_{\langle ij \rangle}[J_0\delta(s_i, s_j) + J_\pm\delta(s_i, s_j \pm 1],\qquad(2.16)$$

where $\beta = 1/k_BT$, at site i the spin $s_i = 1, 2, \ldots, q$ can be in q different states with implicit periodic labeling, e.g., $s_i = q + n$ implying $s_i = n$, the delta function $\delta(s_i, s_j) = 1(0)$ for $s_i = s_j(s_j \neq s_j)$, and $\langle ij \rangle$ denotes summation over all nearest-neighbor pairs of sites. The upper and lower subscripts of $J_\pm > 0$ give left-handed and right-handed chirality (corresponding to heavy and superheavy domain walls in the krypton-on-graphite incommensurate ordering [27–30]), whereas $J_\pm = 0$ gives the nonchiral Potts model (relevant to the krypton-on-graphite epitaxial ordering [31]).

q-state clock spin-glass model

The q-state clock spin glass is composed of unit spins that are confined to a plane and that can only point along q angularly equidistant directions, with Hamiltonian

$$-\beta\mathcal{H} = \sum_{\langle ij \rangle}J_{ij}\vec{s_i} \cdot \vec{s_j} = \sum_{\langle ij \rangle}J_{ij}\cos\theta_{ij},\qquad(2.17)$$

where $\beta = 1/k_BT$, $\theta_{ij} = \theta_i - \theta_j$, at each site i the spin angle θ_i takes on the values $(2\pi/q)\sigma_i$ with $\sigma_i = 0, 1, 2, \ldots, (q-1)$, and $\langle ij \rangle$ denotes that the sum runs over all nearest-neighbor pairs of sites. As a ferromagnetic-antiferromagnetic spin-glass system [17], the bond strenghts J_{ij}, with quenched (frozen) ferromagnetic-antiferromagnetic randomness, are $+J > 0$ (ferromagnetic) with probability $1 - p$ and $-J$ (antiferromagnetic) with probability p, with $0 \leq p \leq 1$. Thus the ferromagnetic and antiferromagnetic interactions locally compete in frustration centers. Recent stuides on ferromagnetic-antiferromagnetic clock spin glasses are in Refs. [32–34].

2.2.4. Methods for Obtaining Phase Diagrams

Hard-spin mean-field theory

The $d = 2$ Ising model is one of the rare examples that can be solved exactly. Approximation provides the tools in examining different problems, where exact solutions are not available. The mean-field theory considers the spins of the neighboring sites as the magnetization of the system. Thus the partition function of the system with N sites can

be written in terms of single sites, at locality i as

$$\mathcal{Z}_N = \mathcal{Z}_1^N = \left(\sum_{s_i = \pm 1} e^{-\beta \mathcal{H}_i} \right)^N. \tag{2.18}$$

The single-site Hamiltonian is given as

$$-\beta \mathcal{H}_i = \sum_{j=1}^{q} J_{ij} s_i s_j = \sum_{j=1}^{q} J_{ij} s_i m_j, \tag{2.19}$$

where the summation runs over the q neighbors of locality i, m_j is the magnetization of the system, calculated at locality j. One can calculate the magnetization m_i using the single-site partition function $\mathcal{Z}_1$ from Eqs. (2.18) and (2.19), using Eq. (2.9) as

$$m_i = \tanh \left(\sum_{j=1}^{q} J_{ij} m_j \right). \tag{2.20}$$

The equation in Eq. (2.20) is the self-consistency equation of mean-field theory. Using this equation, the magnetization at each site can be calculated iteratively by assigning an initial set of magnetization values to N sites. A new set of N values can be calculated from the self-consistency equation Eq. (2.20), until each magnetization value converges, and the magnetization difference between the two iterations do not exceed a certain tolerance.

Hard-spin mean-field theory, has been introduced as a self-consistent theory that conserves the hard-spin ($|s| = 1$) condition. Hard-spin mean-field theory has yielded, for example, the lack of order in the undiluted zero-field triangular-lattice antiferromagnetic Ising model and the ordering that occurs either when a uniform magnetic field is applied to the system, giving a quantitatively accurate phase diagram in the temperature versus magnetic field variables [18, 19, 35–38], or when the system is sublattice-wise quench-diluted [39]. Hard-spin mean-field theory has also been successfully applied to complicated systems that exhibit a variety of ordering behaviors, such as three-dimensionally stacked frustrated systems [18, 40], higher-spin systems[41], and hysteretic $d = 3$ spin glasses [42]. Furthermore, hard-spin mean-field theory shows qualitative and quantitative effectiveness for unfrustrated systems as well, such as being dimensionally discriminating by yielding the no-transition of $d = 1$ and improved transition temperatures in $d = 2$ and 3 [35, 42], also shown with T_C^{HSMFT} in Fig. 2.3.

In the hard-spin mean-field theory, the nearest-neighbors of the sites are free variables (hard spins), instead of magnetization. The magnetization at site i is therefore calculated
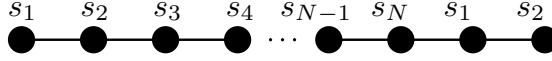
Figure 2.4: The one dimensional chain of N atoms, with periodic boundary conditions.

using the self-consistency equation of the hard-spin mean-field theory as

$$m_i = \sum_{\{s\}} \left[\prod_{\langle ij \rangle} P(m_j, s_j) \right] \tanh \left(\sum_{j=1}^{q} J_{ij} s_j \right), \tag{2.21}$$

where $P(m_j, s_j)$ is the probability at locality j with magnetization m_j. Note that the second summation in Eq. (2.21) is the same summation obtained in Eq. (2.20), where m_j is replaced with s_j, the hard spin. The probability is found from the magnetization calculation Eq. (2.9)

$$m_j = P_+ - P_-, \tag{2.22}$$

where P_+ and P_- are the probabilities of having $+1$ and -1 at locality j, and $P_+ + P_- = 1$. Thus the probability of s_j is calculated as

$$P(m_j, s_j) = \frac{1 + m_j s_j}{2}. \tag{2.23}$$

A similar approach to the mean-field theory calculations can be used to study the quenched random systems using hard-spin mean-field theory.

Migdal-Kadanoff renormalization-group theory

In condensed matter, many of the problems are not exactly solvable, but the simplest cases give insight to more complex ones. The one-dimensional chains with nearest-neighbor interactions J_{ij} only is an example to this situation. The Hamiltonian of this model with N sites is given as

$$-\beta \mathcal{H} = \sum_{i=1}^{N} J_{i,i+1} s_i s_{i+1}, \tag{2.24}$$

where we take periodic boundary conditions as shown in Fig. 2.4. In order to see the strength of renormalization-group theory, one should look at the partition function

$$\mathcal{Z} = \sum_{\{s\}} e^{\sum_{i=1}^{N} J_{i,i+1} s_i s_{i+1}} = \sum_{s_1} \sum_{s_2} \cdots \sum_{s_N} e^{\sum_{i=1}^{N} J_{i,i+1} s_i s_{i+1}}. \tag{2.25}$$

14

The summation on the right-hand side can be grouped for every even-numbered sites. After rearranging the summation, we obtain

$$\mathcal{Z} = \sum_{s_1} \sum_{s_3} \cdots \sum_{s_{2n-1}} \left(\sum_{s_2} \sum_{s_4} \cdots \sum_{s_{2n}} e^{\sum_{i=1}^{N} J_{i,i+1} s_i s_{i+1}} \right). \qquad (2.26)$$

The summations inside the brackets are calculated to find the recursion relations

$$R(s'_{1'}, s'_{2'}) = \sum_{s_2} e^{J_{12} s_1 s_2 + J_{23} s_2 s_3} = e^{J'_{1'2'} s'_{1'} s'_{2'} + \widetilde{G}}, \qquad (2.27)$$

where primes denote the renormalized value of the same lattice, and $\widetilde{G}$ is an additive constant to compensate for the removed sites. In removing the even-numbered sites, we rescale the length of the lattice by a rescaling factor $b = 2$, thereby the number of sites are halved.

This type of grouping is called decimation, also shown for different length rescalings b in Fig. 2.5(a). For $d = 1$ Ising model, the renormalized interactions are calculated as

$$J'_{1'2'} = \frac{1}{2} \ln \left(\frac{e^{J_{12} + J_{23}} + e^{-J_{12} - J_{23}}}{e^{J_{12} - J_{23}} + e^{-J_{12} + J_{23}}} \right). \qquad (2.28)$$

As mentioned in Section 2.1.1, the critical temperature J_C^{-1} can be found from the scale-free behavior of the system at the critical point.

At the critical point, the partition function of the renormalized lattice is scale free, therefore every sublattice has identical partition functions, resulting identical renormalized interactions with the unrenormalized ones, $J'_C = J_C$, also called the fixed point. Hence, the critical temperature, and therefore the critical exponents can exactly be calculated from their corresponding recursion relations.

In a square lattice, a similar approach can be constructed, by decimating every next-nearest neighbors, to obtain a renormalized lattice. Figure 2.5(b) shows one possible decimation with length scale $b = \sqrt{2}$. Although schematically, this seems applicable, the summation through decimated sites bring an extra interaction term between four neighbors of the decimated site, leading to a different partition function. Although the square lattice is exactly solved for Ising model [14, 43] using different methods, these are not applicable to higher dimensions. Thus, we restrict ourselves to renormalization-group theory. We therefore focus on the Migdal-Kadanoff approximate renormalization-group transformations [20, 21] for the cubic lattices, composed of the bond-moving followed by decimation steps, shown in Fig. 6.1(a). This approximation corresponds to exact solutions of hierarchical lattices [44–48]. The corresponding hierarchical lattice of the $d = 3$ cubic lattice, shown in Fig. 6.1(a), can be obtained by the repeated self-imbedding of the left-
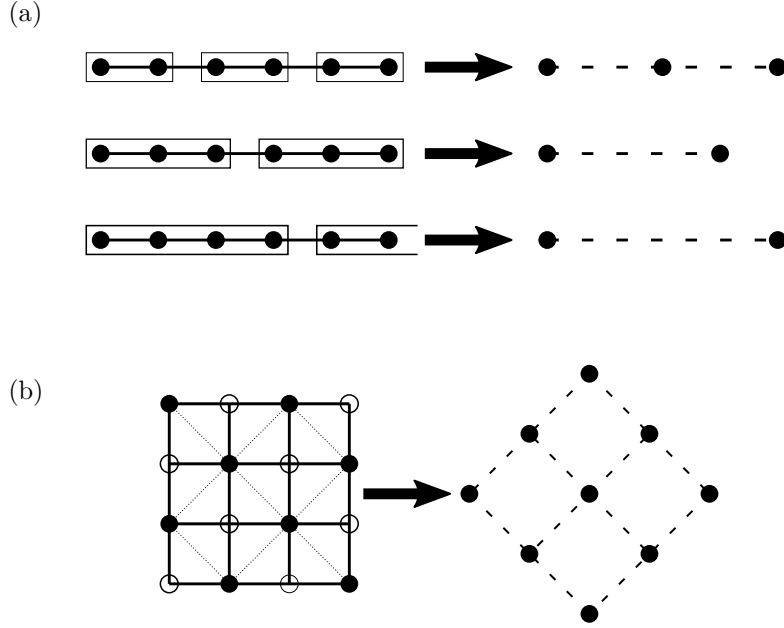
Figure 2.5: (a) shows the decimation process for one-dimensional chains for different length rescalings $b = 2, 3, 4$ from top to bottom. (b) Decimations for a square lattice, with length rescaling $b = \sqrt{2}$. The empty circles are decimated (summed in the partition function). Thin dotted lines on the left figure represent the new bond formations due to this decimation. The lattice on the right is the renormalized lattice after this decimation. Quadruple interactions are formed after this decimation, hence the partition function is not consistent with decimations in two dimensions.

most graph in panel Fig. 6.1(b). The recursion relations obtained from both procedures are identical.

Infinitesimally away from the critical point, the recursion relations move the interaction to a further point, yielding flow diagrams for the recursion relations. Using the recursion relations, we obtain the thermodynamics of the renormalized systems. The renormalization-group theory suggests that under the renormalization transformations, the partition function of the renormalized and unrenormalized systems, which are a function of temperature and external magnetic field at their corresponding renormalized parameters as

$$\mathcal{Z}'(T', H') = \mathcal{Z}(T, H), \tag{2.29}$$

where primes mark the renormalized variable, are equal. For simplicity, we start by considering Kadanoff scaling [8] around the critical point, where the temperature T and magnetic field H are scaled as

$$t' = b^{y_T} t,$$
$$H' = b^{y_H} H, \tag{2.30}$$

where the primes mark the rescaled parameters, $t = |T - T_C|/T_C$. Using the scaling

16
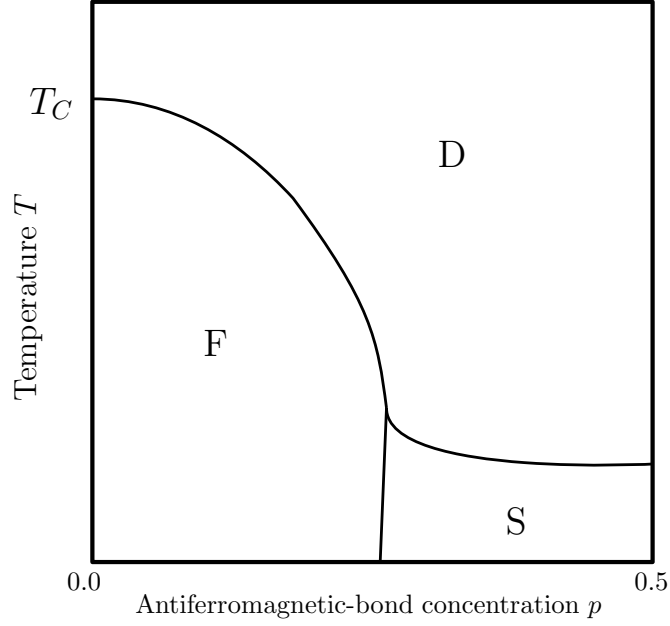
Figure 2.6: The qualitative phase diagram of the Ising spin glass in antiferromagnetic bond concentration p, and temperature T, including ferromagnetic (F), spin-glass (S) and disordered (D) phases. Note that T_C shows the critical temperature obtained from the purely ferromagnetic system. The phase diagram is given only for the antiferromagnetic bond concentrations in the range $0 \leq p \leq 0.5$. The mirror-symmetric part $0.5 \leq p \leq 1$ of the phase diagram would consist of an antiferromagnetic (A) ordering in place of the ferromagnetic phase.

from Eq. (2.30), we can easily obtain the scaling behaviors of the thermodynamics. For example, the scalings for magnetization per site can be calculated as

$$
\begin{aligned}
m(t, H) &= \frac{1}{N} \frac{\partial}{\partial H} \log \mathcal{Z}(t, H) \\
&= \left(b^{-d} \frac{1}{N'} \right) \left(b^{y_H} \frac{\partial}{\partial H'} \right) \log \mathcal{Z}'(t', H') = b^{y_H - d} m'(t', H')
\end{aligned}
\tag{2.31}
$$

which suggests that the magnetization per site rescales as $m' \sim b^{d - y_H} m$. An important result of the discussion in Ref. [8] is that these rescaling functions are analytic and corresponding critical exponents depend on the exponents of y_T and y_H. With the choice of $b = t^{-1/y_T}$, the critical exponent of the magnetization at constant magnetic field is found as

$$
\beta = \frac{d - y_H}{y_T}.
\tag{2.32}
$$

Note that the Kadanoff scaling was introduced before renormalization-group theory. We can assume that the renormalization-group transformations also form analytic functions, hence the flows can be obtained for homogenous systems. Figure 2.7 shows the flow diagram of $d = 3$ Ising ferromagnet with isotropic interactions in a cubic lattice, obtained from Migdal-Kadanoff renormalization-group theory for $d = 3$ and $b = 3$ length rescal-

$$0 \qquad\qquad\qquad\qquad J^* = J_C \qquad\qquad\qquad\qquad \infty$$
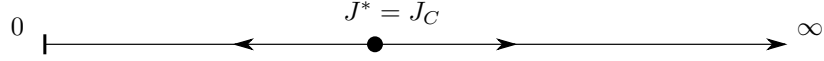
Figure 2.7: The flow diagram of the $d = 3$ Ising model with isotropic and ferromagnetic ($J_{ij} = J > 0$) interactions, indicating the unstable fixed point J^*, where under renormalization transformations, the renormalized interactions move away from this fixed point. Hence, the fixed point is also the critical point $J^* = J_C$.

ings corresponding to the decimations and bond movings in Fig. 6.1. These flows can be used to construct the phase diagram of a given system.

We mention Ising spin-glass systems with randomly distributed ferromagnetic and antiferromagnetic interactions, with Hamiltonian Eq. (2.13). The interactions J_{ij} is chosen randomly from a bimodal distribution of antiferromagnetic interactions ($-J < 0$) with probability p, and ferromagnetic interactions ($+J > 0$) with probability $1 - p$. In renormalization-group transformations, this initial bimodal probability distribution also transforms into another distribution, calculated from the convolution [49]

$$P'(J'_{i'j'}) = \int \left\{ \prod_{ij}^{i'j'} dJ_{ij} P(J_{ij}) \right\} \delta(J'_{i'j'} - R(\{J_{ij}\})), \qquad (2.33)$$

where $P'(J'_{i'j'})$ is the renormalized probability distribution of the renormalized interactions $J'_{i'j'}$, and $R(\{J_{ij}\})$ represents the recursion relations obtained from the corresponding Migdal-Kadanoff renormalization-group transformation from Fig. 6.1. The different thermodynamic phases of the model are identified by the different asymptotic renormalization-group flows of the quenched probability distribution. For all renormalization-group flows, originating inside the phases and on the phase boundaries, Eq. (2.33) is iterated until asymptotic behavior is reached. The obtained phase diagram is given qualitatively in Fig. 2.6 for the $d = 3$ Ising spin-glass model, where the ferromagnetic, disordered and spin-glass phases are shown.

Chaos from renormalization-group trajectories

The trajectories obtained from homogeneous systems are straight forward and can analytically be obtained from the corresponding recursion relations. However, in spin-glass phases, at a specific location in the lattice, the consecutive interactions, encountered under consecutive renormalization-group transformations, behave chaotically [50–52]. This chaotic behavior was found [50–52] and subsequently well established [32, 53–79] in spin-glass systems with competing ferromagnetic and antiferromagnetic interactions.

It has been shown that chaos in the interaction as a function of the rescaling implies chaos in the spin-spin correlation function as a function of distance [71]. Chaos in the spin-glass phase and at its phase boundary are identified and distinguished by different

Lyapunov exponents [32, 53, 71], calculated as [80, 81],

$$\lambda = \lim_{n \to \infty} \frac{1}{n} \sum_{k=0}^{n-1} \ln \left| \frac{dx_{k+1}}{dx_k} \right|,$$

(2.34)

where $x_k = J(ij)/\langle J \rangle$ at step k of the renormalization-group trajectory. In the following chapters, we discuss different spin glasses and differentiated chaoses from Lyapunov exponents using the previously mentioned concepts.

Chapter 3

INTERFACE-ROUGHENING PHASE DIAGRAM OF THE THREE-DIMENSIONAL ISING MODEL FOR ALL INTERACTION ANISOTROPIES FROM HARD-SPIN MEAN-FIELD THEORY

3.1. Introduction

The roughening phase transition, mentioned in Section 2.2.1, is well studied with the three-dimensional Ising model, in the so-called solid-on-solid limit, in which the interactions along one spatial direction (z) are taken to the infinite strength, while the interactions along the x and y spatial directions remain finite. In this case, due to the infinite interactions, the ordering phase transition moves to infinite temperature and is not observed. A study of the system with finite interactions, where both ordering and roughening phase transitions should distinctly be observed, had not been done.

In our current study, hard-spin mean-field theory [Section 2.2.4] is used to study ordering and roughening phase transitions in the three-dimensional ($d = 3$) Ising model for the entire range of interaction anisotropies, continuously from the solid-on-solid limit to the isotropic system to the weakly coupled-planes limit. The phase diagram is obtained in the temperature and interaction anisotropy variables, with separate curves of ordering and roughening phase boundaries. The method, when applied to the anisotropic $d = 2$ Ising model, correctly yields the lack of roughening phase transition.
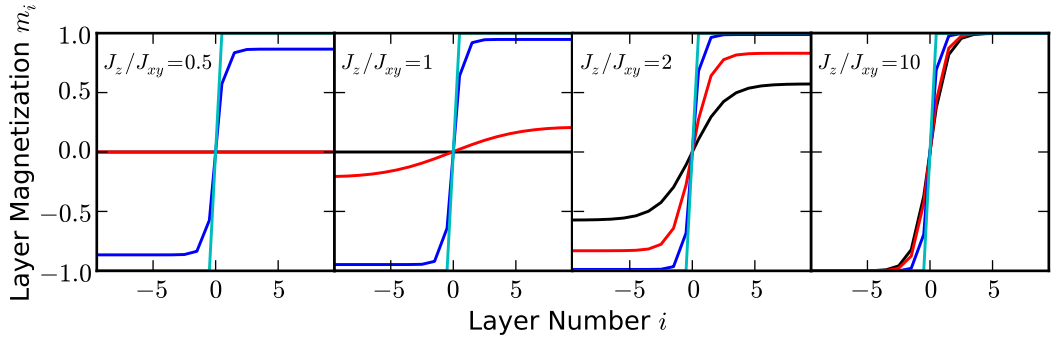
Figure 3.1: For the $d = 3$ anisotropic Ising model, magnetizations m_i versus xy layer-number i curves for different temperatures $1/J_{xy}$. Each panel shows results for the indicated anisotropy J_z/J_{xy}. The curves in each panel, with decreasing sharpness, are for temperatures $1/J_{xy} = 1, 3, 5, 6$. In the left two panels, the high-temperature curves coincide with the horizontal line $m_i = 0$.

3.2.   Hard-Spin Mean-Field Theory

We have applied hard-spin mean-field theory to the global study of the roughening transition in the anisotropic $d = 3$ Ising model. [We have also found that no roughening phase transition is seen in $d = 2$ (Section 3.4).] The uniaxially anisotropic $d = 3$ Ising model is defined by the Hamiltonian (2.14). The interactions are ferromagnetic, J_{xy}, $J_z >$ 0, except for the interaction between two of the xy planes, which has the same magnitude as the other J_z interactions but is antiferromagnetic: $J_z^A = -J_z < 0$. This choice is made in order to induce an interface when the system is ordered. (An alternate approach would have been to use a system without periodic boundary conditions along the z direction, but with oppositely pinned spins at each edge. However, this would have introduced a surface effect at the pinned edges, modifying the magnetization deviations which would thereby not exclusively reflect the spreading of the interface.) For this system, the self-consistent equation of hard-spin mean-field theory is given in Eq. (2.21). The coupled Eqs. (2.21) are solved numerically for the $20 \times 20 \times 20$ cubic system with periodic boundary conditions, by iteration: A set of magnetizations is substituted into the right-hand side of Eq. (2.21), to obtain a new set of magnetizations from the left hand-side. This new set is then substituted into the right-hand side, and this procedure is carried out repetedly, converging to stable values of the magnetizations that are the solution of the equations. The resulting magnetization values depend on the z coordinate only.
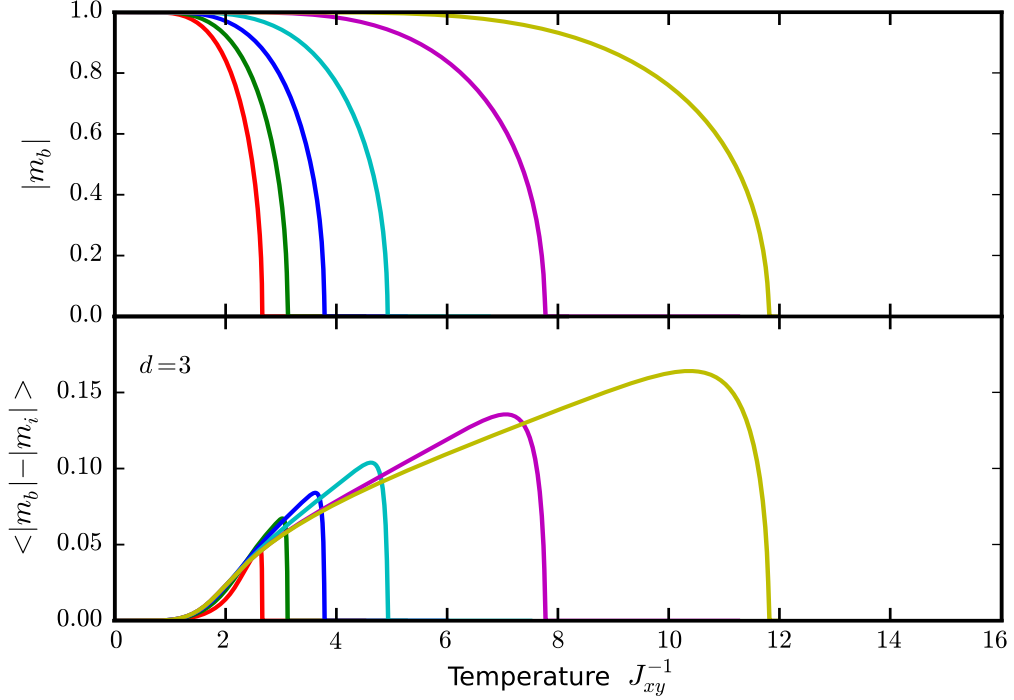
Figure 3.2: Local magnetization data for the $d = 3$ anisotropic Ising model. The curves, starting from the high-temperature side, are for anisotropies $J_z/J_{xy} = 10, 5, 2, 1, 0.5, 0.2$. Upper panel: Magnetization absolute values $|m_b|$ away from the interface as a function of temperature $1/J_{xy}$, for different values of the anisotropy J_z/J_{xy}. Lower panel: The deviation $|m_b| - |m_i|$ averaged over the system versus temperature $1/J_{xy}$ for different anisotropies J_z/J_{xy}. This averaged deviation vanishes when the interface is smooth. Note the qualitatively different low-temperature behavior in $d = 2$ case shown in Fig. 3.4

3.3. Results: Ordering and Roughening Phase Transitions in $d = 3$

A series of curves for the magnetizations of m_i versus xy layer number i are shown for different temperatures $1/J_{xy}$, for a given anisotropy J_z/J_{xy} in each panel of Fig. 3.1. For each value of the anisotropy, the magnetizations m_i are zero at high temperatures and become nonzero below the ordering transition temperature T_C. The ordering onset is seen in the upper panel of Fig. 3.2, where the magnetization absoluve values $|m_b|$ away from the interface are plotted as a function of temperature $1/J_{xy}$, for different values of the anisotropy J_z/J_{xy}.

In Fig. 3.1, it is also seen that, at temperatures just below T_C, the interface between $m_i \gtrless 0$ domains is spread over several layers. It is also seen that below a lower roughening-transition temperature T_R, the interface becomes localized between two consecutive layers, reversing the sign of the magnetization m_i with no change in magnitude. This onset is best seen in the lower panel of Fig. 3.2, where the deviation $|m_b| - |m_i|$ averaged over the system is plotted as a function of temperature $1/J_{xy}$ for different

anisotropies J_z/J_{xy}.

Thus, we have deduced the phase diagram, for all values of the anisotropy J_z/J_{xy} and temperature $1/J_{xy}$, as shown in Fig. 3.3. The roughening transition is obtained by fitting the averaged deviation curves (lower panel of Fig. 3.2) within the range $\langle |m_b| - |m_i| \rangle = 0.01$ to 0.04, to find the temperature at which the averaged deviation reaches zero, meaning that the interface becomes localized between two consecutive layers, reversing the sign of the magnetization m_b with no change in magnitude. In Fig. 3.3 the ordering and roughening phase transitions occur as two separate curves, starting in the decoupled planes ($J_z/J_{xy} = 0$) limit and scanning at finite temperature the entire range of anisotropies. The ordering transition starts, for the decoupled planes limit $J_z/J_{xy} = 0$, at $1/J_{xy} = 3.12$, to be compared with the exact result of $1/J_{xy} = 2.27$. The ordering transition continues to $1/J_{xy} = 5.06$, to be compared with the precise [82] result of $1/J_{xy} = 4.51$, for the isotropic case $J_z/J_{xy} = 1$. In the solid-on-solid limit ($J_z/J_{xy} \to \infty$), the ordering boundary goes to infinite temperature. The roughening transition starts at $1/J_{xy} = 0$ for J_z/J_{xy} close to zero and settles to a finite temperature value before the isotropic case. Thus, the roughening transition temperature $1/J_{xy}$ is 1.45 in the isotropic case $J_z/J_{xy} = 1$ and 1.62 in the solid-on-solid limit $J_z/J_{xy} \to \infty$, the latter to
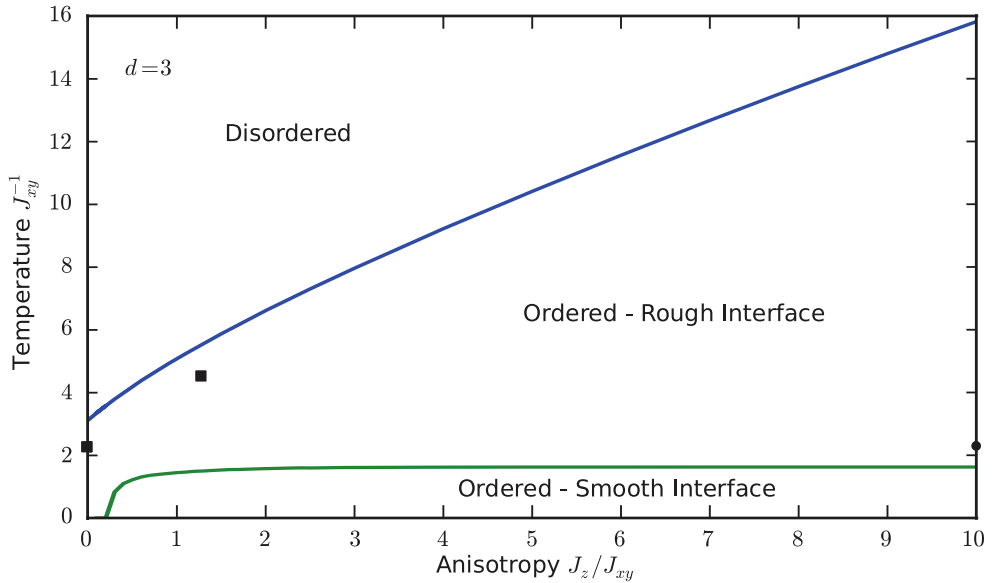
Figure 3.3: For the $d = 3$ anisotropic Ising model, the calcualted phase diagram showing the disordered, ordered with rough interface, and ordered with smooth interface phases. The squares indicate the exact ordering temperatures from duality at $J_z/J_{xy} = 0$ and from Ref. [82] at $J_z/J_{xy} = 1$. The circle indicates the roughening transition temperature for the solid-on-solid limit $J_z/J_{xy} \to \infty$ [16]. The roughening transition is obtained by fitting the averaged deviation curves (lower panel of Fig. 3.2) within the range $\langle |m_b| - |m_i| \rangle = 0.01$ to 0.04, to find the temperature at which the averaged deviation reaches zero, meaning that the interface becomes localized between two consecutive layers, reversing the sign of the magnetization $|m_b|$ with no change in magnitude.
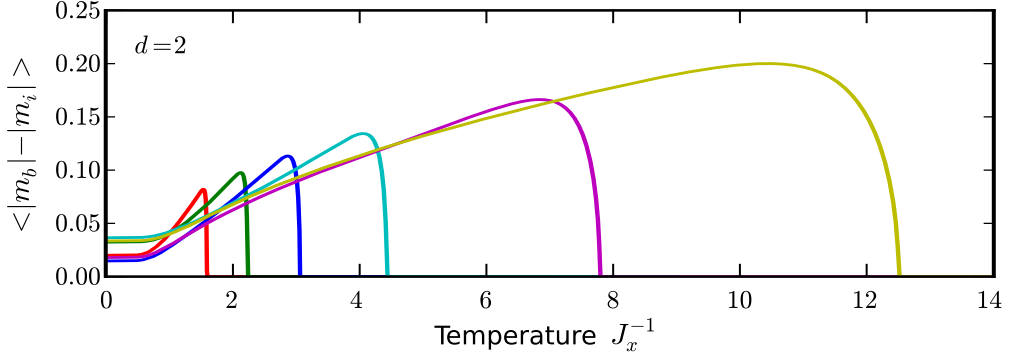
Figure 3.4: For the $d = 2$ anisotropic Ising model, the deviation $|m_b| - |m_i|$ averaged over the system versus temperature $1/J_{xy}$ for different anisotropies $J_z/J_{xy} = 10, 5, 2, 1, 0.5, 0.2$. It is seen that the deviation does not vanish, i.e., the interface does not localize, down to zero temperature. Thus, a qualitatively different low-temperature behavior occurs, as compared with the $d = 3$ case shown in the lower panel of Fig. 3.2.

be compared with the value of 2.30 ± 0.10 from Ref. [16].

3.4. Results: Ordering Transitions but No Roughening Transitions in $d = 2$

We have also applied our method to the anisotropic $d = 2$ Ising model, defined by the Hamiltonian

$$-\beta\mathcal{H} = J_x \sum_{\langle ij \rangle}^{x} s_i s_j + J_z \sum_{\langle ij \rangle}^{z} s_i s_j, \tag{3.1}$$

where, on a 20×20 square lattice with periodic boundary conditions, the first sum is over nearest-neighbor pairs of sites along the x spatial direction, and the second sum is over the nearest-neighbor pairs of sites along the only other (z) spatial direction.

The ordering phase transition is observed in $d = 2$ similarly to the $d = 3$ case.
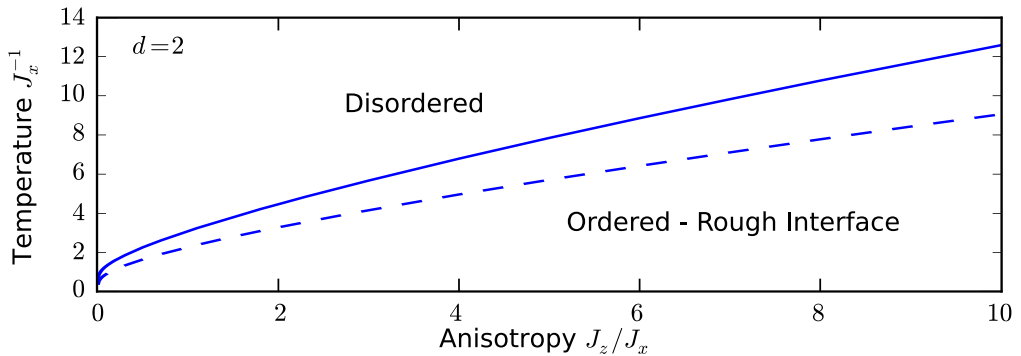
Figure 3.5: For the $d = 2$ anisotropic Ising model, the phase diagram showing the disordered phase and the ordered phase with rough interface. The dashed curve is the exact ordering boundary $\sinh(2J_x)\sinh(2J_z) = 1$ obtained from duality. No ordered phase with smooth interface is found.

However, the rough interface phase continues to zero temperature, as seen in the $|m_b| - |m_i|$ curves in Fig. 3.4. Thus, no roughening phase transition occurs in $d = 2$. The corresponding phase diagram is given in Fig. 3.5. The ordering transition starts, for the decoupled lines limit $J_z/J_x = 0$, at $1/J_x = 0$, as expected for decoupled $d = 1$ systems. The ordering transition continues to $1/J_x = 3.09$, to be compared with the exact result of $1/J_x = 2.27$ for the isotropic case $J_z/J_x = 1$. In the $J_z/J_x \to \infty$ limit, the ordering boundary again goes to infinite temperature.

3.5. Conclusion

It is seen that hard-spin mean-field theory yields a complete picture of the ordering and roughening phase transitions for the isotropic and anisotropic Ising models, in spatial dimensions $d = 3$ and 2. This result attests to the microscopic efficacy of the model. Future works, such as the effects of uncorrelated and correlated (aerogel [83, 84]) frozen impurities on the roughening transitions, are planned.

Chapter 4

SUCCESSIVELY THRESHOLDED DOMAIN BOUNDARY ROUGHENING DRIVEN BY PINNING CENTERS AND MISSING BONDS: HARD-SPIN MEAN-FIELD THEORY APPLIED TO $d = 3$ ISING MAGNETS

4.1. Introduction

Hard-spin mean-field theory [18, 19] has recently been applied to Ising magnets, correctly yielding the absence and presence of an interface roughening transition respectively in $d = 2$ and $d = 3$ dimensions and producing the ordering-roughening phase diagram for isotropic and anisotropic systems [see Chpt. 3]. The approach is now extended to the effects of quenched random pinning centers and missing bonds on the interface of isotropic and uniaxially anisotropic Ising models in $d = 3$. We find that these frozen impurities cause domain boundary roughening that exhibits consecutive thresholding transitions as a function of interaction anisotropy. We also find that, for both missing-bond and pinning-center impurities, for moderately large values of anisotropy, the systems saturate to the "solid-on-solid" limit, exhibiting a single universal curve for the domain boundary width as a function of impurity concentration.

4.2.   The Anisotropic $d = 3$ Ising Model with Impurities and Hard-Spin Mean-Field Theory

The $d = 3$ anisotropic Ising model is defined by the Hamiltonian (2.14). The system has ferromagnetic interactions $J_{xy}, J_z > 0$, periodic boundary conditions in the x and y directions, and oppositely fixed boundary conditions at the two terminal planes in the z spatial direction, which yields a domain boundary within the system when in the ordered phase. Thus, the system is generally uniaxially anisotropic. We systematically study the anisotropic $J_{xy} \neq J_z$ as well as the isotropic $J_{xy} = J_z$ cases.

In our current study, hard-spin mean-field theory [18, 19], which has been qualitatively and quantitatively successful in frustrated and unfrustrated, equilibrium and nonequilibrium magnetic ordering problems [35–41, 85–92], including recently the interface roughening transition [85], is used to study the roughening of an interface by quenched random pinning center sites or missing bonds. The coupled equations self-consistency equations of hard-spin mean-field theory (2.21) for all sites are solved by local numerical iteration, in a $10 \times 10 \times 10$ system.

4.3.   Domain Boundary Widths

4.3.1.   Determination of the Domain Boundary Width

In our study, the domain boundary is roughened in two ways: (1) Magnetic impurities are included in the system by pinning randomly chosen sites to $s_i = +1$ or to $s_i = -1$. The impurity concentration p in this case is the ratio of the number of pinned sites to the total number of sites. The numbers of $+1$ and -1 pinned sites are fixed to be equal, to give both domains an equal chance to advance over its counter. (2) Missing bonds are created by removing randomly chosen bonds. In this case, the concentration p is given by the ratio of the number of removed bonds to the total number of bonds when none is missing. The domain boundary width is calculated by first considering each yz plane. The boundary width in each yz plane is calculated by counting the number of sites, in the z direction, between the two furthest opposite magnetizations in the plane (Fig. 4.1). This number is averaged over all the yz planes. The result is then averaged over 100 independent realizations of the quenched randomness. We have checked that our results are robust with respect to varying the number of independent realizations of the quenched randomness, as shown below.

27
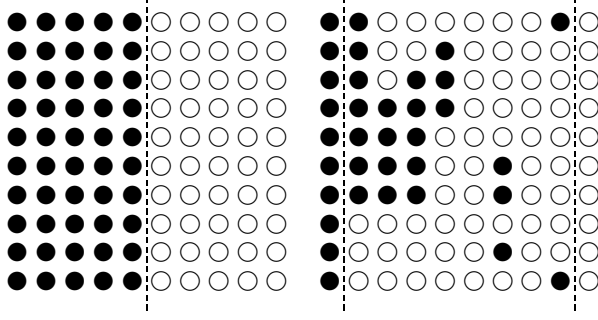
Figure 4.1: A yz plane at temperature $1/J_{xy} = 0.1$. Filled and empty circles respectively represent the calculated local magnetizations with $m_i > 0$ and $m_i < 0$. The left side is for the pure system, $p = 0$. The right side is calculated with quenched random pinning centers with concentration $p = 0.24$. Islands that are disconnected from the pinned z boundary plane of their own sign (typically occurring around an opposite pinning center deep inside a bulk phase) do not enter the interface width calculation and are not shown here. Thus, the disconnected pieces seen in this figure are actually part of an overhang, connected to the corresponding z boundary plane via the other yz planes. The dashed lines delimit the domain boundary and the separation between these dashed lines gives the domain boundary width in this yz plane. The same procedure for determining the interface width is also applied to the missing bond systems.

4.3.2. Impurity Effects on the Domain Boundary Width

Our calculated domain boundary widths, as a function of impurity (i.e., missing bond or pinned site) concentration p at temperature $1/J_{xy} = 0.1$, are shown in Fig. 4.2. The different curves are for different interaction anisotropies J_z/J_{xy}. In the lower panel for pinning-center impurity, the domain boundary roughens with the introduction of infinitesimal impurity, for all anisotropies: The curves have finite slope at the pure system. In the upper panel for missing-bond impurity, the domain boundary roughens with the introduction of infinitesimal impurity for strongly coupled planes $J_z/J_{xy} > 2.5$, whereas for weakly coupled planes $J_z/J_{xy} < 2.5$, it is seen that infinitesimal or small impurity has essentially no effect on the flat domain boundary. In the latter cases, the curves reach the pure system with zero slope.

For both missing-bond and pinning-center impurities, for moderately large values of J_z/J_{xy}, we find (Figs. 4.2 and 4.3) that the systems saturate to the $J_z/J_{xy} \to \infty$ "solid-on-solid" limit [93]. Thus, the systems exhibit a single universal curve for the domain boundary width as a function of impurity concentration, onwards from all moderately large values of J_z/J_{xy}.
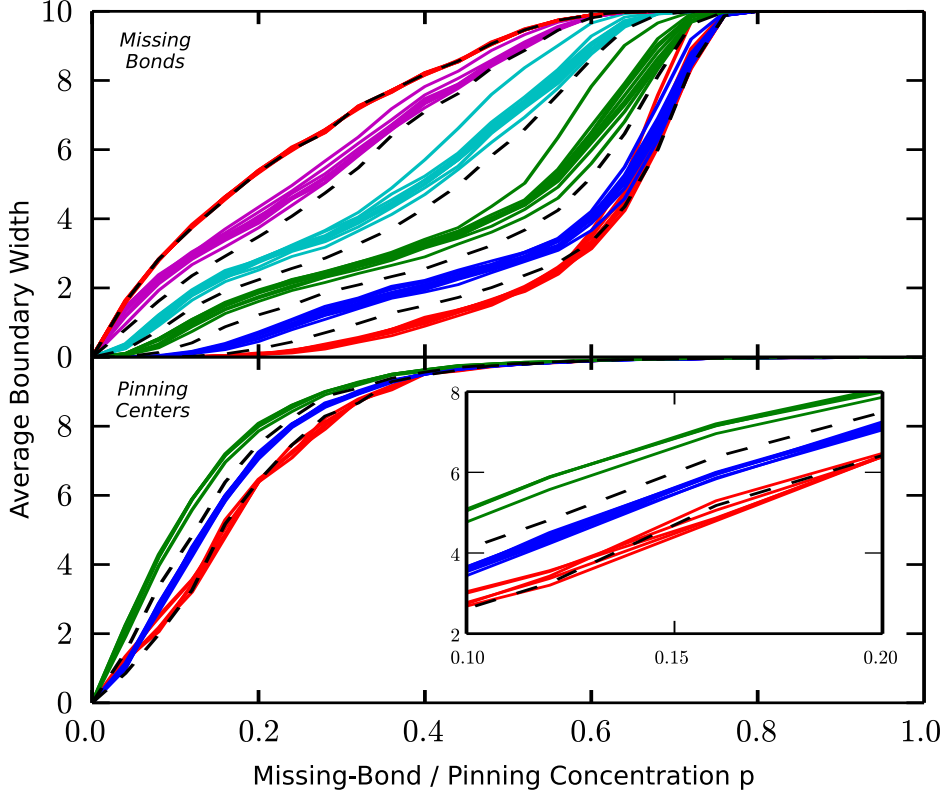
Figure 4.2: Calculated domain boundary widths versus impurity concentration p for different anisotropy J_z/J_{xy} values, at temperature $1/J_{xy} = 0.1$. In the upper panel, the horizontal axis p is the ratio of the number of missing bonds to the total number of bonds when none is missing. In the lower panel, the horizontal axis p is the ratio of the number of pinned sites to the total number of sites. In the upper panel for missing bonds, from the bottom to the top curves, the anisotropies are $J_z/J_{xy} = 0.1$ to 5.0 with 0.1 intervals and $J_z/J_{xy} = 5.5$ to 10 with 0.5 intervals. The dashed curves are calculated with the predicted threshold anisotropy values of $J_z/J_xy = 1, 2, 3, 4, 5$. In the lower panel for pinning centers, the anisotropies are $J_z/J_{xy} = 0.5$ to 2.5 with 0.1 intervals. The dashed curves are calculated with the predicted threshold anisotropy values of $J_z/J_{xy} = 1, 2$. Beyond $J_z/J_{xy} \simeq 5$ and 2.3, respectively for missing bonds and pinning centers, the system saturates to the $J_z/J_{xy} \to \infty$ "solid-on-solid" limit, exhibiting a single universal curve for the domain boundary width as a function of impurity concentration, for all $J_z/J_{xy} \geq 5$ and $J_z/J_{xy} \geq 2.3$ respectively.

4.3.3. Successive Roughening Thresholds

A bunching of the curves is visible, in the domain-boundary width curves in Fig. 4.2, especially in the upper panel for missing-bond impurity. This corresponds to a thresholded domain boundary roughening, controlled by the interaction anisotropy. This effect is also visible in Fig. 4.3, by the steps in the curves which give the domain boundary widths as a function of the interaction anisotropy J_z/J_{xy} for different impurity concentrations p, at temprature $1/J_{xy} = 0.1$. We have checked that our results are robust with respect to varying the number of independent realizations of the quenched randomness. This is shown in Fig. 4.4.

Thresholded domain boundary roughening can be understood by considering the ef-

fect of increasing the anisotropy. We first discuss the case of missing-bond impurity. Upon increasing J_z, for what value of J_z will a spin flip, e.g., from $+1$ to -1, thereby increasing the domain boundary width (directly and/or by inducing a flip cascade)? Increasing J_z can flip a spin and increase the width only if one of its bonds in the $\pm z$ direction is missing and the nonmissing bond connects to a -1 spin. This flip will then happen for $J_z = (q-q')J_{xy}$,

Figure 4.3: Calculated domain boundary widths versus anisotropy J_z/J_{xy}, at temperature $1/J_{xy} = 0.1$. The consecutive curves, bottom to top, are for impurity concentration values of $p = 0.04$ to 0.72 (top panel) and 1 (bottom panel) with 0.04 intervals. These values of p are noted next to the curves. In the upper panel, p is the ratio of the number of missing bonds to the total number of bonds when none is missing. In the lower panel, p is the ratio of the number of pinned sites to the total number of sites. The curves show the deviations from the isotropic case $J_z/J_{xy} = 1$ (vertical dash-dotted line) in the directions of strongly coupled planes $J_z/J_{xy} > 1$ or weakly coupled planes $J_z/J_{xy} < 1$. The predicted threshold values are shown with the vertical dash-dotted and dashed lines and are well reproduced by the calculated widths. It is clearly seen to the right of this figure that beyond $J_z/J_{xy} \simeq 5$ and 2.3, respectively for missing bonds and pinning centers, the system saturates to the $J_z/J_{xy} \to \infty$ "solid-on-solid" limit, exhibiting a single universal value for the domain boundary width as a function of impurity concentration, for all $J_z/J_{xy} \lesssim 5$ and $J_z/J_{xy} \gtrsim 2.3$ respectively.

where (q, q') are the number of xy neighbors bonded to the flipping spin that are, respectively, $+1$, -1. The possible values are $(q, q') = (4, 0), (3, 0), (2, 0), (1, 0), (3, 1), (2, 1)$, giving the thresholded values of $J_z/J_{xy} = 1, 2, 3, 4$, in fact calculationally seen in the top panels of Figs. 4.2 and 4.3. Furthermore, the simultaneous flip of two neighboring spins gives the threshold value of $J_z/J_{xy} = 5$, also calculationally seen in the top panels of Figs. 4.2 and 4.3. Beyond $J_z/J_{xy} = 5$, the system saturates to the $J_z/J_{xy} \to \infty$ "solid-on-solid" limit [93], exhibiting a single universal curve for the domain boundary width as a function of impurity concentration, for all $J_z/J_{xy} \gtrsim 5$.

We now discuss the case of pinned-site impurity. We again consider the effect of increasing J_z and investigate the value of J_z that wil flip the spin, e.g., from $+1$ to -1, thereby increasing the domain boundary width (again, directly and/or by inducing a flip
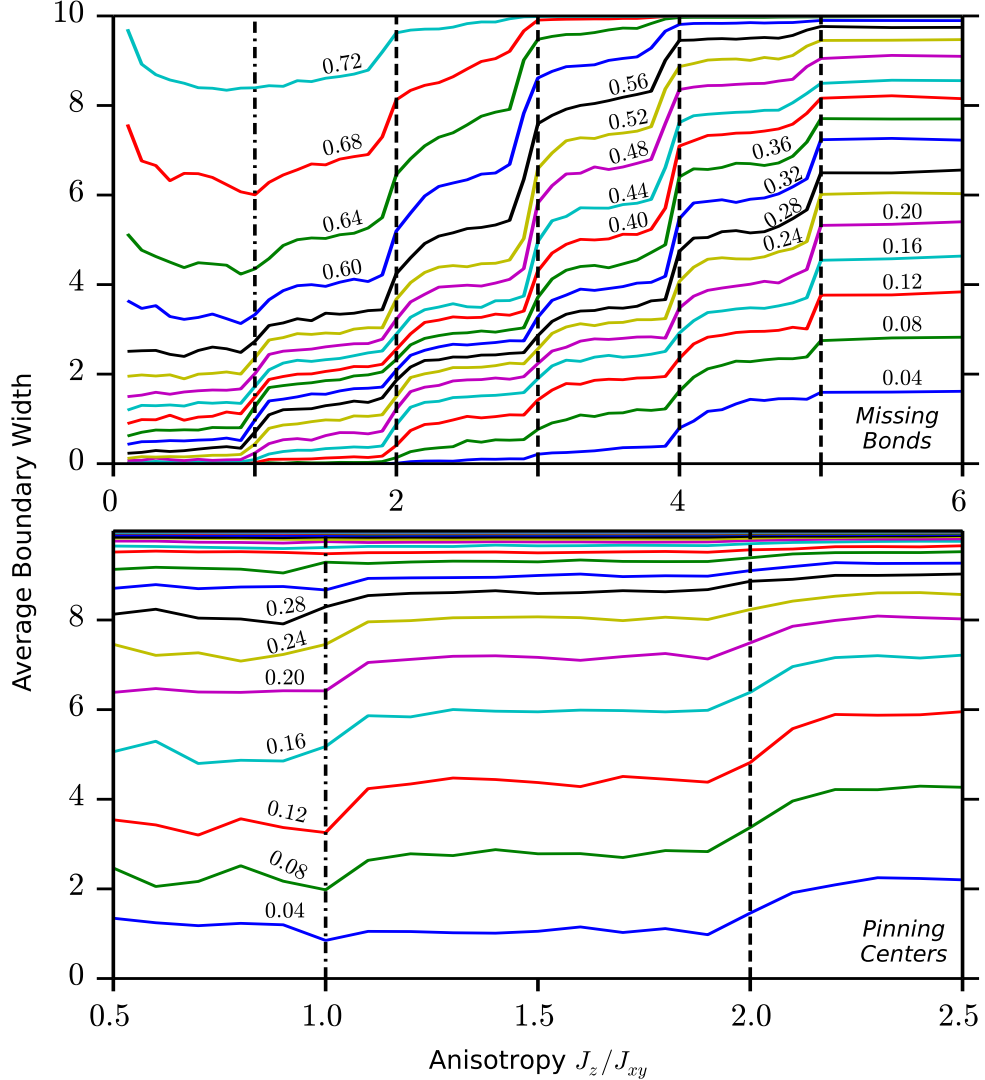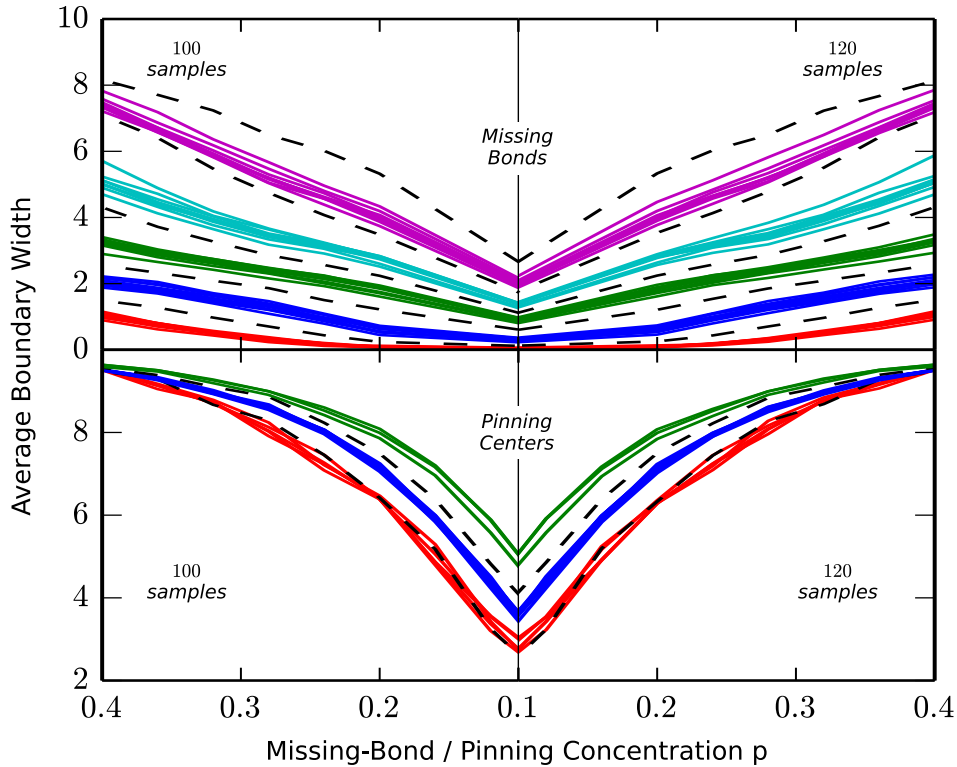

Figure 4.4: Calculated domain boundary widths versus impurity concentration p for different anisotropy J_z/J_{xy} values, at temperature $1/J_{xy} = 0.1$. There curves are obtained by averaging over 100 (left panels) and 120 (right panels) independent realizations of the quenched randomness. In the upper panel, the horizontal axis p is the ratio of the number of missing bonds to the total number of bonds when none is missing. In the lower panel, the horizontal axis p is the ratio of the number of pinned sites to the total number of sites. In the upper panel for missing bonds, from the bottom to the top curves, the anisotropies are $J_z/J_{xy} = 0.1$ to 5.0 with 0.1 intervals. The dashed curves are calculated with the predicted threshold anisotropy values $J_z/J_{xy} = 1, 2, 3, 4, 5$. In the lower panel for pinning centers, the anisotropies are $J_z/J_{xy} = 0.5$ to 2.3 with 0.1 intervals. The dashed curves are calculated with the predicted threshold anisotropy values of $J_z/J_{xy} = 1, 2$. Comparison of the left and right panels shows that our results are robust with respect to varying the number of independent realizations of the quenched randomness.
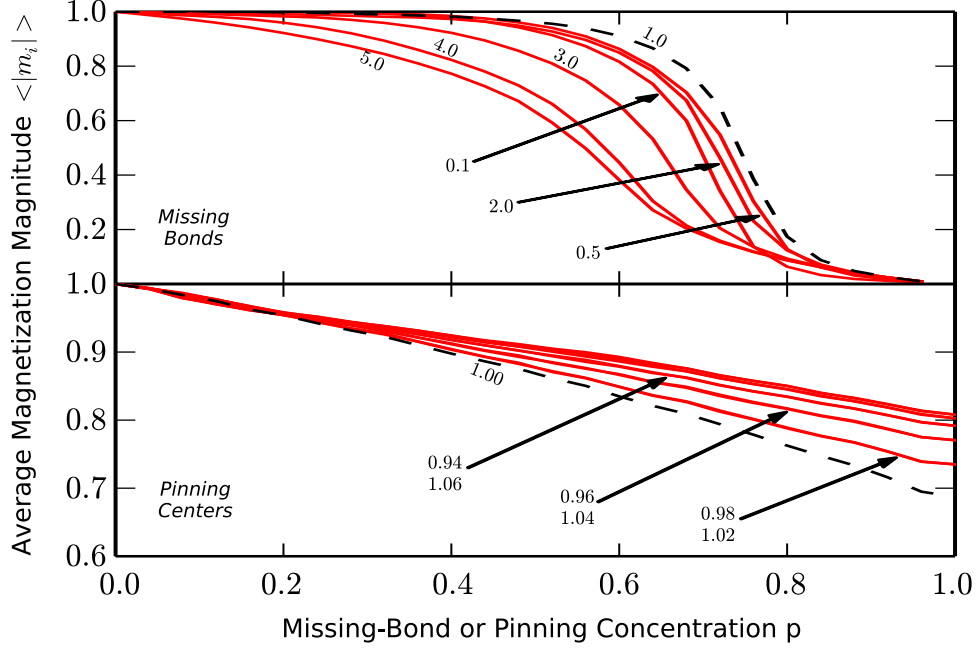
Figure 4.5: Calculated local magnetization magnitudes $\langle |m_i| \rangle$ averaged across the system versus impurity concentration p for different anisotropy J_z/J_{xy} values, at temperature $1/J_{xy} = 0.1$. In the upper panel, the horizontal axis p is the ratio of the number of missing bonds to the total number of bonds when none is missing. In the lower panel, the horizontal axis p is the ratio of the number of pinned sites to the total number of sites. In each panel, the dashed curve corresponds to the isotropic case $J_z/J_{xy} = 1$. The full curves are for the anisotropic cases. Some of the J_z/J_{xy} values for the anisotropic cases are indicated next to the corresponding curves. Note that the average magnetization magnitude curve of the isotropic case constitutes an upper boundary to the curves of the anisotropic cases for the missing bonds system (upper panel). The average magnetization magnitude curve of the isotropic case constitutes a lower boundary to the curves of the anisotropic cases for the pinning center system (lower panel). This is understandable by the fact that missing bonds weaken the connectivity and therefore the magnetization of the system, whereas pinning centers constitute a strong aligning field to their neighboring spins. In curves in the lower panel, the deviation from the isotropic case is symmetric, so that each curve corresponds to the values of the anisotropy J_z/J_{xy} which are above and below the isotropic case $J_z/J_{xy} = 1$.

cascade). Increasing J_z can flip this spin only if both of its neighbors in the $\pm z$ direction are -1, with one of these being part of a disconnected island seeded by a pinning center. This flip will then happen for $2J_z = (q - q')J_{xy}$, where again q and q' are the numbers of xy neighbors bonded to the flipping spin that are, respectively, $+1$ and -1. The possible values are $(q, q') = (4, 0), (3, 1)$, giving the threshold values of $J_z/J_{xy} = 1, 2$, calculationally seen in the bottom panels of Figs. 4.2 and 4.3. Beyond $J_z/J_{xy} \simeq 2.3$, the system saturates to the $J_z/J_{xy} \rightarrow \infty$ "solid-on-solid" limit [93], exhibiting a single universal curve for the domain boundary width as a function of impurity concentration, for all $J_z/J_{xy} \gtrsim 2.3$.

In a similar vein, in the limit of xy planes weakly coupled due to low J_z/J_{xy} and high concentration of missing bonds, the domain boundary gains by the intermediacy of

sending overhands in the lateral x and y directions, eventually covering the whole system via randomly magnetized xy planes. In this case, the spin is flipped by the effect of J_{xy} upon decreasing J_z. This flip occurs at $2J_z = (q - q')J_{xy}$, where (q, q') has to be such that J_z/J_{xy} is low. Thus $(q, q') = (2, 1)$. [Other pairs of values $(3, 0)$ and $(1, 0)$, do not contribute to this spread of overhangs.] Indeed in Fig. 4.3, a rise in the domain for decreasing $J_z < 0.5$ is seen at high missing bond concentration.

The curves in Fig. 4.3 are domain boundary widths that are affected by complicated (due to the random geometric distribution of the impurities) cascades of flips of groups of spins, occuring continuously as the interaction anisotropy is changed. The arguments given above are for single-spin flips, which strongly affect the boundary width at the specific anisotropy ratios.

We note that since in this system the interactions acting on a given spin s_i can be competing, due to the presence of the interface or of a neighboring pinning center, all of the local magnetizations $m_i = \langle s_i \rangle$, where the averaging is thermal, are not saturated even at low temperatures. Such an effect has been seen down to zero temperature in other systems with competing interactions, as for example shown in Fig. 3 of Ref. [94]. In our present study, the calculated magnitudes of the local magnetizations averaged across our current system, $\langle |m_i| \rangle$, are given in Fig. 4.5 and show this unsaturation.

4.3.4. Conclusion

The effects of quenched random pinning centers and missing bonds on the interface of isotropic and uniaxially anisotropic Ising models in $d = 3$ have been investigated by hard-spin mean-field theory. We find that the frozen impurities cause domain boundary roughening that exhibits consecutive thresholding transitions as a function of interaction anisotropy J_z/J_{xy}. The numerical results, showing the thresholding transitions as the bunching of domain boundary width versus impurity concentration curves (Fig. 4.2) and steps in the domain boundary width versus anisotropy curves (Fig. 4.3) agree with our spin-flip arguments at the interface. The threshold effect should be fully observable in experimental magnetic samples with good crystal structure and point impurities. For both missing-bond and pinning-center impurities, for moderately large values of J_z/J_{xy}, the systems saturate to the $J_z/J_{xy} \to \infty$ solid-on-solid limit, thus exhibiting a single universal curve for the domain boundary width as a function of impurity concentration, onwards from all moderately large values of J_z/J_{xy}.

Chapter 5

CHIRAL POTTS SPIN GLASS IN $d = 2$ AND 3 DIMENSIONS

5.1.   Introduction

Here, we focus on the extension of the chiral Potts model, mentioned in Section 2.2.3, by introducing quenched random left- and right-chiral interactions. We have studied the chiral spin-glass Potts system with $q = 3$ states in $d = 2$ and 3 spatial dimensions by renormalization-group theory and calculated the global phase diagrams (Fig. 5.1) in temperature, chirality concentration p, and chirality-breaking concentration c, also quantitatively determining phase chaos and phase-boundary chaos. In $d = 3$, the system has ferromagnetic, left-chiral, right-chiral, chiral spin-glass, and disordered phases. The phase boundaries to the ferromagnetic, left- and right-chiral phases show, differently, an unusual, fibrous patchwork (microreentrances) of all four (ferromagnetic, left-chiral, right-chiral, chiral spin-glass) ordered phases, especially in the multicritical region. The chaotic behavior of the interactions, under scale change, is determined in the chiral spin-glass phase and on the boundary between the chiral spin-glass and disordered phases, showing Lyapunov exponents in magnitude reversed from the usual ferromagnetic-antiferromagnetic spin-glass systems. At low temperatures, the boundaries of the left- and right-chiral phases become thresholded in p and c. In the $d = 2$, the chiral spin-glass Potts system does not have a spin-glass phase, consistently with the lower-critical dimension of ferromagnetic-antiferromagnetic spin glasses. The left- and right-chirally ordered phases show reentrance in chirality concentration p.

5.2.   The Chiral Potts Spin-Glass System

We extend the chiral Potts model mentioned in Section 2.2.3 by inducing quenched random left and right chirality. In the chiral Potts spin-glass model studied here, the
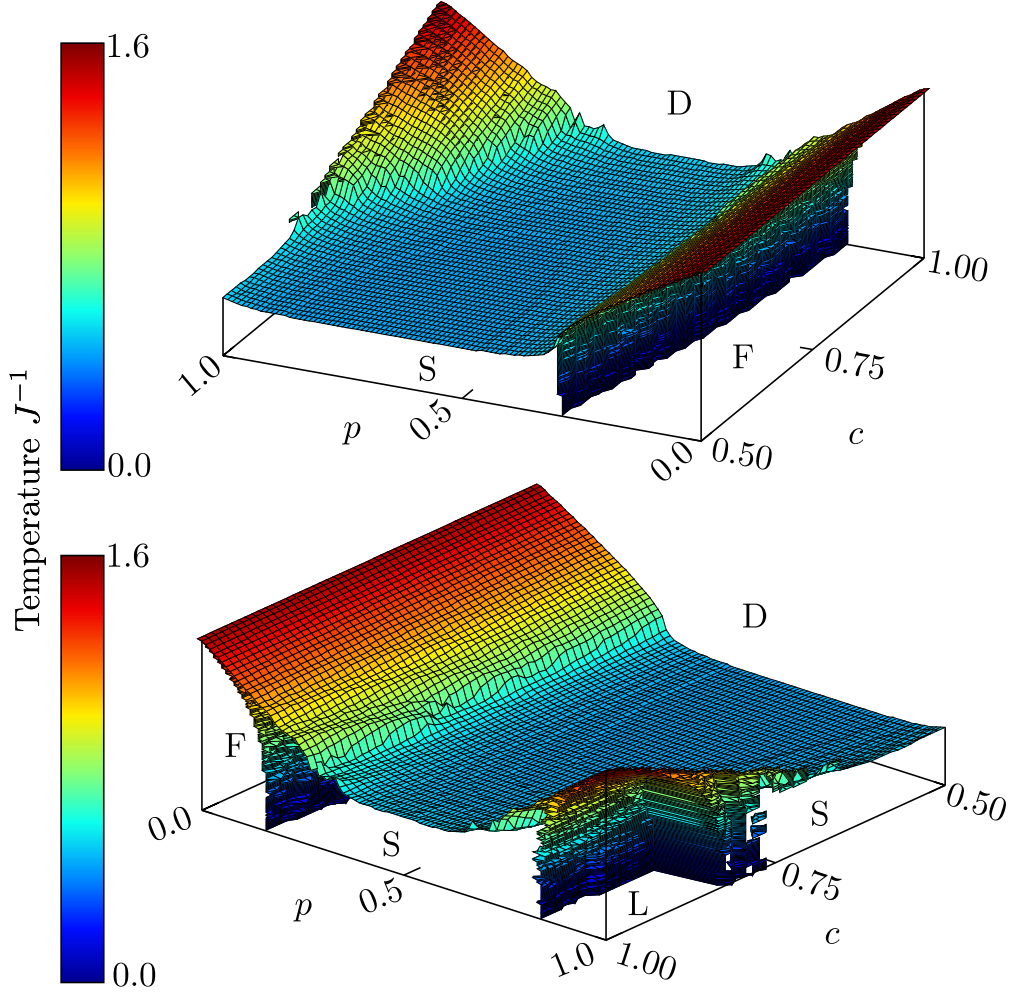
Figure 5.1: Calculated global phase diagram of the $d = 3$ chiral Potts spin glass, in temperature J^{-1}, chirality concentration p, and chirality-breaking concentration c. Note that the upper and lower figures are rotated with respect to each other. The ferromagnetically ordered phase (F), the chiral spin-glass phase (S), the left-chirally ordered phase (L), and the disordered phase (D) are marked. The global phase diagram is mirror-symmetric with respect to the chirality-breaking concentration $c = 0.5$, so that only $0.5 \leq c \leq 1$ is shown. In the (not shown) mirror-symmetric $0 \leq c \leq 0.5$ portion of the global phase dSiagram, the right-chirally ordered phase (R) occurs in the place of the left-chirally ordered phase (L) seen in this figure. Different cross-sections of this global phase diagram are shown in Figs. 5.3 and 5.4.

chirality of each nearest-neighbor interaction is randomly left-handed or right-handed or zero. This randomness is frozen (quenched) into the system and the overall fraction of left-, right-, and nonchirality is controlled by the quenched densities p and c as described below. Thus, the Hamiltonian of the chiral Potts spin-glass model is

$$-\beta\mathcal{H} = \sum_{\langle ij \rangle} J\Big[(1 - \eta_{ij})\delta(s_i, s_j) + \eta_{ij}[\phi_{ij}\delta(s_i, s_j + 1) + (1 - \phi_{ij})\delta(s_i, s_j - 1)]\Big], \quad (5.1)$$

where, for each pair of nearest-neighbor sites $\langle ij \rangle$, $\eta_{ij} = 0$ (nonchiral) or 1 (chiral). In the latter case, $\phi_{ij} = 1$ (left-handed) or 0 (right-handed). Thus, nonchiral, left-chiral, and right-chiral nearest-neighbor interactions are frozen randomly distributed in the entire
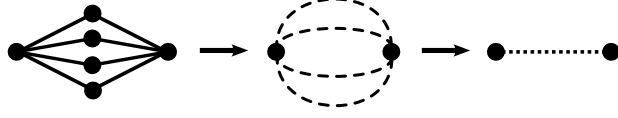
Figure 5.2: Renormalization-group transformation consisting of decimation followed by bond moving. The resulting recursion relations are approximate for the cubic lattice. The corresponding hierarchical lattice is obtained by the repeated self-imbedding of the leftmost graph. The recursion relations are exact for this $d = 3$ hierarchical lattice. For the $d = 2$, the number of parallel strands is 2 instead of 4 shown here.

system. For the entire system, the overall concentration of chiral interactions is given by p, with $0 \leq p \leq 1$. Among the chiral interactions, the overall concentrations of left- and right-chiral interactions are respectively, given by c and $1 - c$, with $0 \leq c \leq 1$. Thus, the model is chiral for $p > 0$ and chiral-symmetric $c = 0.5$, chiral-symmetry broken for $c \neq 0.5$. The global phase diagram is given in terms of temperature J^{-1}, chirality concentration p, and chirality-breaking concentration c (Figs. 5.1, 5.3 and 5.4).

Under the renormalization-group transformations described below, the Hamiltonian given in Eq. (5.1) maps onto the more general form

$$-\beta\mathcal{H} = \sum_{\langle ij \rangle} \left[J_0(ij)\delta(s_i, s_j) + J_+(ij)\delta(s_i, s_j + 1) + J_-(ij)\delta(s_i, s_j - 1) \right], \qquad (5.2)$$

where for each pair of nearest-neighbor sites $\langle ij \rangle$, the largest of the interaction constants (J_0, J_+, J_-) is set to zero, by subtracting the same constant G from each of (J_0, J_+, J_-), with no effect to the physics.

5.3. Renormalization-Group Transformation: Migdal-Kadanoff Approximation and Exact Hierarchical Lattice Solution

We solve the chiral Potts spin-glass model with $q = 3$ states by renormalization-group theory, in $d = 3$ spatial dimension, and with the length rescaling factor $b = 2$. Our solution is simultaneously, the Migdal-Kadanoff approximation [20, 21] for the cubic lattices and exact [44–48] for the $d = 3$ hierarchical lattice based on the leftmost graph of Fig. 5.2. The local renormalization-group transformation is achieved by a sequence, shown in Fig. 5.2, of decimations

$$e^{\tilde{J}_0(13)-\tilde{G}} = x_0(12)x_0(23) + x_+(12)x_-(23) + x_-(12)x_+(23),$$
$$e^{\tilde{J}_+(13)-\tilde{G}} = x_0(12)x_+(23) + x_+(12)x_0(23) + x_-(12)x_-(23), \qquad (5.3)$$
$$e^{\tilde{J}_-(13)-\tilde{G}} = x_0(12)x_-(23) + x_+(12)x_+(23) + x_-(12)x_0(23),$$

where $x_0(12) \equiv e^{J_0(12)}$, etc., and $\widetilde{G}$ is the subtractive constant mentioned in the previous section, and bond movings

$$J'_0(13) = \widetilde{J}^{(1)}_0(13) + \widetilde{J}^{(2)}_0(13) + \widetilde{J}^{(3)}_0(13) + \widetilde{J}^{(4)}_0(13),$$
$$J'_+(13) = \widetilde{J}^{(1)}_+(13) + \widetilde{J}^{(2)}_+(13) + \widetilde{J}^{(3)}_+(13) + \widetilde{J}^{(4)}_+(13), \qquad (5.4)$$
$$J'_-(13) = \widetilde{J}^{(1)}_-(13) + \widetilde{J}^{(2)}_-(13) + \widetilde{J}^{(3)}_-(13) + \widetilde{J}^{(4)}_-(13),$$

where primes mark the interactions of the renormalized system.

The starting trimodal quenched probability distribution of the interactions, characterized by p and c as described above, is not conserved under rescaling. Note that the interactions mentioned here includes more than one value at each locality, which is different than the interactions mentioned in Section 2.2.4. Therefore, the renormalized quenched probability distribution of the interactions is obtained by the convolution [49],

$$P'(\boldsymbol{J}(i'j')) = \int \left\{ \prod_{ij}^{i'j'} d\boldsymbol{J}(ij) P(\boldsymbol{J}(ij)) \right\} \delta(\boldsymbol{J}(i'j') - \boldsymbol{R}(\{\boldsymbol{J}(ij)\})), \qquad (5.5)$$

where $\boldsymbol{J} \equiv (J'_0, J'_+, J'_-)$ and $\boldsymbol{R}(\{\boldsymbol{J}(ij)\})$ represents the bond decimation and bond moving given in Eqs. (5.3) and (5.4). Similar previous studies, on other spin-glass systems, are in Refs. [32, 33, 53, 95–105], also mentioned in Section 2.2.4.

For numerical practicality, the bond moving of Eq. (5.4) is achieved by two sequential pairwise combination of interactions, each pairwise combination leading to an intermediate probability distribution resulting from a pairwise convolution as in Eq. (5.5). Furthermore, due to our convention of zeroing the largest interaction constant in each local triplet of interactions, the quenched probability distribution of three interactions $P(\boldsymbol{J}(ij))$ is conveniently just composed of the three probability distributions of two interactions, $P_0(J_+, J_-), P_+(J_0, J_-), P_-(J_+, J_-)$, where $P_0(J_+, J_-)$ has the (largest) interaction $J_0 = 0$, etc., which also considerably simplifies the numerical calculation. We effect this procedure numerically, by representing each probability distribution by histograms, as in previous studies [53, 96, 98–100, 102, 103, 105]. The probability distributions of two interactions $P_0(J_+, J_-), P_+(J_0, J_-),$ and $P_-(J_+, J_-)$ are represented via bivariate histograms with two-dimensional vectors (J_+, J_-) for P_0, etc. The number of histograms grow rapidly with each renormalization-group transformation, so that for calculational purposes, the histograms are binned when the number of histograms outgrow 40000 bins. In the calculation of chiral spin-glass phase-sink fixed distribution of Fig. 5.5, the histograms are binned after 10^8 histograms.

The different thermodynamic phases of the model are identified by the different asymp-
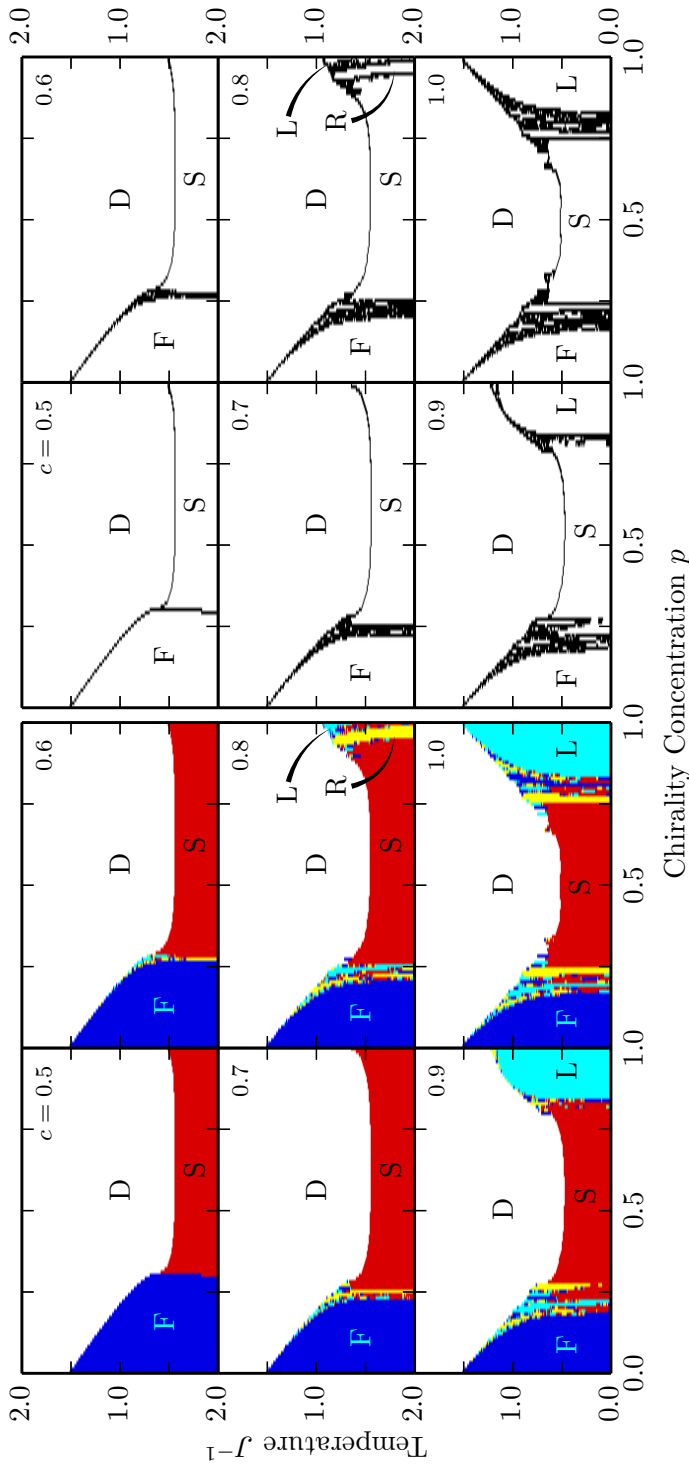
Figure 5.3: Cross-sections, in temperature J and chirality concentration p, of the global phase diagram shown in Fig. 5.1. The chirality-breaking concentration c is given on each cross-section. The ferromagnetically ordered phase (F), the chiral spin-glass phase (S), the left- and right-chirally ordered phases (L and R), and the disordered phase (D) are marked. Note that, as soon as the chiral symmetry of the model is broken by $c \neq 0.5$, a narrow fibrous patchwork (microreentrances) of all four (ferromagnetic, left-chiral, right-chiral, chiral spin-glass) ordered phases intervenes at boundaries of the ferromagnetically ordered phase F. This intervening region is more pronounced close to the multicritical region where the ferromagnetic, spin-glass, and disordered phases meet. The interlacing phase transitions inside this region are more clearly seen in the right-hand side panels of the figure, where only the phase boundaries are drawn in black. This intervening region gains importance as c moves away from 0.5. But it is only at higher values of the chirality-breaking concentration c, such as $c = 0.8$ on the figure, that the chirally ordered phase appears as a compact region at $c, p \lesssim 1$. In this case, again all four (ferromagnetic, left-chiral, right-chiral, chiral spin-glass) ordered phases intervene in a narrow fibrous patchwork at the boundaries of the chirally ordered phase L and R, the latter mirror-symmetric and not shown here. For $c = 1$, for which all interactions of the system are, with respective concentrations $1 - p$ and p, either ferromagnetic, or left-chiral, the phase diagram becomes symmetric with respect to $p = 0.5$ as in standard ferromagnetic-antiferromagnetic spin-glass systems, except that the chirally ordered phases dominate the fibrous patchwork on both sides of the phase diagram.

38
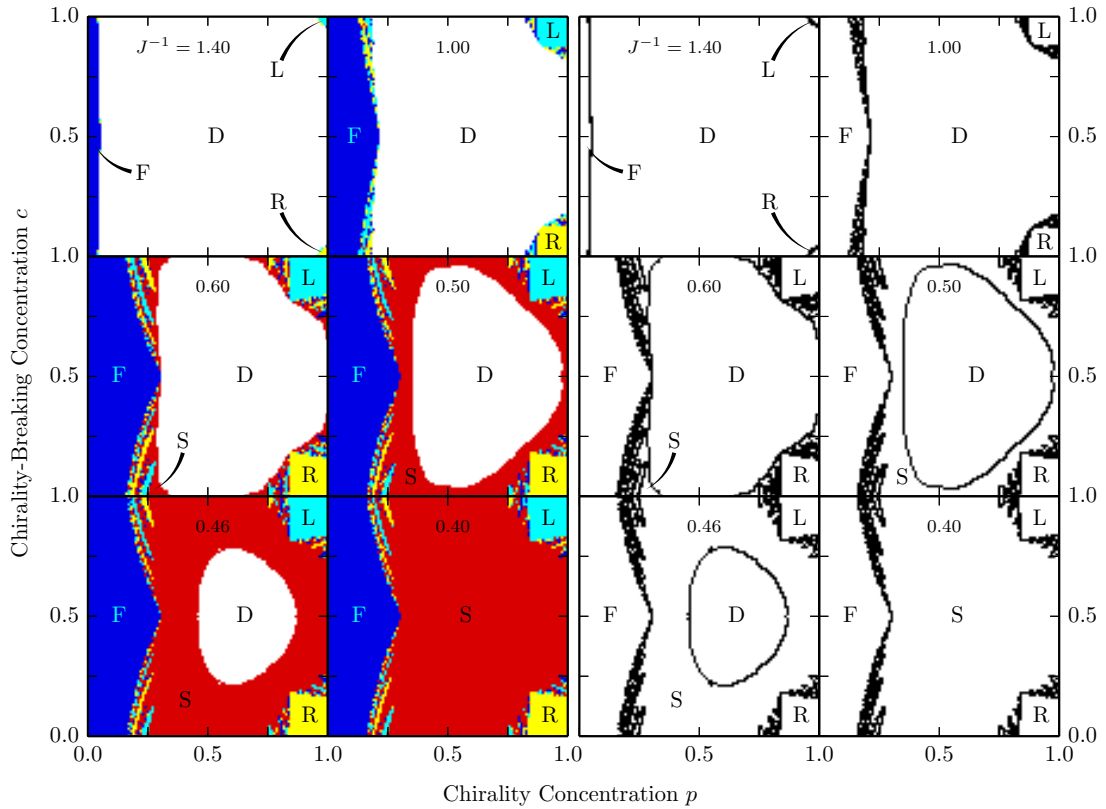
Figure 5.4: Cross-sections, in chirality concentration p and chirality-breaking concentration c, of the global phase diagram shown in Fig. 5.1. The temperature J^{-1} is given on each cross-section. The ferromagnetically ordered phase (F), the chiral spin-glass phase (S), the left-chirally ordered phase (L), the right-chirally ordered phase (R), and the disordered phase (D) are marked. Note the narrow fibrous patches (microreentrances) of all four (ferromagnetic, left-chiral, right-chiral, chiral spin-glass) ordered phases intervening at the boundaries of the ferromagnetically ordered phase F and at the boundaries of the chirally ordered phases L and R. It is seen here that, within these regions, the chirally ordered phases L and R form elongated lamellar patterns. These intervening phase transitions are more clearly seen in the right-hand side panels of the figure, where only the phase boundaries are drawn in black. Also note the temperature-independent square shape, at low temperatures, of the phase boundary of the chirally ordered phases, creating thresholds of $p = 0.84$ and $c = 0.84$ or 0.16 into L or R, respectively. This is also visible in the three-dimensional Fig. 5.1.

totic renormalization-group flows of the quenched probability distribution. For all renormalization-group flows, originating inside the phases and on the phase boundaries, Eq. (5.5) is iterated until asymptotic behavior is reached. Thus, we are able to calculate the global phase diagram of the chiral Potts spin-glass model.

5.4.   Chiral Potts Spin Glass: Calculated Global Phase Diagram

The calculated global phase diagram of the $d = 3$ chiral Potts spin-glass system, in temperature J^{-1}, chirality concentration p, and chirality-breaking concentration c, is given in Fig. 5.1. The ferromagnetically ordered (F) phase occurs at low temperature and low chirality p. The chiral spin-glass ordered (S) phase occurs at intermediate chirality p for all c and at high chirality p for intermediate c. The left- and right-chirally ordered phases L and R occur at high chirality p and values of chirality-breaking c away from 0.5. The disordered phase (D) occurs at high temperature. The global phase diagram is mirror-symmetric with respect to the chirality-breaking concentration $c = 0.5$, so that only $0.5 \leq c \leq 1$ is shown in Fig. 5.1. In the (not shown) mirror-symmetric $0 \leq c \leq 0.5$ portion of the global phase diagram, the right-chirally ordered phase (R) occurs in the place of the left-chirally ordered phase (L) seen in Fig. 5.1. Different cross-sections of the global phase diagram are shown in Figs. 5.3 and 5.4.

Under renormalization-group transformations, all points in the spin-glass phase are attracted to a fixed probability distribution of the quenched random interactions $P(J_0, J_+, J_-)$, namely to the sink of the chiral spin-glass phase. As explained in Section 5.3, $P(J_0, J_+, J_-)$ is composed of three distributions, $P_0(J_+, J_-)$, $P_+(J_0, J_-)$, and $P_-(J_0, J_+)$. Of these, $P_0(J_+, J_-)$ gives the quenched probability distribution of nearest-neighbor interactions in which the ferromagnetic interaction J_0 is dominant. Similarly, $P_+(J_0, J_-)$ and $P_-(J_0, J_+)$ give the quenched probability distributions of nearest-neighbor interactions in which, respectively, the left-chiral interaction J_+ and the right-chiral interaction J_- are dominant. (As explained in Section 5.2, by subtraction of an overall constant, the dominant interaction is set to zero and the other two, subdominant interactions are therefore negative, with no loss of generality.) The sink fixed distribution $P_0(J_+, J_-)$ is given in Fig. 5.5, where the average interactions $\langle J_\pm \rangle$ diverge to negative infinity as $b^{y_R n}$, where n is the number of renormalization-group iterations and $y_R = 0.32$ is the runaway exponent, while conserving the shape of the distribution shown in Fig. 5.5. The other two distributions $P_+(J_0, J_-)$ and $P_-(J_0, J_+)$ have the same sink distribution. Thus, in the chiral spin-glass
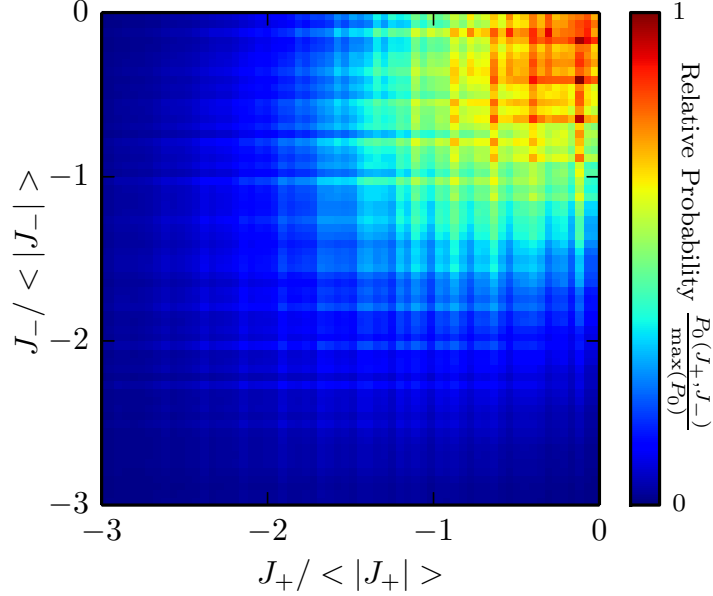
Figure 5.5: The fixed probability distribution of the quenched random interactions $P_0(J_+, J_-)$ to which all of the points in the chiral spin-glass phase are attracted under renormalization-group transformations, namely the sink of the chiral spin-glass phase. The average interactions $\langle J_\pm \rangle$ diverge to negative infinity as $\langle J_\pm \rangle \sim b^{y_R n}$, where n is the number of renormalization-group iterations and $y_R = 0.32$ is the runaway exponent, while $J_0 = 0$ (See Section 5.2). The other two distributions $P_+(J_0, J_-)$ and $P_-(J_0, J_+)$ have the same sink distribution. Thus, in the chiral spin-glass phase, chiral symmetry is broken local order, but not globally.

phase, chiral symmetry is broken by local order, but not globally.

We find here that the chaotic rescaling behavior, mentioned in Section 2.2.4, also occurs in our current spin-glass system with competing left- and right-chiral interactions, as shown in Fig. 5.6. In fact, the chaotic rescaling behavior occurs not only within the spin-glass phase, but also, quantitatively distinctly, at the phase boundary between the spin-glass and disordered phases [32]. This chaotic behavior at the phase boundary is also seen in the chiral system here and also shown in Fig. 5.6. The sum in Eq. (2.34) is to be taken within the asymptotic chaotic band, which is renormalization-group stable or unstable for the phase or its boundary, respectively. Thus, we throw out the first 100 renormalization-group iterations to eliminate the transient points outside of, but leading to the chaotic band. Subsequently, typically using 1000 renormalization-group iterations in the sum in Eq. (2.34) assures the convergence of the Lyapunov exponent value. Thus, the Lyapunov exponents that we obtain are numerically exact, to the number of digits given. We have calculated the Lyapunov exponents $\lambda = 1.77$ and 1.94, respectively, for the chiral spin-glass phase and for the boundary between the chiral spin-glass and disordered phases. At the chiral spin-glass phase-sink distribution, the average interaction diverges to negative infinity as $\langle J \rangle \sim b^{y_R n}$, where n is the number of renormalization-
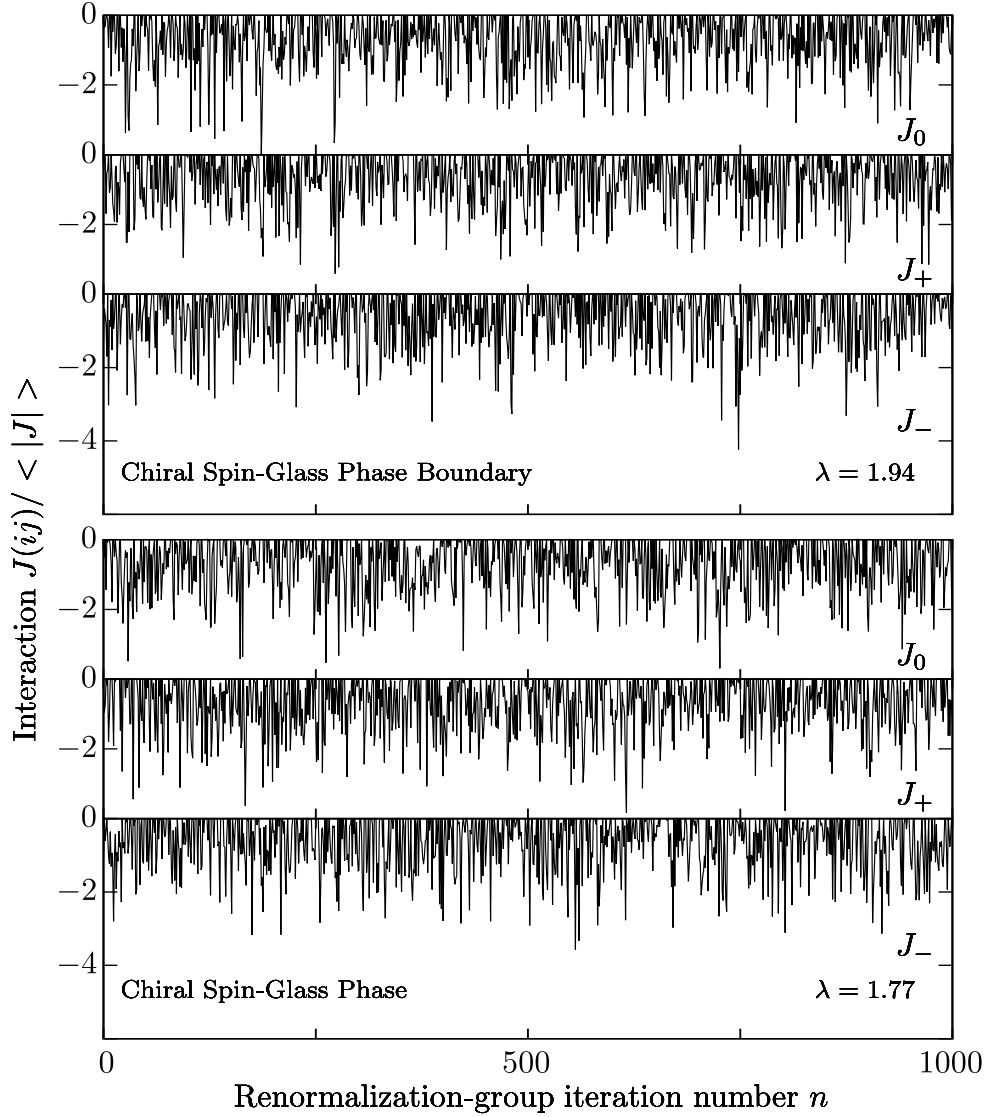
Figure 5.6: Chaotic renormalization-group trajectory: The three interactions at a given location, under consecutive renormalization-group transformations, are shown. Bottom panel: Inside the chiral spin-glass phase. The corresponding Lyapunov exponent is $\lambda = 1.77$ and the average interaction diverges as $\langle J \rangle \sim b^{y_R n}$, where n is the number of renormalization-group iterations and $y_R = 0.32$ is the runaway exponent. Top panel: At the phase boundary between the chiral spin-glass and disordered phases. The corresponding Lyapunov exponent is $\lambda = 1.94$ and the average nonzero interaction is fixed at $\langle J \rangle = -2.53$. The relative value of the Lyapunov exponents is unusual for spin-glass systems.

group iterations and $y_R = 0.32$ is the runaway exponent. At the fixed distribution of the phase boundary between the chiral spin-glass and disordered phases, the average interaction remains fixed at $\langle J \rangle = -2.53$. Interestingly, chaos is stronger at the boundary (larger Lyapunov exponent) than inside the chiral spin-glass phase. The opposite is seen in the usually studied $\pm J$ ferromagnetic-antiferromagnetic spin glass [32].

By contrast, in each of the ferromagnetic (F), left-chiral (L), and right-chiral (R) ordered phases, under consecutive renormalization-group transformations, the quenched probability distribution of the interactions sharpens to a δ function around a single value

receding to negative infinity for the respective pairs of interactions, namely (J_+, J_-), (J_0, J_+), and (J_0, J_-). There is no asymptotic chaotic behavior under renormalization-group in these phases F, L, and R.

Cross-sections of the global phase diagram, in temperature J^{-1} and chirality concentration p, are given in Fig. 5.3. The chirality-breaking concentration c is indicated for each cross-section. Note that, as soon as the chiral symmetry of the model is broken by $c \neq 0.5$, a narrow fibrous patchwork (microreentrances) of all four (ferromagnetic, left-chiral, right-chiral, chiral spin-glass) ordered phases intervenes at the boundaries between the ferromagnetically ordered phase F and the spin-glass phase S or the disordered phase D. This intervening regions is more pronounced close to the multicritical region where the ferromagnetic, spin-glass, and disordered phases meet. The interlacing phase transitions inside this region are more clearly seen in the right-hand side panels of Fig. 5.3, where only the phase boundaries are drawn in black. This intervening region gains importance as c moves away from 0.5. But it is only at higher values of the chirality-breaking concentration c, such as $c = 0.8$ on the figure, that the chirally ordered phase appears as a compact region at $c, p \lesssim 1$. In this case, again all four (ferromagnetic, left-chiral, right-chiral, chiral spin-glass) ordered phases intervene in a narrow fibrous patchwork at the boundaries of the chirally ordered phases L and R, the latter mirror symmetric and not shown here. For $c = 1$, for which all interactions of the system are, with respective concentrations $1 - p$ and p, either ferromagnetic, or left-chiral, the phase diagram becomes symmetric with respect to $p = 0.5$ as in standard ferromagnetic-antiferromagnetic spin-glass systems [17], except that the chirally ordered phases dominate the fibrous patchwork on both sides of the phase diagram.

Cross-sections, in chirality concentration p and chirality-breaking concentration c, of the global phase diagram are given in Fig. 5.4. The temperature J^{-1} is given on each cross-section. Note the narrow fibrous patches of all four (ferromagnetic, left-chiral, right-chiral, chiral spin-glass) phases intervening at the boundaries of the ferromagnetically ordered phase F and at the boundaries of the chirally ordered phases L and R. It is seen here that, within these regions, the chirally ordered phases L and R form elongated lamellar patterns. The interlacing phase transitions inside this region are more clearly seen in the right-hand side panels of the figure, where only the phase boundaries are drawn in black. It is again seen that the symmetry around $p = 0.5$ at the upper horizontal frame ($c = 1$) of each panel is broken inside the panel ($c < 1$). Also note the temperature-independent square shape, at low temperatures, of the phase boundary of the chirally ordered phases L and R, creating the threshold value of $p = 0.84$ and $c = 0.84$ or 0.16 into L or R, respectively. This is also visible in the three-dimensional Fig. 5.1
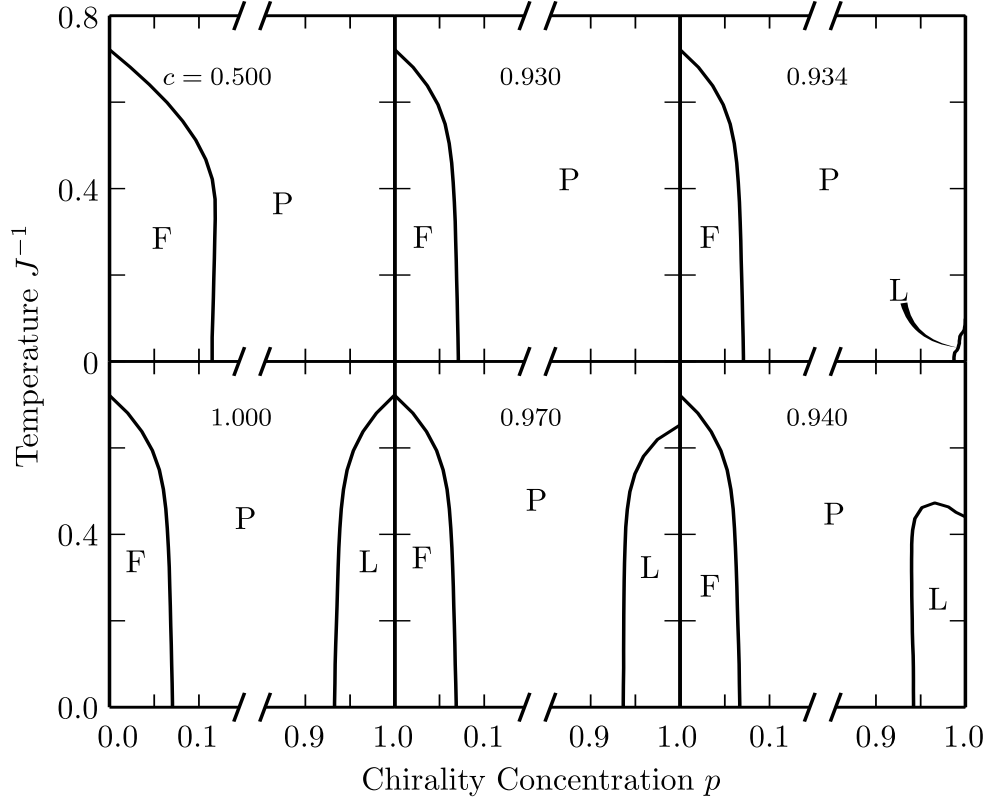
Figure 5.7: Representative cross-sections of the $d = 2$ chiral Potts spin-glass system, in temperature J^{-1} and chirality concentration p. The chirality-breaking concentration c is given on each cross-section. The ferromagnetically ordered phase (F), the left-chirally ordered phase (L), and the disordered phase (D) are marked. No chiral spin-glass phase occurs in $d = 2$ and no fibrous patchwork is seen at the phase boundaries. The chirally ordered phase appears for very high chirality-breaking concentration c (seen here for $c = 0.934$, but not seen for $c = 0.930$) and shows reentrance in chirality concentration p. This reentrance disappears as $c = 1$ is approached. For $c = 1$, for which all interactions of the system are, with respective concentrations $1 - p$ and p, either ferromagnetic or left-chiral, the phase diagram becomes symmetric with respect to $p = 0.5$ as in standard ferromagnetic-antiferromagnetic spin-glass systems.

5.5. Chiral Reentrance in $d = 2$

The global phase diagram of the $d = 2$ chiral Potts spin-glass system is given in Fig. 5.7. Representative cross-sections in temperature J^{-1} and chirality concentration p are shown. The chirality-breaking concentration c is given on each cross-section. The ferromagnetically ordered phase (F), the left-chirally ordered phase (L), and the disordered phase (D) are marked. No chiral spin-glass phase occurs in $d = 2$ and no fibrous patchwork is seen at the phase boundaries. The chirally ordered phase appears for very high chirality-breaking concentration c (seen here for $c = 0.934$, but not seen for $c = 0.930$) and shows reentrance [30, 106–111] in chirality concentration p. This reentrance disappears as $c = 1$ is approached. For $c = 1$, for which all interactions of the system are, with respective concentrations $1 - p$ and p, either ferromagnetic, or left-chiral, the

phase diagram becomes symmetric with respect to $p = 0.5$ as in standard ferromagnetic-antiferromagnetic spin-glass systems [53].

The absence of the chiral spin-glass phase in $d = 2$ is consistent with standard ferromagnetic-antiferromagnetic Ising spin-glass systems, where the lower-critical dimension for the spin-glass phase is found around 2.5 [105, 112–115]. Below this dimension, no spin-glass phase appears (unless some nanorestructuring is done to the system [53]).

5.6. Conclusion

We have thus obtained the global phase diagram of the chiral spin-glass Potts system with $q = 3$ states in $d = 3$ and 2 spatial dimensions by renormalization-group theory that is approximate for the cubic lattice and exact for the hierarchical lattice. Unusual features have been revealed in $d = 3$. The phase boundaries to the ferromagnetic, left- and right-chiral phases show, differently, an unusual, fibrous patchwork (microreentrances) of all four (ferromagnetic, left-chiral, right-chiral, chiral spin-glass) ordered phases, especially in the multicritical region. In $d = 3$, there is a chiral spin-glass phase. Quite unusually, the phase boundary between the chiral spin-glass and disordered phases is more chaotic than the chiral spin-glass phase itself, as judged by the magnitudes of the respective Lyapunov exponents. At low temperatures, the boundaries of the left- and right-chiral phases become temperature-independent and thresholded in chirality concentration p and chirality-breaking concentration c. In the $d = 2$, thie chiral spin-glass system does not have a spin-glass phase, consistently with the lower-critical dimension of ferromagnetic-antiferromagnetic spin glasses. The left- and right-chirally ordered phases show reentrance in chirality concentration p.

Chapter 6

DEVIL'S STAIRCASE CONTINUUM IN THE CHIRAL CLOCK SPIN GLASS WITH COMPETING FERROMAGNETIC-ANTIFERROMAGNETIC AND LEFT-RIGHT CHIRAL INTERACTIONS

6.1. Introduction

The presence of chiral interactions, motivated by experimental systems [26–30], can result in extremely rich phase transition phenomena in otherwise simple systems [116]. In this respect, we study here a $q = 5$ state clock spin-glass model in $d = 3$ spatial dimensions, using renormalization-group theory. Our system has both competing ferromagnetic and antiferromagnetic interactions, as in the usually studied spin-glass models [17], and competing left-chiral and right-chiral interactions [116]. We have studied $q = 5$ states, beacause odd numbers of states have built-in entropy for antiferromagnetic interactions, even without quenched randomness and frustration [33].

The global phase diagram is calculated in temperature, antiferromagnetic bond concentration p, random chirality strength, and right-chirality concentration c. We find an extremely rich phase diagram, with a ferromagnetic phase, a multitude of different chiral phases, a chiral spin-glass phase, and a critical (algebraically) ordered phase [117, 118]. The ferromagnetic and chiral phases accumulate at the disordered phase boundary and form devil's staircases [23, 119], where different ordered phases characteristically intercede at alll scales of phase-diagram space. In fact, a continuum of devil's staircases is found. Shallow and deep reentrances of the disordered phase, bordered by fragments of

regular and temperature-inverted devil's staircases, are seen. The extremely rich phase diagrams are presented as continuously and qualitatively changing videos [120].

6.2. The $q-$State Chiral Clock Double Spin Glass

The q-state clock spin glass mentioned in Section 2.2.3 is extended to double spin glass systems, by introducing the competing left- and right-chiral interactions [see Chpt. 5] to clock systems. In the q-state chiral clock double spin glass introduced here, frustration also occurs via randomly frozen left or right chirality [116]. The Hamiltonian in Eq. (2.17) is therefore generalized to random local chirality,

$$-\beta\mathcal{H} = \sum_{\langle ij \rangle} \left[J_{ij} \cos\theta_{ij} + \Delta\delta\left(\theta_{ij} + \eta_{ij}\frac{2\pi}{q}\right) \right]. \tag{6.1}$$

In a cubic lattice, the x, y, or z coordinates increase as sites along the respective coordinate direction are considered. Bond moving as in Fig. 6.1(a) is done transversely to the bond directions, so that this sequencing is respected. Equivalently, in the corresponding hierarchical lattice, one can always define a direction along the connectivity, for example, from left to right in Fig. 6.1(b), and assign consecutive increasing number labels to the sites. In Eq. (6.1), for each pair of nearest-neighbor sites $\langle ij \rangle$ the numerical site label j is ahead of i, frozen (quenched) $\eta_{ij} = 1$ (left chirality) or -1 (right chirality), and the δ function $\delta(x) = 1(0)$ for $x = 0(x \neq 0)$. The overall concentrations of left and right chirality are respectively $1 - c$ and c, with $0 \leq c \leq 1$. The strength of the random chiral interaction is Δ/J, with temperature divided out. With no loss of generality, we take $\Delta \geq 0$. Thus, the system is chiral $\Delta > 0$, chiral symmetric for $c = 0.5$, and chiral symmetry broken for $c \neq 0.5$. The global phase diagram is in terms of temperature J^{-1}, antiferromagnetic bond concentration p, random chirality strength Δ/J, and chiral symmetry-breaking concentration c.

6.3. Renormalization-Group Method: Migdal-Kadanoff Approximation and Exact Hierarchical Lattice Solution

We solve the chiral clock double spin-glass model with $q = 5$ states by renormalization-group theory, in $d = 3$ spatial dimensions, with length rescaling factor $b = 3$. We use $b = 3$, as in previous position-space renormalization-group calculations of spin-glass sys-
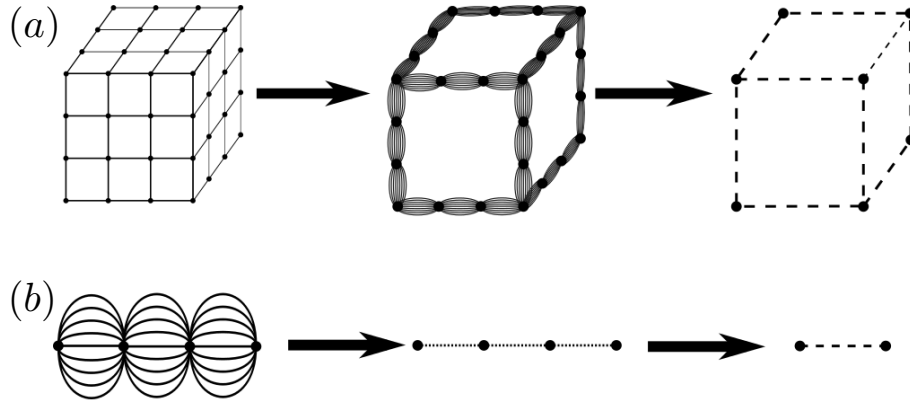
Figure 6.1: (a) The Migdal-Kadanoff approximate renormalization-group transformation for the cubic lattice, composed of the bond-moving followed by decimation steps, with the length rescaling factor $b = 3$. The corresponding hierarchical lattice is obtained by the repeated self-imbedding of the leftmost graph in panel (b).(b) The exact renormalization-group transformation for this $d = 3$ hierarchical lattice. The two procedures yield identical recursion relations.

tems, because it treats ferromagnetism and antiferromagnetism on equal footing. Our solution is simultaneously, the Migdal-Kadanoff approximation [20, 21] for the cubic lattice and the exact solution [44–48] for the $d = 3$ hierarchical lattice based on the repeated self-imbedding of leftmost graph of Fig. 6.1(b). Fig. 6.1(a) shows the Migdal-Kadanoff approximate renormalization-group transformation for the cubic lattice, composed of the bond-moving followed by decimation steps. Fig. 6.1(b) shows the exact renormalization-group transformation for the hierarchical lattice. The two procedures yield identical recursion relations.

Exact calculations on hierarchical lattices are also currently widely used on a variety of statistical mechanics problems [121–137]. On the other hand, this approximation for the cubic lattice is an uncontrolled approximation, as in fact are all renormalization-group theory calculations. However, as noted before [138], the local summation in position-space technique used here has been qualitatively, near quantitatively, and predictively successful in a large variety of problems, such as arbitrary spin-s Ising models [139], global Blume-Emery-Griffiths model [140], first- and second-order Potts transitions [141, 142], antiferromagnetic Potts critical (algebraically ordered) phases [117, 118], ordering [31] and superfluidity [143] on surfaces, multiply reentrant liquid crystal phases [106, 107], chaotic spin glasses [50], random-field [144, 145] and random temperature [146, 147] magnets including the remarkably small $d = 3$ magnetizaion critical exponent β of the random-field Ising model, and high-temperature superconductors [148]

Under the renormalization-group transformation described below, the Hamiltonian of

Eq. (6.1) maps onto the more general form

$$-\beta\mathcal{H} = \sum_{\langle ij\rangle} V_{ij}(\theta_{ij}), \qquad (6.2)$$

where $\theta_{ij} = \theta_i - \theta_j$ can take q different values, so that for each pair $\langle ij\rangle$ of nearest-neighbor sites, there are q different interaction constants

$$\{V_{ij}(\theta_{ij})\} = \{V_{ij}(0), V_{ij}(\delta), V_{ij}(2\delta), V_{ij}(3\delta), V_{ij}(4\delta)\} \equiv \boldsymbol{V}_{ij}, \qquad (6.3)$$

which are in general different at each locality (quenched randomness). Here, $\delta \equiv 2\pi/5$ is the angle between consecutive clock-spin directions. The largest element of $\{V_{ij}(\theta_{ij})\}$ at each locality $\langle ij\rangle$ is set to zero, by subtracting the same constant G from all q interaction constants, with no effect on the physics; thus, the $q-1$ other interaction constants are negative.

The local renormalization-group transformation is achieved by the sequence, shown in Fig. 6.1, of bond movings

$$\widetilde{V}_{ij}(\theta_{ij}) - \widetilde{G} = \sum_{k=1}^{b^{d-1}} V_{ij}^{(k)}(\theta_{ij}), \qquad (6.4)$$

and decimations

$$e^{V'_{14}(\theta_{14}) - G} = \sum_{\theta_2, \theta_3} e^{\widetilde{V}_{12}(\theta_{12}) + \widetilde{V}_{23}(\theta_{23}) + \widetilde{V}_{34}(\theta_{34})}, \qquad (6.5)$$

where $\widetilde{G}$ and G are the subtractive constants mentioned above, and prime marks the interaction of the renormalized system.

The starting double-bimodal quenched probability distribution of the interactions, characterized by p and c as described above, is not conserved under rescaling. Recall that we adapted the convolution from (2.33) to the multiinteraction case in Chpt. 5. Here, we apply a similar approach, to obtain the renormalized quenched probability distribution of the interactions by the convolution [49]

$$P'(\boldsymbol{V}'_{i'j'}) = \int \left\{ \prod_{ij}^{i'j'} d\boldsymbol{V}_{ij} P(\boldsymbol{V}_{ij}) \right\} \delta(\boldsymbol{V}'_{i'j'} - \boldsymbol{R}(\{\boldsymbol{V}_{ij}\})), \qquad (6.6)$$

where $\boldsymbol{V}_{ij} \equiv \{V_{ij}(\theta_{ij})\}$ as in Eq. (6.3), $\boldsymbol{R}(\{\boldsymbol{V}_{ij}\})$ represents the bond moving and bond decimation given in Eqs. (6.4) and (6.5), and primes refer to the renormalized system. Similar previous studies, on other spin-glass systems are in Refs. [32, 33, 53, 95–97, 99–101, 105]. For numerical practicality, the bond moving and decimation of Eqs. (6.4) and (6.5) are achieved by a sequential pairwise combination of interactions, each pairwise

combination leading to an intermediate probability distribution resulting from a pairwise convolution as in Eq. (6.6).

We effect this procedure numerically, first starting with the initial double δ distribution of Eq. (6.1), giving 4 possible interactions quenched randomly distributed throughout the system, and generating 1000 interactions that embody the quenched probability distribution resulting from the pairwise combination. Each of the generated 1000 interactions is described by q interaction constants, as explained above [Eq. (6.3)]. At each subsequent pairwise convolution as in Eq. (6.6), 1000 randomly chosen pairs, representing quenched random neighbors in the lattice, are matched by (6.4) or (6.5), and a new set of 1000 interactions is produced. As a control, we have also calculated phase diagrams given below using 1500 interactions and the phase diagrams did not change.

Our calculation simply consists in following the recursion relations, Eqs. (6.4)–(6.6), to the various fixed points and thereby mapping the initial conditions that are the basins of attraction of the various fixed points. This map is the phase diagram: The different thermodynamic phases of the system are identified by the different asymptotic renormalization-group flows of the quenched probability distribution $P(\boldsymbol{V}_{ij})$. Two renormalization-group trajectories starting at each side of a phase boundary point diverge from each other, flowing towards the phase sinks (completely stable fixed points) of their respective phases. Thus, the phase boundary point between two phases is readily obtained to the accuracy of the figures. We are therefore able to calculate the global phase diagram of the chiral clock double spin-glass model.

6.4.   Global Phase Diagram of the $q = 5$ State Chiral Clock Double Spin Glass

The global phase diagram of the $q = 5$ state chiral clock double spin-glass model in $d = 3$ spatial dimensions, in temperature J^{-1}, antiferromagnetic bond concentration p, random chirality strength Δ/J, and right-chirality concentration c, is a four-dimensional object, so that only the cross sections of the global phase diagram are exhibited.

Figure 6.2 shows the calculated sequence of phase diagrams for the ferromagnetic $(p = 0)$, on the left side of the figure, and antiferromagnetic $(p = 1)$, on the right side, systems with quenched random left- and right-chiral interactions. The horizontal axis c is the concentration of right-chiral interactions. Phase diagrams for different random chirality strengths Δ/J are shown. The system exhibits ferromagnetic (F), a multitude of different chiral, and spin-glass (S) ordered phases. The antiferromagnetic system also
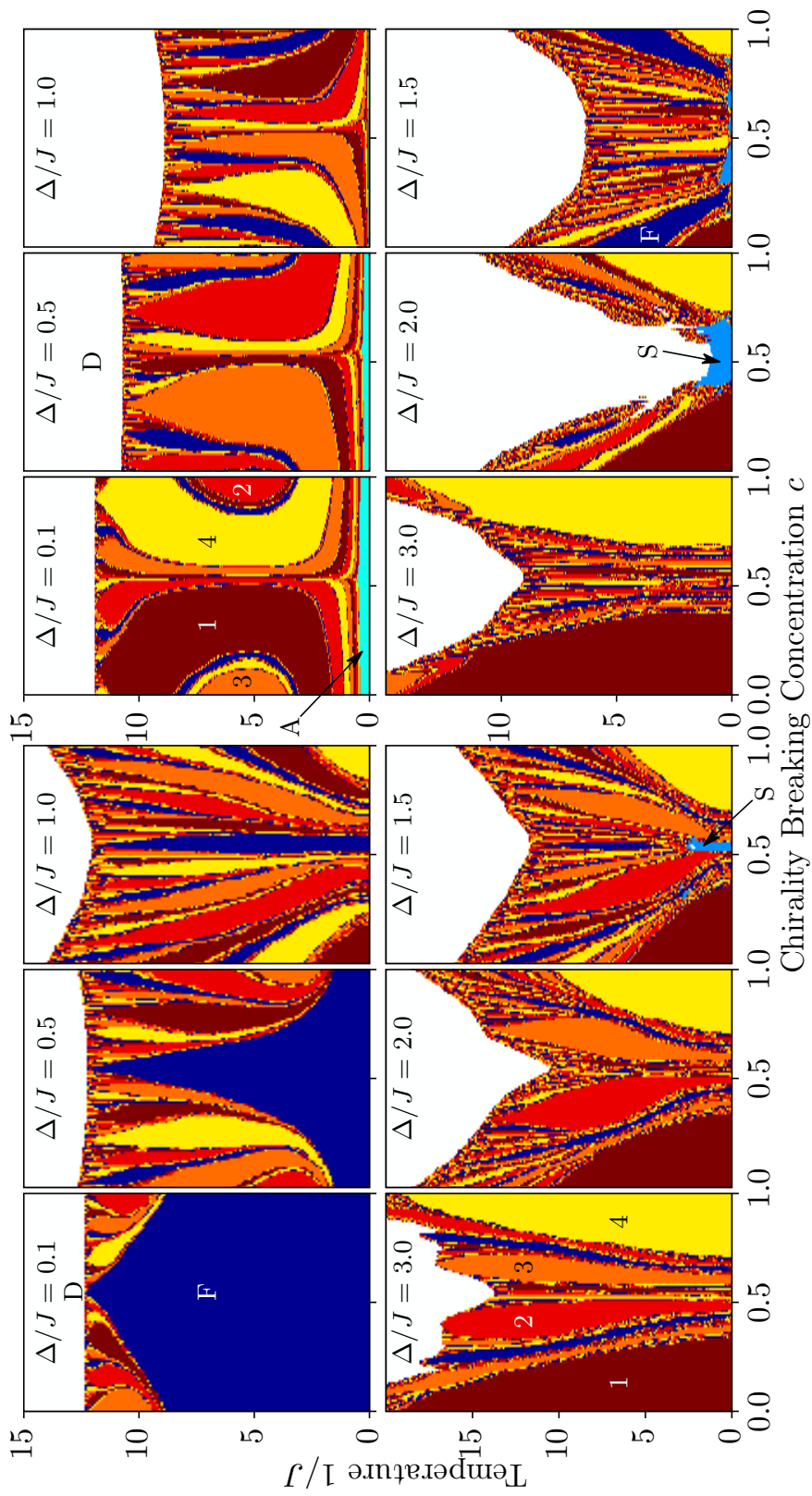
Figure 6.2: Calculated sequence of phase diagrams for the ferromagnetic ($p = 0$), on the left side of the figure, and antiferromagnetic ($p = 1$), on the right side, systems with quenched random left- and right-chiral interactions. The horizontal axis c is the concentration of right-chiral interactions. Phase diagrams for different random chirality strengths Δ/J are shown. The system exhibits ferromagnetic (F), a multitude of different chiral, and spin-glass (S) ordered phases. On some of the chiral phases, the δ multiplicity of the asymptotically dominant interaction is indicated. The ferromagnetic and chiral phases accumulate as different devil's staircases at their boundary with the disordered (D) phase. The antiferromagnetic system also exhibits an algebraically ordered (A) phase. The full richness of the continuum of widely varying devil's staircase phase diagrams can also be seen in video form, four of which are accessible as Supplemental Material [120]

51

shows an algebraically (A) ordered (critical) phase, in which every point is a critical point with divergent correlation length [117, 118]. In all cases, the ferromagnetic and different chiral phases accumulate as different devil's staircases [23, 119] at their boundary with the disordered (D) phase. The definition of the devil's staircase is that this accumulation is seen at every expanded scale of the phase diagram variables. This accumulation at every expanded phase diagram scale is indeed revealed from our calculations, as seen further below.

Figure 6.3 shows the calculated sequence of phase diagrams for the left chiral ($c = 0$), on the upper side, and quenched random left and right chiral ($c = 0.5$), on the lower side, system with, in both cases, quenched random ferromagnetic and antiferromagnetic interactions. The horizontal axis is the random chirality strength Δ/J. The consecutive phase diagrams are for different concentrations of antiferromagnetic interactions p. The system exhibits ferromagnetic (F), a multitude of different chiral, spin-glass (S), and algebraically ordered (A) phases. The ferromagnetic and different chiral phases accumulate as different devil's staircases [23, 119] at their boundary with the disordered (D) phase. Note shallow and deep reentrances of disorder [107–110] at $p = 0.4$ and $p = 0.7$, respectively, surrounded by regular and temperature-inverted devil's staircases.

Figure 6.4 shows the phase diagram cross section in the upper left of Fig. 6.3, with calculated 10-fold and 100-fold zoom. The devil's staircase structure appears at each zoom level.

The full richness of the continuum of widely varying devil's staircase phase diagrams can best be seen in video form, four of which are accessible as Supplemental Material [120]. These videos effectively exhibit a very large number of calculated phase diagram cross sections.

6.5.   Entire-Phase Criticality, Differentiated Chaos in the Spin-Glass and at Its Boundary

The renormalization-group mechanism for the algebraically ordered (critical) phase is that all renormalization-group trajectories originating inside this phase flow to a completely stable fixed point (sink) that occurs at finite temperature (finite coupling strength) [117, 118, 149–157]. In all other ordered phases, the trajectories flow to strong (infinite) coupling.

In the ferromagnetic phase, the interaction $V_{ij}(0)$ becomes asymptotically dominant. In the chiral phases, in the renormalization-group trajectories, one of the chiral inter-
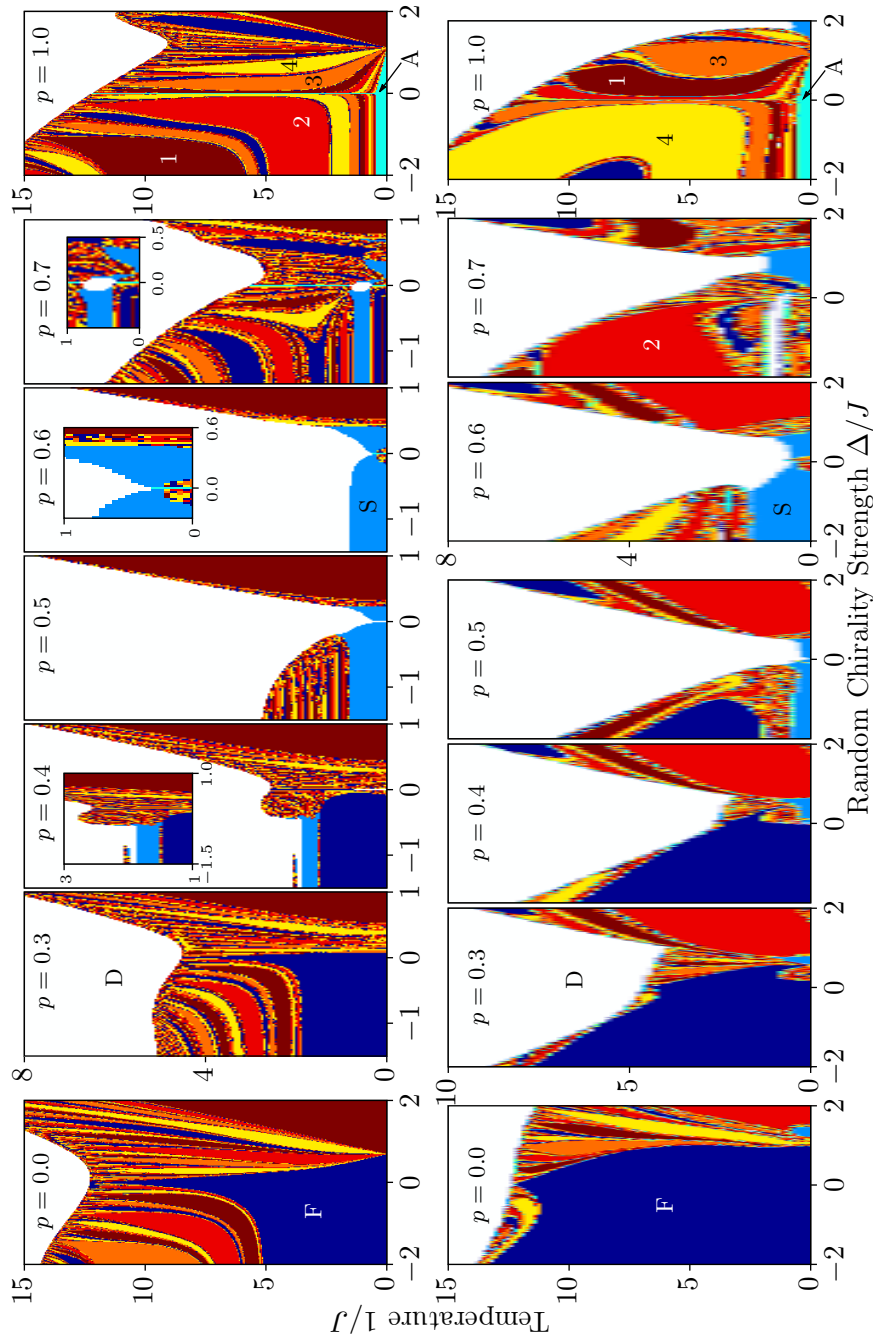
Figure 6.3: Calculated sequence of phase diagrams for the left-chiral ($c = 0$), on the upper side of the figure, and quenched random left- and right-chiral ($c = 0.5$), on the lower side, systems with quenched random ferromagnetic and antiferromagnetic interactions. The horizontal axis is the random chirality strength Δ/J. The consecutive phase diagrams are for different concentrations of antiferromagnetic interactions p. The system exhibits ferromagnetic (F), a multitude of different chiral, spin-glass (S), and critical (algebraically) ordered (A) phases. On some of the chiral phases, the δ multiplicity of the asymptotically dominant interaction is indicated. The ferromagnetic and chiral phases accumulate as different devil's staircases at their boundary with the disordered (D) phase. Note shallow and deep reentrances of the disordered phase at $p = 0.4$ and $p = 0.7$, respectively, surrounded by regular and temperature-inverted devil's staircase. The full richness of the continuum of widely varying devil's staircase phase diagrams can also be seen in video form, four of which are accessible as Supplemental Material [120].

53
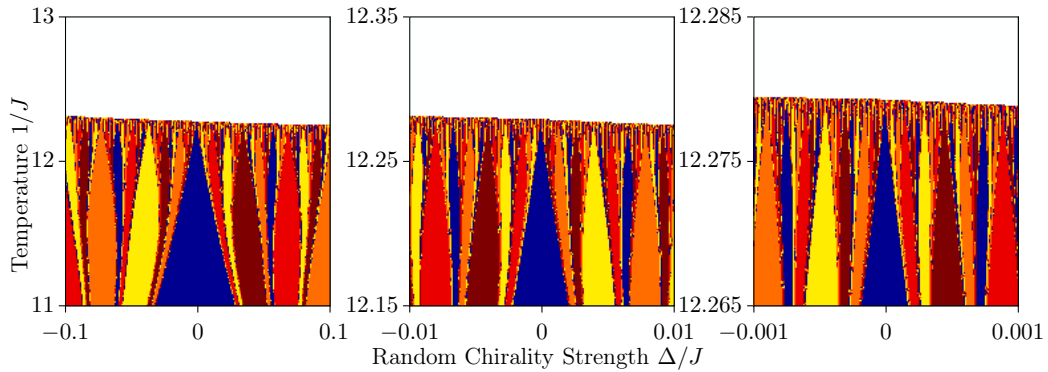
Figure 6.4: The phase diagram cross section in the upper left of Fig. 6.2, with a calculated 10-fold and 100-fold zoom. The devil's staircase structure appears at each zoom level.

actions from the right-hand side of Eq. (6.3), $\{V_{ij}(\delta), V_{ij}(2\delta), V_{ij}(3\delta), V_{ij}(4\delta)\}$, becomes asymptotically dominant. However, in each of the separate phases, it takes a characteristic number n of renormalization-group transformations, namely a length scale of 3^n, to reach the dominance of one chiral interaction. This distinct number of iterations, namely scale changes, determines, by tracing back to the periodic sequence in the original lattice, the pitch of the chiral phase in the original unrenormalized system. Thus, the chiral phases in the original unrenormalized system, with distinct chiral pitches, are distinct phases. After the dominance of one chiral interaction, the renormalization-group trajectory follows the periodic sequence $V_{ij}(\delta) \to V_{ij}(3\delta) \to V_{ij}(4\delta) \to V_{ij}(2\delta) \to V_{ij}(\delta)$ resulting from matching $q = 5$ and $b = 3$.

Our calculation is exact for the hierarchical lattice pictured in Fig. 6.1(b); therefore the phase diagrams in Figs. 6.2 and 6.3 are exactly applicable. However, our calculation is approximate for the cubic lattice, as pictured in Fig. 6.1(a). Thus, one could speculate that in the cubic lattice, the multitude of chiral phases would appear as a single chiral phase with a continuously varying pitch: The continuously varying pitch is shown in the two-dimensional ANNNI model by Monte Carlo simulations, which was also mentioned in Section 2.2.3, and classified as a 'sinusoidal' phase [25] above a certain temperature. The $d = 3$ ANNNI model also exhibits, from mean-field calculations, a devil's staircase structure made up of commensurate and incommensurate orders [158]. Figure 6.5 shows all the chiral phases in our calculation merged into a single phase. It is seen that a quite unusual phase diagram still appears, with the interlacing of the ferromagnetic phase with the chiral phase, throughout the bulk of the phase region.

The renormalization-group trajectories starting in the chiral spin-glass phase, unlike those in the ferromagnetic or chiral phases, do not have the asymptotic behavior where at any scale a single potential $V(\theta)$ is dominant. These trajectories of the spin-glass phase asymptotically go to a strong-coupling fixed probability distribution $P(\boldsymbol{V}_{ij})$ which assigns
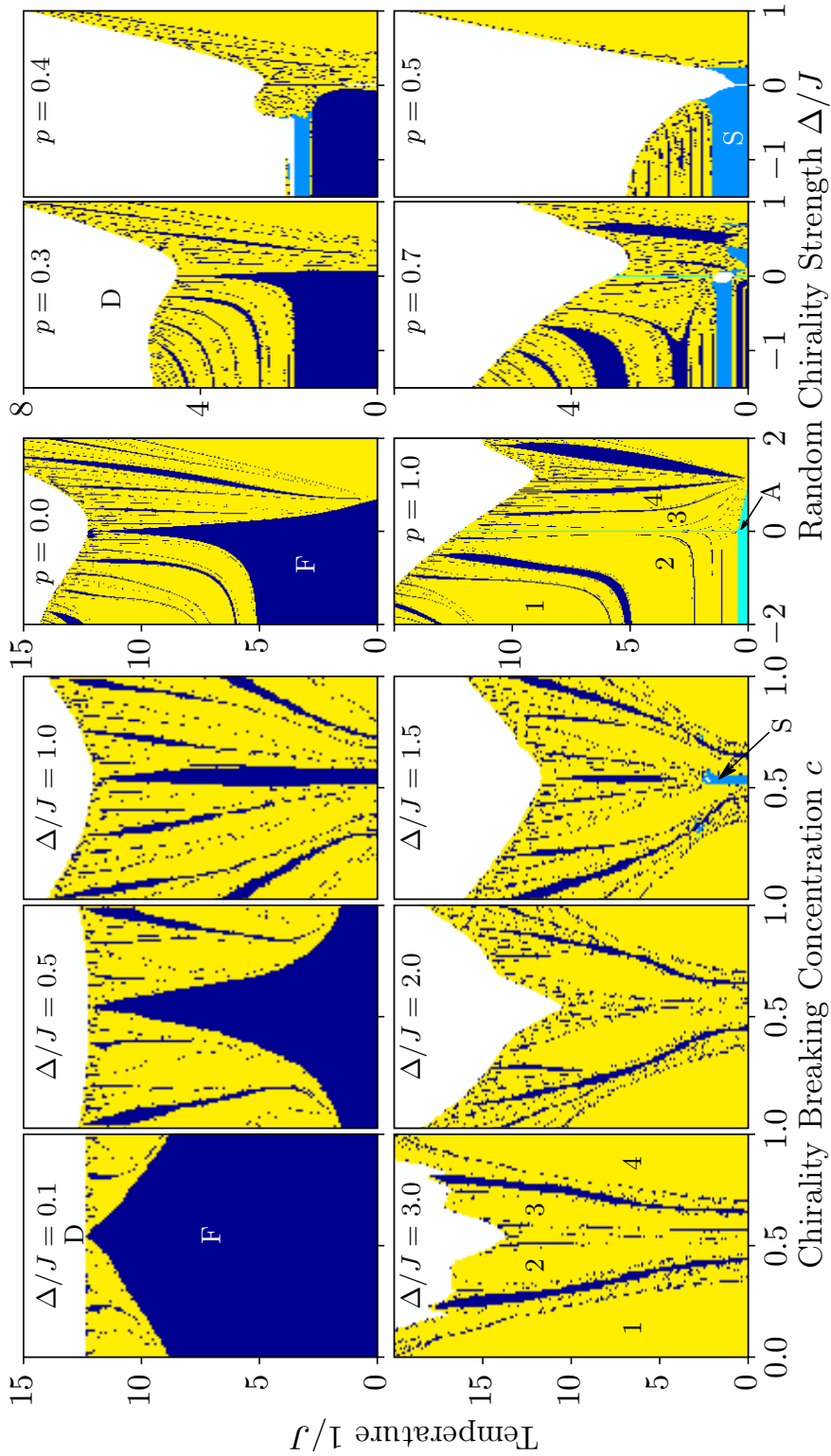
Figure 6.5: Our calculation is exact for the hierarchical lattice pictured in Fig. 6.1(b); therefore the phase diagrams in Figs. 6.2 and 6.3 are exactly applicable. However, our calculation is approximate for the cubic lattice, as pictured in Fig. 6.1(a). Thus, it could be speculated that in the cubic lattice, the multitude of chiral phases would appear as a single chiral phase with a continuously varying pitch: This figure shows all the chiral phases merged into a single phase. It is seen that a quite unusual phase diagram still appears, with the interlacing of the ferromagnetic phase with the chiral phase, throughout the bulk of the phase region. The left side of this figure is derived from the left portion of Fig. 6.2; the right side is derived from the top portion of Fig. 6.3
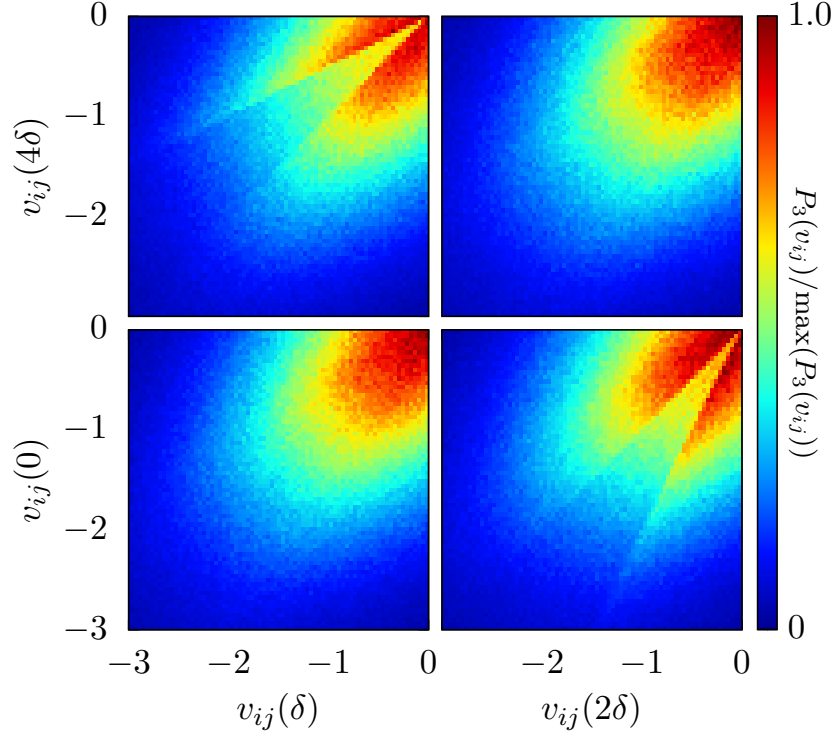
Figure 6.6: Asymptotic fixed distribution of the spin-glass phase. The part of the fixed distribution, $P_3(\boldsymbol{V}_{ij})$ for the interactions $\boldsymbol{V}_{ij}$ in which $V_{ij}(3\delta)$ is maximum and therefore 0 (and the other four interactions are negative) is shown in this figure, with $v_{ij}(\sigma\delta) = V_{ij}(\sigma\delta)/\langle|V_{ij}(\sigma\delta)|\rangle$. The projections of $P_3(\boldsymbol{V}_{ij})$ onto two of its four arguments are shown in each panel of this figure. The other four $P_\sigma(\boldsymbol{V}_{ij})$ have the same fixed distribution. Thus, chirality is broken locally but not globally.

nonzero probabilities to a distribution of $\boldsymbol{V}_{ij}$ values, with no single $V_{ij}(\theta)$ being dominant. Projections of this distribution (a function of five variables) are shown in Fig. 6.6. This situation is a direct generalization of the asymptotic trajectories of the $\pm J$ Ising spin-glass phase, where a fixed probability distribution over positive and negative values of the interaction J is obtained, with no single value of J being dominant [152].

Since, at each locality, the largest interaction in $\{V_{ij}(0), V_{ij}(\delta), V_{ij}(2\delta), V_{ij}(3\delta), V_{ij}(4\delta)\}$ is set to zero and the four other interactions are thus made negative, by subtracting the same constant from all five interactions without affecting the physics, the quenched probability distribution $P(\boldsymbol{V}_{ij})$, a function of five variables, is actually composed of five functions $P_\sigma(\boldsymbol{V}_{ij})$ of four variables, each such function corresponding to one of the interactions being zero and the other four, arguments of the function, being negative. Figure 6.6 shows one of the latter functions: The part of the fixed distribution, $P_3(\boldsymbol{V}_{ij})$, for the interactions $\boldsymbol{V}_{ij}$ in which $V_{ij}(3\delta)$ is maximum and therefore 0 (and the other four interactions are negative) is shown in this figure. The projections of $P_3(\boldsymbol{V}_{ij})$ onto two of its four arguments are shown in each panel of this figure. The other four $P_\sigma(\boldsymbol{V}_{ij})$ have the same fixed distribution. Thus, chirality is broken locally, but not globally.

56
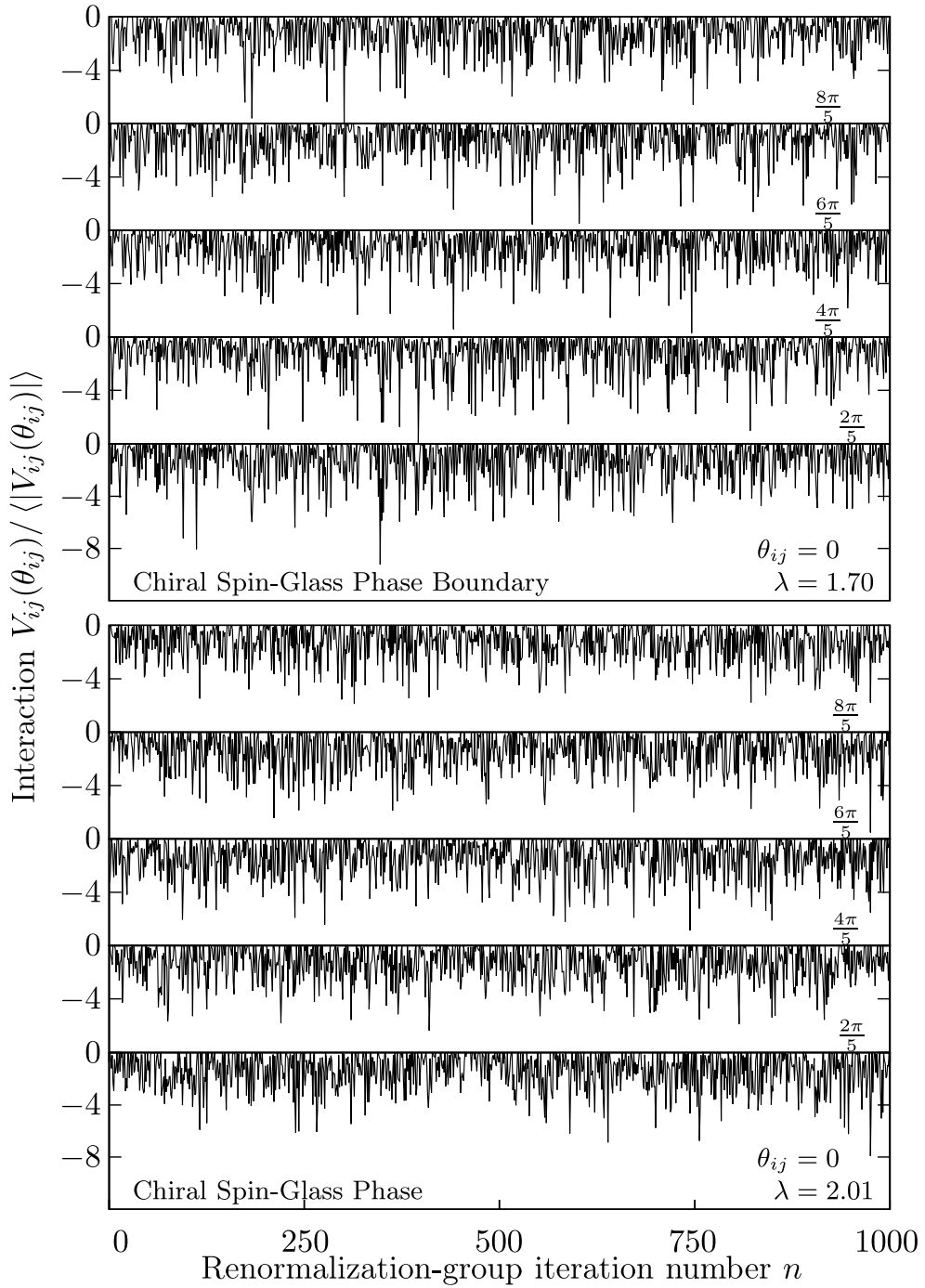
Figure 6.7: Chaotic renormalization-group trajectories of the spin-glass phase (bottom) and of the phase boundary between the spin-glass and disordered phases (top). The five interactions $V_{ij}(0), V_{ij}(\delta), V_{ij}(2\delta), V_{ij}(3\delta), V_{ij}(4\delta)$ at a given location $\langle ij \rangle$, under consecutive renormalization-group transformations, are shown. The $\theta_{ij} = \sigma\delta$ angular value of each interaction $V_{ij}(\theta_{ij})$ is indicated in the figure panels. Bottom panel: Inside the spin-glass phase. The corresponding Lyapunov exponent is $\lambda = 2.01$ and the average interaction diverges as $\langle |V| \rangle \sim b^{y_R n}$, where n is the number of renormalization-group iterations and $y_R = 0.26$ is the runaway exponent. Top panel: At the phase boundary between the spin-glass and disordered phases. The corresponding Lyapunov exponent is $\lambda = 1.70$ and the average nonzero interaction remains fixed at $\langle V \rangle = -0.99$. As indicated by the Lyapunov exponents, chaos is stronger inside the spin-glass phase than at its phase boundary.

Another distinctive mechanics, that of chaos under scale change [50–52] or, equivalently, under spatial translation [32], occurs within the spin-glass phase and differently at the spin-glass phase boundary [32], in systems with competing ferromagnetic and antiferromagnetic interactions [32, 50–79, 159] and with competing left- and right-chiral interactions, introduced in Chpt. 5. The physical hierarchical lattice that we solve here is an infinite system, where 1000 quintuplets $\{V_{ij}(0), V_{ij}(\delta), V_{ij}(2\delta), V_{ij}(3\delta), V_{ij}(4\delta)\})$ are randomly distributed over the lattice bond positions. Thus, as we can fix our attention to one lattice position and monitor how the quintuplet at that position evolves under renormalization-group transformation, as it merges with its neighbors through bond-moving [Eq. (6.4)] and decimation [Eq. (6.5)], and thereby calculate the Lyapunov exponent [32, 53], which when positive is the measure of the strength of chaos.

Figure 6.7 gives the asymptotic chaotic renormalization-group trajectories of the spin-glass phase and, distinctly, of the phase boundary between the spin-glass and disordered phases. The chaotic trajectories found here are similar to those found in traditional (Ising) spin-glasses [32, 53], with of course different Lyapunov exponents seen below. The five interactions $V_{ij}(0), V_{ij}(\delta), V_{ij}(2\delta), V_{ij}(3\delta), V_{ij}(4\delta)$ at a given location $\langle ij \rangle$, under consecutive renormalization-group transformations, are shown in Fig. 6.7. As noted, chaos is measured by the Lyapunov exponent [32, 53, 71, 80, 81], which we here generalize, by the matrix form, to our multiinteraction case:

$$\lambda = \lim_{n \to \infty} \frac{1}{n} \ln \left| \mathcal{E} \left(\prod_{k=0}^{n-1} \frac{d\boldsymbol{v}_{k+1}}{d\boldsymbol{v}_k} \right) \right|, \tag{6.7}$$

where the function $\mathcal{E}(\boldsymbol{M})$ gives the largest eigenvalue of its matrix argument $\boldsymbol{M}$ and the vector $\boldsymbol{v}_k$ is

$$\boldsymbol{v}_k = \{v_{ij}(0), v_{ij}(\delta), v_{ij}(2\delta), v_{ij}(3\delta), v_{ij}(4\delta)\}, \tag{6.8}$$

with $v_{ij}(\sigma\delta) = V_{ij}(\sigma\delta) / \langle |V_{ij}(\sigma\delta)| \rangle$, at step k of the renormalization-group trajectory. The product in Eq. (6.7) is to be taken within the asymptotic chaotic band, which is renormalization-group stable of unstable for the spin-glass phase or its boundary, respectively. Thus, we throw out the first 100 renormalization-group iterations to eliminate the transient points outside of, but leading to, the chaotic band. Subsequently, typically using 1000 renormalization-group iterations in the product in Eq. (6.7) assures the convergence of the Lyapunov exponent value λ, which is thus accurate to the number of significant figures given. Spin-glass chaos occurs for $\lambda > 0$ [71] and as chaos is stronger, λ is more positive, as seen, for example, in the progressions in Figs. 6 and 7 of Ref. [53]. In the spin-glass phase of the currently studied system, the Lyapunov exponent is $\lambda = 2.01$ and the

average interaction diverges as $\langle |V| \rangle \sim b^{y_R n}$, where n is the number of renormalization-group iterations and $y_R = 0.26$ is the runaway exponent. At the phase boundary between the spin-glass and disordered phases, the Lyapunov exponent is $\lambda = 1.70$ and the average nonzero interaction remains fixed at $\langle V \rangle = -0.99$. As indicated by the Lyapunov exponents, chaos is stronger inside the spin-glass phase than at its phase boundary.

6.6. Conclusion

It is thus seen that chirality and chiral quenched randomness provides, in a simple model, remarkably rich phase transition phenomena. These include a multitude of chiral phases, a continuum of widely varying devil's staircases, shallow and deep reentrances of the disordered phase surrounded by regular and temperature-inverted devil's staircases, a critical phase, and a chiral spin-glass phase with chaotic rescaling behavior inside and differently at its boundary. The widely varying continuum of devil's staircase phase diagrams are best seen in video form, four of which are accessible as Supplemental Material [120]. Finally, the study of an even number of q states, which do not have a built-in entropy as mentioned above, should yield equally rich but qualitatively different phase diagrams.

Chapter 7

PHASE TRANSITIONS BETWEEN DIFFERENT SPIN-GLASS PHASES AND MANY CHAOSES IN QUENCHED RANDOM CHIRAL SYSTEMS

7.1.   Introduction

Spin-glass phases, created by competing frustrated random ferromagnetic and anti-ferromagnetic interactions, have been known [17] to incorporate a plethora of interesting complex phenomena, not least being the natural generation chaos [50–52]. Recently, it has been shown [116, 160] that competing left- and right-chiral interactions also create spin-glass phases, even in the absence of competing ferromagnetic and antiferromagnetic interactions. First shown [116] with chiral Potts models [26–30], with the inclusion of quenched randomness, chiral spin glasses were recently extended [160] to clock models with an odd number of states ($q = 5$), resulting in a literally moviesque sequence of phase diagrams, including regular and inverted devil's staircases, a chiral spin-glass phase, and algebraic order.

The chiral clock model work was purposefully initiated [160] with odd number of states q, in order to deal with the complexity of the global phase diagram, since it is known that the odd q models do not show [33] the traditional ferromagnetic-antiferromagnetic spin-glass phase. The current study, on the other hand, is on the random chiral clock model with an even number of states ($q = 4$). A double spin-glass model is constructed, including competing quenched random left-right chiral and ferromagnetic-antiferromagnetic interactions, and solved in three dimensions by renormalization-group theory.

The extremely rich phase diagram includes, to our knowledge for the first time, more than one (four) spin-glass phases on the same phase diagram and three separate spin-

glass-to-spin-glass phase transitions. These constitute phase transitions between chaoses. We determine the chaotic behaviors of the spin-glass phases, of the phase transitions between the spin-glass phases, of the phase transitions between the spin-glass phases and the ferromagnetic, antiferromagnetic, quadrupolar, and disordered phases.

7.2.   Renormalization-Group Method:
Migdal-Kadanoff Approximation and
Exact Hierarchical Lattice Solution

Our method has been previously described in Chpt. 6 and used on a qualitatively different model, with qualitatively different results. Thus, we solve the chiral clock double spin-glass model with $q = 4$ states by renormalization-group theory, in $d = 3$ spatial dimensions, with length rescaling factor $b = 3$. We use $b = 3$, as in previous position-space renormalization-group calculations of spin-glass systems, because it treats ferromagnetism and antiferromagnetism on equal footing. Once again, our solution is, simultaneously, the Migdal-Kadanoff approximation [20, 21] for the cubic lattice and the exact solution [44–48] for the $d = 3$ hierarchical lattice based on the repeated self-imbedding of leftmost graph of Fig. 6.1(b). Figure 6.1(a) shows the Migdal-Kadanoff approximate renormalization-group transformation for the cubic lattice, composed of the bond-moving followed by decimation steps. Figure 6.1(a) shows the exact renormalization-group transformation for the matching hierarchical lattice. The two procedures yield identical recursion relations. Exact calculations on hierarchical lattices are also currently widely used on a variety of statistical mechanics [122–125, 127, 129, 131, 133–137] and finance [161] problems.

Under the renormalization-group transformation described below, the Hamiltonian of Eq. (6.1) maps onto the more general form

$$-\beta\mathcal{H} = \sum_{\langle ij \rangle} V_{ij}(\theta_{ij}),$$ (7.1)

where $\theta_{ij} = \theta_i - \theta_j$ can take q different values, so that for each pair $< ij >$ of nearest-neighbor sites, there are q = 4 different interaction constants

$$\{V_{ij}(\theta_{ij})\} = \{V_{ij}(0), V_{ij}(\pi/2), V_{ij}(\pi), V_{ij}(3\pi/2)\} \equiv \boldsymbol{V}_{ij},$$ (7.2)

which are in general different at each locality (quenched randomness). The largest element of $\{V_{ij}(\theta_{ij})\}$ at each locality $\langle ij \rangle$ is set to zero, by subtracting the same constant

G from all q interaction constants, with no effect on the physics; thus, the $q - 1$ other interaction constants are negative.

The local renormalization-group transformation is achieved by the sequence, shown in Fig. 6.1, of bond movings

$$\widetilde{V}_{ij}(\theta_{ij}) - \widetilde{G} = \sum_{k=1}^{b^{d-1}} V_{ij}^{(k)}(\theta_{ij}), \tag{7.3}$$

and decimations

$$e^{V'_{14}(\theta_{14}) - G} = \sum_{\theta_2, \theta_3} e^{\widetilde{V}_{12}(\theta_{12}) + \widetilde{V}_{23}(\theta_{23}) + \widetilde{V}_{34}(\theta_{34})}, \tag{7.4}$$

where $\widetilde{G}$ and G are the subtractive constants mentioned above, and prime marks the interaction of the renormalized system.

The starting double-bimodal quenched probability distribution of the interactions, characterized by p and c as described above, is not conserved under rescaling. The renormalized quenched probability distribution of the interactions is obtained by the convolution [49]

$$P'(\boldsymbol{V}'_{i'j'}) = \int \left\{ \prod_{ij}^{i'j'} d\boldsymbol{V}_{ij} P(\boldsymbol{V}_{ij}) \right\} \delta(\boldsymbol{V}'_{i'j'} - \boldsymbol{R}(\{\boldsymbol{V}_{ij}\})), \tag{7.5}$$

where $\boldsymbol{V}_{ij} \equiv \{V_{ij}(\theta_{ij})\}$ as in Eq. (7.2), $\boldsymbol{R}(\{\boldsymbol{V}_{ij}\})$ represents the bond moving and bond decimation given in Eqs. (7.3) and (7.4), and primes refer to the renormalized system. Similar previous studies, on other spin-glass systems, are in Refs. [32, 33, 53, 95–97, 99–101, 105]. For numerical practicality the bond moving and decimation of Eqs. (7.3) and (7.4) are achieved by a sequential pairwise combination of interactions, each pairwise combination leading to an intermediate probability distribution resulting from a pairwise convolution as in Eq. (7.5)

We effect this procedure numerically, first starting with the initial double delta distribution of Eq. (6.1) giving 4 possible interactions quenched randomly distributed throughout the system, and generating 1000 interactions that embody the quenched probability distribution resulting from the pairwise combination. Each of the generated 1000 interactions is described by $q = 4$ interaction constants, as explained above [Eq. (7.2)]. At each subsequent pairwise convolution as in Eq. (7.5), 1000 randomly chosen pairs, representing quenched random neighbors in the lattice, are matched by (7.3) or (7.4), and a new set of 1000 interactions is produced. Our calculation simply consists in following the recursion relations, Eqs. (7.3)–(7.5) to the various fixed points and thereby mapping
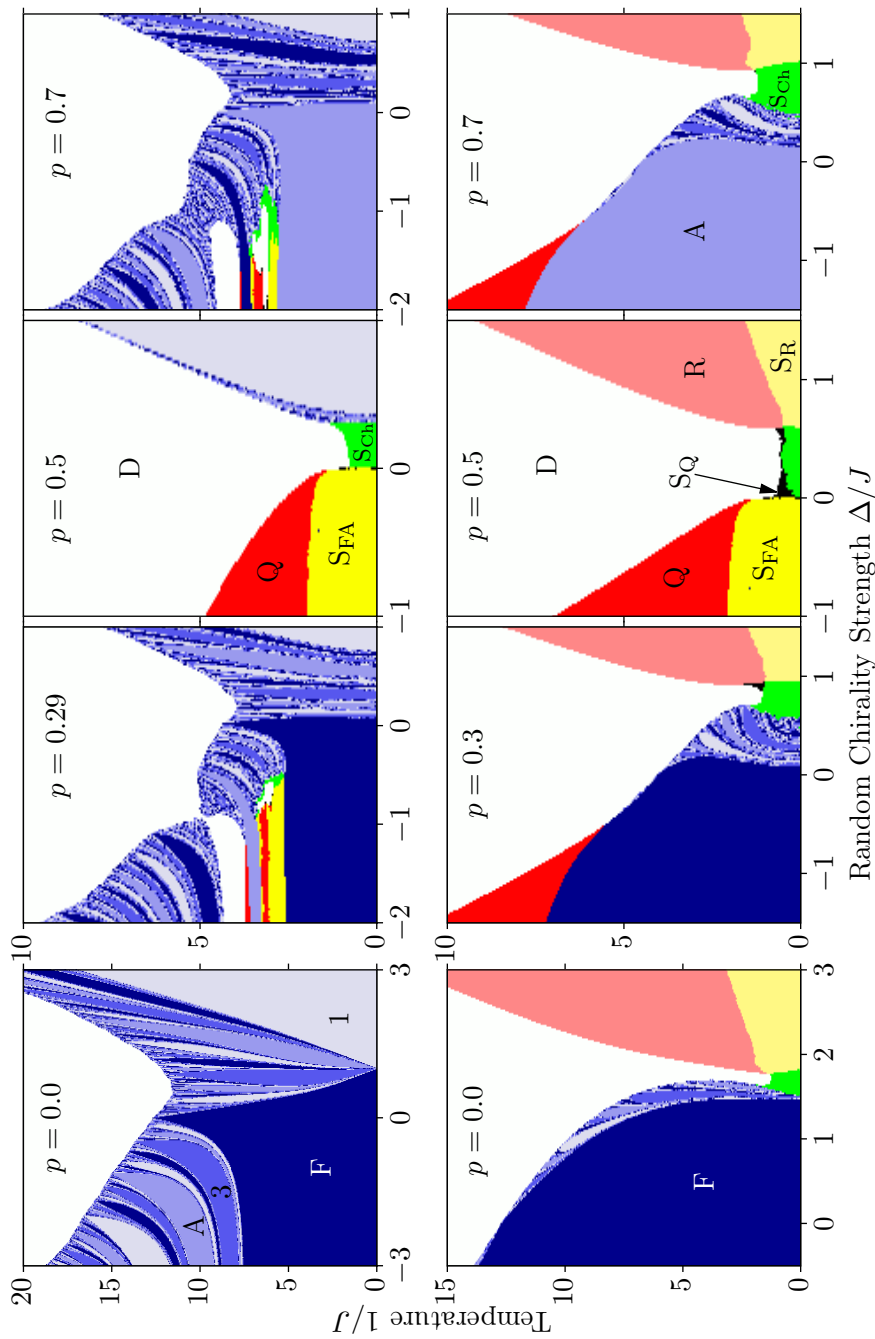
Figure 7.1: A calculated sequence of phase diagrams for the left chiral ($c = 0$), on the upper side, and quenched random left and right chiral ($c = 0.5$), on the lower side, systems with, in both cases, quenched random ferromagnetic and antiferromagnetic interactions. The horizontal axis is the random chirality strength Δ/J. The consecutive phase diagrams are for different concentrations p of antiferromagnetic interactions. The system exhibits a ferromagnetic phase F, an antiferromagnetic phase A, a multitude of different chiral phases, a quadrupolar phases Q, a "one-step" phase R, and four differently ordered spin-glass phases: the chiral spin glass S_{CH}, the usual ferromagnetic-antiferromagnetic spin glass S_{FA}, the quadrupolar spin glass S_Q, and S_R. The phase diagrams obtained from p and $1 - p$ are symmetric, since the system has an even number of spin directions. On some of the chiral phases, the $\pi/2$ multiplicity of the asymptotically dominant interaction is indicated. The ferromagnetic and chiral phases accumulate as different devil's staircases at their boundary with the disordered (D) phase.

63
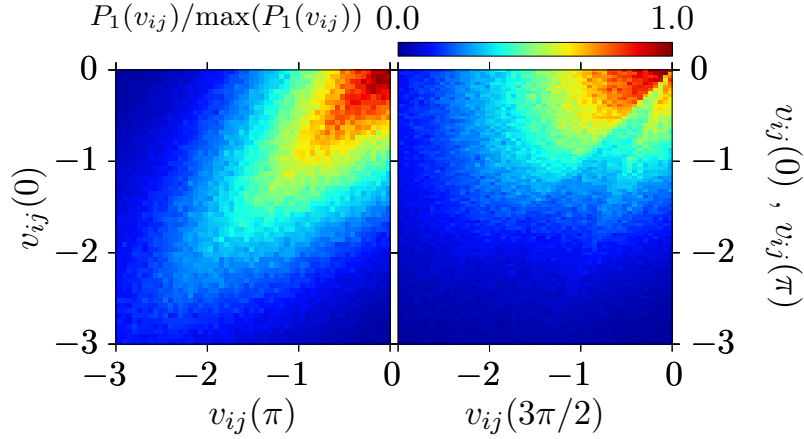
Figure 7.2: Asymptotic fixed distribution of the chiral spin-glass phase S_{Ch}. The part of the fixed distribution $P_1(\mathbf{V}_{ij})$, for the interactions $\mathbf{V}_{ij}$ in which $V_{ij}(\pi/2)$ is maximum and therefore 0 (and the other three interactions are negative) is shown in this figure, with $v_{ij}(\theta) = V_{ij}(\theta)/\langle|V_{ij}(\theta)|\rangle$. The projections of $P_1(\mathbf{V}_{ij})$ onto two of its three arguments are shown in each panel of this figure. The other three $P_\sigma(\mathbf{V}_{ij})$ have the same fixed distribution. Thus chirality is broken locally but not globally, just as, in the long-time studied ferromagnetic-antiferromagnetic spin glasses, spin-direction symmetry breaking is local but not global (i.e., the local magnetization is non-zero, the global magnetization is zero).

the initial conditions that are the basins of attraction of the various fixed points. This map is the phase diagram: The different thermodynamic phases of the system are identified by the different asymptotic renormalization-group flows of the quenched probability distribution $P(\boldsymbol{V}_{ij})$. Two renormalization-group trajectories starting at each side of a phase boundary point diverge from each other, flowing towards the phase sinks (completely stable fixed points) of their respective phases. Thus, the phase boundary point between two phases is readily obtained to the accuracy of the figures. We are therefore able to calculate the global phase diagram of the (importantly even) $q = 4$ chiral clock double spin-glass model.

7.3. Global Phase Diagram: Multiple Spin-Glass Phases

The global phase diagram of the $q = 4$ state chiral clock double spin-glass model in $d = 3$ spatial dimensions, in temperature J^{-1}, antiferromagnetic bond concentration p, random chirality strength Δ/J, and right-chirality concentration c, is a four-dimensional object, so that only the cross-sections of the global phase diagram are exhibited.

Figure 7.1 shows a calculated sequence of phase diagram cross sections for the left-chiral ($c = 0$), on the upper side, and quenched random left- and right-chiral ($c = 0.5$), on the lower side, systems with in both cases quenched random ferromagnetic and antiferromagnetic interactions. The horizontal axis is the random chirality strength Δ/J (See Eq. (6.1)). The consecutive phase diagrams are for different concentrations p of an-
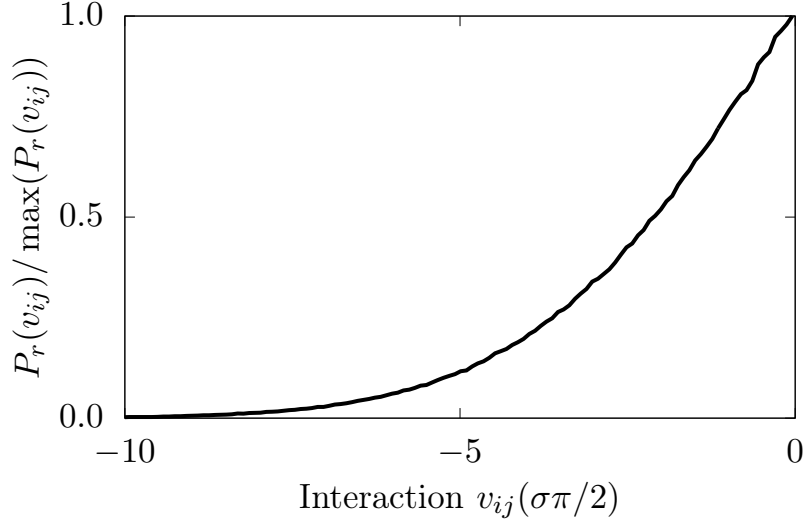
Figure 7.3: Asymptotic fixed distributions of 3 different spin-glass phases, with $v_{ij}(\theta) = V_{ij}(\theta)/\langle|V_{ij}(\theta)|\rangle$. For the ferromagnetic-antiferromagnetic spin-glass S$_{FA}$ phase, $r = 0, \sigma = 2$ and $r = 2, \sigma = 0$. The other two angles do not occur. For the quadrupolar spin-glass S$_Q$ phase, $r = 0, \sigma = 1$ and $r = 1, \sigma = 0$, with $V_{ij}(0) = V_{ij}(\pi)$ and $V_{ij}(\pi/2) = V_{ij}(3\pi/2)$. For the spin-glass S$_R$ phase, $r = 1, \sigma = 3$ and $r = 3, \sigma = 1$. The other two angles do not occur. The $v_{ij}(0) = v_{ij}(\pi)$ curve obtained from the left panel of Fig. 3 also matches the curve here.

tiferromagnetic interactions. The system exhibits a disordered phase (D), a ferromagnetic phase (F), a conventionally ordered (in contrast to the algebraically ordered for $q = 5$) antiferromagnetic phase (A), a quadrupolar phase (Q), a new "one-step" phase (R), a multitude of different chiral phases, and four different spin-glass phases (S$_{Ch}$, S$_{FA}$, S$_Q$, S$_R$) including spin-glass-to-spin-glass phase transitions. The ferromagnetic and different chiral phases accumulate as conventional and temperature-inverted (abutting to the reentrant [107–111] disordered phase) devil's staircases [23, 119] at their boundary with the disordered (D) phase. This accumulation occurs at all scales of phase diagram space (i.e., at all magnifications of the phase diagram figure).

Unlike the odd q case of $q = 5$, which incorporates built-in entropy [160] even without any quenched randomness, no algebraically ordered phase [117, 118] occurs in this even q case of $q = 4$. The devil's staircases of the chiral phases is again seen. Most interestingly, quadrupolar and "one-step" phases, different spin-glass phases for the first time in the same phase diagram, and spin-glass-to-spin-glass direct phase transitions are seen. The phases and phase boundaries involving spin glassiness are tracked through the calculated Lyapunov exponents of their chaos.

In all ordered phases, the renormalization-group trajectories flow to strong (infinite) coupling. In the ferromagnetic phase, under renormalization-group transformations, the interaction $V_{ij}(0)$ becomes asymptotically dominant. In the antiferromagnetic phase, under renormalization-group transformations, the interaction $V_{ij}(\pi)$ becomes asymptotically

dominant. In the quadrupolar phase Q, the interactions $V_{ij}(0)$ and $V_{ij}(\pi)$ become asymptotically dominant and equal. Thus, there are two such quadrupolar phases, namely along the spin directions $\pm x$ or $\pm y$, with the additional (factorized) trivial degeneracy of $\pm$ spin direction at each site. In the new "one-step phase" R, the interactions $V_{ij}(+\pi/2)$ and $V_{ij}(-\pi/2)$ become asymptotically dominant and equal. Thus, in such a phase, the average local spins can span all spin directions, taking $\pm\pi/2$ steps from one spin to the next in the renormalized systems.

In the chiral phases, in the renormalization-group trajectories, one of the chiral interactions from the right-hand side of Eq. (7.2), $\{V_{ij}(\pi/2), V_{ij}(3\pi/2))\}$, becomes asymptotically dominant. However, in each of the separate chiral phases, it takes a characteristic number n of renormalization-group transformations, namely a length scale of 3^n, to reach the dominance of one chiral interaction. This distinct number of iterations, namely scale changes, determines, by tracing back to the periodic sequence in the original lattice, the pitch of the chiral phase in the original unrenormalized system. Thus, the chiral phases in the original unrenormalized system, with distinct chiral pitches, are distinct phases. After the dominance of one chiral interaction, the renormalization-group trajectory follows the periodic sequence $V_{ij}(\pi/2) \to V_{ij}(3\pi/2) \to V_{ij}(\pi/2)$ resulting from matching $q = 4$ and $b = 3$.

The renormalization-group trajectories starting in the spin-glass phases, unlike those in the ferromagnetic, antiferromagnetic, quadrupolar, "one-step", and chiral phases, do not have the asymptotic behavior where at any scale one potential $V(\theta)$ is dominant. These trajectories of the spin-glass phases asymptotically go to a strong-coupling fixed probability distribution $P(\boldsymbol{V}_{ij})$ which assigns non-zero probabilities to a distribution of $\boldsymbol{V}_{ij}$ values, with no single $V_{ij}(\theta)$ being dominant. These distributions are shown in Figs. 3 and 4. Different asymptotic fixed probability distributions indicate different spin-glass phases, for the first time in the same phase diagram.

Since, at each locality, the largest interaction in $\{V_{ij}(0), V_{ij}(\pi/2), V_{ij}(\pi), V_{ij}(3\pi/2)\}$ is set to zero and the three other interactions are thus made negative, by subtracting the same constant from all four interactions without affecting the physics, the quenched probability distribution $P(\boldsymbol{V}_{ij})$, a function of four variables, is actually composed of four functions $P_\sigma(\boldsymbol{V}_{ij})$ of three variables, each such function corresponding to one of the interactions being zero and the other three, arguments of the function, being negative. Figs. 3 and 4 show the latter functions.

In Fig. 7.2 for the spin-glass phase S_{Ch}, the part of the fixed distribution, $P_1(\boldsymbol{V}_{ij})$, for the interactions $\boldsymbol{V}_{ij}$ in which $V_{ij}(\pi/2)$ is maximum and therefore 0 (and the other three interactions are negative) is shown. The projections of $P_1(\boldsymbol{V}_{ij})$ onto two of its

three arguments are shown in each panel of Fig. 7.2. The other three $P_\sigma(\boldsymbol{V}_{ij})$ have the same fixed distribution. Thus, chirality is broken locally, but not globally, just as, in the long-time studied ferromagnetic-antiferromagnetic spin glasses, spin-direction symmetry breaking is local but not global (i.e., the local magnetization is non-zero, the global magnetization is zero). The asymptotic fixed distribution of the phase S_{Ch}, given in Fig. 7.2, assigns non-zero probabilities to a continuum of values for all four interactions $\{V_{ij}(0), V_{ij}(\pi/2), V_{ij}(\pi), V_{ij}(3\pi/2)\}$. The phase S_{Ch} is therefore a chiral spin-glass phase. The similar chiral spin-glass phase has been seen previously, as the sole spin-glass phase, for the odd $q = 5$.[160]. The chiral spin-glass phase occurs even when there is no competing ferromagnetic-antiferromagnetic interactions.[116, 160]

As seen in Fig. 7.3, in the asymptotic fixed distribution of the spin-glass phase S_{FA}, non-zero probabilities are assigned to a continuum of values of $\{V_{ij}(0), V_{ij}(\pi)\}$. Fig. 4 shows the fixed distribution values $P_0(V_{ij}(\pi))$ for $V_{ij}(0)$ maximum and therefore set to zero. Completing the asymptotic fixed distribution of S_{FA} is an identical function $P_2(V_{ij}(0))$ for $V_{ij}(\pi)$ maximum and therefore set to zero. At this fixed distribution, the values of $V_{ij}(\pi/2)$ and $V_{ij}(3\pi/2)$ diverge to negative infinity, so that these angles do not occur. Thus, S_{FA} is the long-studied [17] spin-glass phase of competing ferromagnetic and antiferromagnetic interactions.

Fig. 7.3 also shows the asymptotic fixed distribution of the spin-glass phase S_R, with the functions $P_1(V_{ij}(3\pi/2))$ for $V_{ij}(\pi/2)$ maximum (and therefore set to zero) and $P_3(V_{ij}(\pi/2))$ for $V_{ij}(3\pi/2)$ maximum (and therefore set to zero). Again, the other two angles do not occur at this asymptotic fixed distribution. Furthermore, Fig. 7.3 also shows the asymptotic fixed distribution of the spin-glass phase S_Q, with the functions $P_0(V_{ij}(\pi/2))$ and $P_1(V_{ij}(0))$, with $V_{ij}(0) = V_{ij}(\pi)$ and $V_{ij}(\pi/2) = V_{ij}(3\pi/2)$. Thus, this fixed distribution does not locally distinguish between $\pm$ spin directions and is thus a quadrupolar spin-glass phase.

In fact, the $v_{ij}(0) = v_{ij}(\pi)$ curve obtained from the left panel of Fig. 7.2 also matches the curve here. The three fixed distributions given in Fig. 7.3 exhibit the same numerical curve, but refer to widely different interactions. Thus, they underpin different spin-glass phases.

7.4.   Phase Transitions between Chaos

Another distinctive mechanism, that of chaos under scale change [50–52] or, equivalently, chaos under spatial translation [32], occurs within the spin-glass phase and differently at the spin-glass phase boundary [32], in systems with competing ferromagnetic and
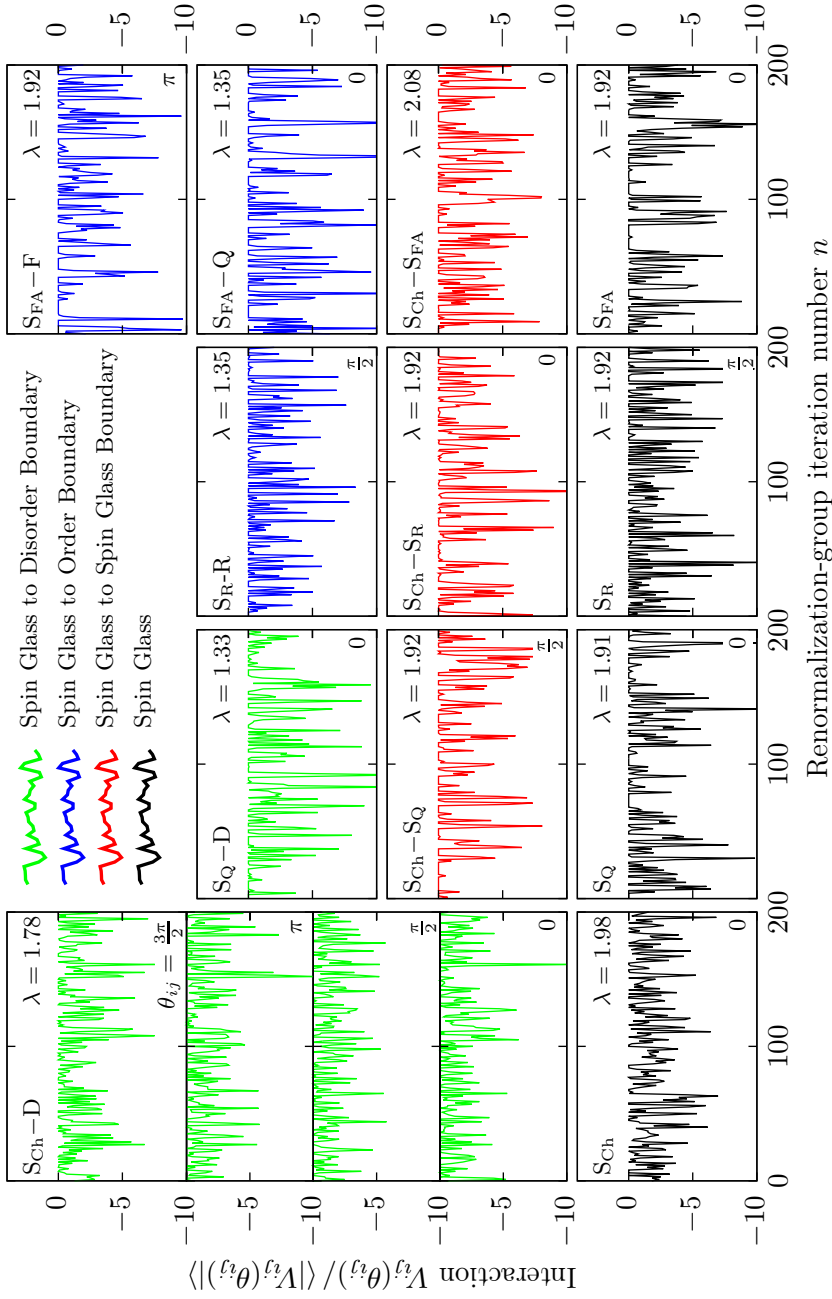
Figure 7.4: Chaotic renormalization-group trajectories of the four different spin-glass phases (black), of the phase boundaries of the spin-glass phases with other spin-glass phases (red), with ordered (blue) and disordered (green) phases. The phase boundary chaoses of each spin-glass phase are given in their corresponding vertically aligned panels. In each case, only one of the four interactions $V_{ij}(0)$, $V_{ij}(\pi/2)$, $V_{ij}(\pi)$, $V_{ij}(3\pi/2)$ at a given location $\langle ij \rangle$, under consecutive renormalization-group transformations, are shown, except, for illustration purposes, all four interactions are shown for $S_{Ch} - D$. The θ_{ij} angular value of each interaction $V_{ij}(\theta_{ij})$ is indicated in the figure panels, as well as the Lyapunov exponent λ calculated from the chaotic sequence under renormalization-group transformations. The Lyapunov exponent is calculated over 1,000 renormalization-group iterations, after throwing out the first 200 iterations. Inside all four spin-glass phases, the average interaction diverges as $< |V| > \sim b^{y_R n}$, where n is the number of renormalization-group iterations and $y_R = 0.25$ is the runaway exponent. At the $S_{Ch}-S_R$, $S_{Ch}-S_Q$, $S_{FA}-A$, $S_{FA}-F$ phase boundaries, $y_R = 0.25$ also. At the $S_{Ch}-S_{FA}$ phase boundary, $y_R = 0.11$ for $V_{ij}(0)$, $V_{ij}(\pi)$ and $y_R = 0.25$ for $V_{ij}(\pi/2)$, $V_{ij}(3\pi/2)$. At the phase boundaries of the spin-glass phases with some non-spin-glass-ordered and disordered phases, the average interaction remains non-divergent, fixed at $< V > = -0.34$ for $S_{FA}-Q$, S_R-R, S_Q-D and $< V > = -1.07$ for $S_{Ch}-D$. As indicated by the Lyapunov exponents, chaos is stronger inside the chiral spin-glass phase.

antiferromagnetic interactions [32, 50–79, 159] and, more recently, with competing left- and right-chiral interactions [116, 160]. The physical hierarchical lattice that we solve here is an infinite system, where 1000 quadruplets $\{V_{ij}(0), V_{ij}(\pi/2), V_{ij}(\pi), V_{ij}(3\pi/2)\}$ are randomly distributed over the lattice bond positions. Thus, as we can fix our attention to one lattice position and monitor how the quadruplet at that position evolves under renormalization-group transformation, as it merges with its neighbors through bond moving [Eq. (7.3)] and decimation [Eq. (7.4)], and thereby calculate the Lyapunov exponent [32, 53], which when positive is the measure of the strength of chaos.

Fig. 7.4 gives the asymptotic chaotic renormalization-group trajectories of the four different spin-glass phases and of the phase boundaries between the spin-glass phases with other spin-glass phases, with the ordered phases and the disordered phase. The chaotic trajectories found here are similar to those found in traditional (Ising) spin-glasses [32, 53], with of course different Lyapunov exponents seen below. The four interactions $V_{ij}(0), V_{ij}(\pi/), V_{ij}(\pi), V_{ij}(3\pi/2)$ at a given location $\langle ij \rangle$, under consecutive renormalization-group transformations, are shown in Fig. 7.4. As noted, chaos is measured by the Lyapunov exponent [32, 53, 71, 80, 81], which we have previously [160] generalized, by the matrix form, to multi-interaction cases:

$$\lambda = \lim_{n \to \infty} \frac{1}{n} \ln \left| \mathcal{E} \left(\prod_{k=0}^{n-1} \frac{d\boldsymbol{v}_{k+1}}{d\boldsymbol{v}_k} \right) \right|, \tag{7.6}$$

where the function $\mathcal{E}(\boldsymbol{M})$ gives the largest eigenvalue of its matrix argument $\boldsymbol{M}$ and the vector $\boldsymbol{v}_k$ is

$$\boldsymbol{v}_k = \{v_{ij}(0), v_{ij}(\pi/2), v_{ij}(\pi), v_{ij}(3\pi/2)\}, \tag{7.7}$$

with $v_{ij}(\theta) = V_{ij}(\theta)/ < |V_{ij}(\theta)| >$, at step k of the renormalization-group trajectory. The product in Eq. (7.6) is to be taken within the asymptotic chaotic band, which is renormalization-group stable or unstable for the spin-glass phase or its boundaries, respectively. Thus, we throw out the first 200 renormalization-group iterations to eliminate the transient points outside of, but leading to the chaotic band. Subsequently, typically using 1,000 renormalization-group iterations in the product in Eq. (7.6) assures the convergence of the Lyapunov exponent value λ.

Spin-glass chaos occurs for $\lambda > 0$ [71] and the more positive λ, the stronger is chaos, as seen for example in the progressions in Figs. 6 and 7 of Ref. [53]. Inside all four spin-glass phases, the average interaction diverges as $< |V| > \sim b^{y_R n}$, where n is the number of renormalization-group iterations and $y_R = 0.25$ is the runaway exponent. In the non-spin-glass-ordered phases, the runaway exponent value is $y_R = d - 1 = 3$ [162].

At the $S_{Ch}-S_R$, $S_{Ch}-S_Q$, $S_{FA}-F$ and its symmetric $S_{FA}-A$ phase boundaries, $y_R = 0.25$ also. At the $S_{Ch}-S_{FA}$ phase boundary, $y_R = 0.11$ for $V_{ij}(0), V_{ij}(\pi)$ and $y_R = 0.25$ for $V_{ij}(\pi/2), V_{ij}(3\pi/2)$. At the phase boundaries of the spin-glass phases with some non-spin-glass-ordered and disordered phases, the average interaction remains non-divergent, fixed at $<V> = -0.34$ for $S_{FA}-Q$, S_R-R, S_Q-D and $<V> = -1.07$ for $S_{Ch}-D$. As indicated by the Lyapunov exponents, chaos is stronger inside the spin-glass phase than at its phase boundaries with non-spin-glass phases.

As expected from the asymptotic fixed distribution analysis given above, the three spin-glass phases S_{FA}, S_Q, S_R and the phase transitions between these phases have the same Lyapunov exponent $\lambda = 1.92$ and therefore the same degree of chaos. The chiral spin-glass S_{Ch} has more chaos ($\lambda = 1.98$) from the other three spin-glass phases. The phase transition between the chiral spin-glass phase S_{Ch} and the other three spin-glass phases is a phase transition between different types of chaos. This phase transition itself of course exhibits chaos, as do all spin-glass phase boundaries.

7.5. Conclusion

The left-right chiral and ferromagnetic-antiferromagnetic double spin-glass clock model, with the crucially even number of states $q = 4$ and in three dimensions $d = 3$, has been solved by renormalization-group theory that is approximate for the cubic lattice and exact for the corresponding hierarchical lattice. We find, for the first time to our knowledge, four different spin-glass phases, including conventional, chiral, and quadrupolar spin-glass phases, and phase transitions between spin-glass phases. The chaoses, in the different spin-glass phases and in the phase transitions of the spin-glass phases with the other spin-glass phases, the non-spin-glass ordered phases, and the disordered phase, are determined and quantified by Lyapunov exponents. It is seen that the chiral spin-glass phase is the most chaotic spin-glass phase. The calculated phase diagram is also otherwise very rich, including regular and temperature-inverted devil's staircases and reentrances.

Chapter 8

CONCLUSION

In this thesis, we have investigated a collection of systems, including the interface roughening-phase transition for the anisotropic Ising models by hard-spin mean-field theory, as well as $q-$state chiral Potts spin-glass models for frustration from competing left and right chiralities, the $q-$state chiral clock double spin-glass models with both competing left-right chiralities, and competing ferromagnetic-antiferromagnetic interactions, using renormalization-group theory.

In Chpt. 3, we start our discussion by considering homogeneous systems. We study the interface roughening phase transition of the $3d$ Ising model using hard-spin mean-field theory, which is an improved mean-field theory that respects the full magnitude of individual local spins, which is important when there are competing local interactions.

In Chpt. 4, the approach is extended to the effects of quenched random pinning centers and missing bonds on the interface of isotropic and uniaxially anisotropic Ising models in $d = 3$. We find that these frozen impurities cause domain boundary roughening that exhibits consecutive thresholding transitions as a function of interaction anisotropy. We also find that, for both missing-bond and pinning-center impurities, for moderately large values of anisotropy, the systems saturate to the "solid-on-solid" limit, exhibiting a single universal curve for the domain boundary width as a function of impurity concentration.

In Chpt. 5, we further examined the quenched random systems, by introducing the chiral spin-glass Potts system. We studied this system by renormalization-group theory with $q = 3$ states in two and three spatial dimensions. The global phase diagrams were calculated in temperature, chirality concentration p, and chirality-breaking concentration c, with determination of phase chaos and phase-boundary chaos. In $d = 3$, the system reveals ferromagnetic, left-chiral, right-chiral, for the first time chiral spin-glass, and disordered phases. The phase boundaries to the ferromagnetic, left- and right-chiral phases show, differently, an unusual fibrous patchwork (microreentrances) of all four (ferromagnetic, left-chiral, right-chiral, chiral spin-glass) ordered phases, especially in the multicritical region. We determined the chaotic behavior of the interactions, under scale change,

both in the chiral spin-glass phase and on the boundary between the chiral spin-glass and disordered phases, showing Lyapunov exponents in relative magnitudes reversed from the usual ferromagnetic-antiferromagnetic spin-glass systems. At low temperatures, the boundaries of the left- and right-chiral phases become thresholded in p and c. In our $d = 2$ calculation, the chiral spin-glass Potts system does not have a spin-glass phase, consistently with the lower-critical dimension of ferromagnetic-antiferromagnetic spin glasses. The left- and right-chirally ordered phases show reentrance in chirality concentration p.

In Chpt. 6 we studied a $q = 5$ state clock spin-glass model in $d = 3$ spatial dimensions, using renormalization-group theory. Our system has both competing ferromagnetic/antiferromagnetic interactions, and competing left/right-chiralities. In $d = 3$, an extremely rich phase diagram contains a ferromagnetic phase, a multitude of chirally ordered phases, a chiral spin-glass phase, and Berker-Kadanoff type critical (algebraically ordered) phase. The global phase diagram exhibits a richly varying continuum of devil's staircases, where the ferromagnetic and chirally ordered phases accumulate at the phase boundary with the disordered phase. The phase diagrams contain shallow and deep reentrances of the disordered phase, surrounded by regular and temperature-inverted devil's staircases. The rich continuum of such phase diagrams were combined into a movie, showing the evolution of phase diagram.

In Chpt. 7, we further examined the initially described q-state chiral clock double spin-glass system to $q = 4$. We find, for the first time to our knowledge, four different spin-glass phases, including conventional, chiral, and quadrupolar spin-glass phases, and phase transitions between spin-glass phases. The chaoses, in the different spin-glass phases and in the phase transitions of the spin-glass phases with the other spin-glass phases, with the non-spin-glass ordered phases, and with the disordered phase, are determined and quantified by Lyapunov exponents. It is seen that the chiral spin-glass phase is the most chaotic spin-glass phase. The calculated phase diagram is also otherwise very rich, including regular and temperature-inverted devil's staircases and reentrances.

Bibliography

[1] J. D. van der Waals, *Over de Continuiteit van den Gas- en Vloeistoftoestand.* PhD thesis, University of Leiden, 1873.

[2] J. C. Maxwell, "On the dynamical evidence of the molecular constitution of bodies," *Nature*, vol. 11, pp. 357–359, 1875.

[3] T. Andrews, "The Bakerian lecture: On the continuity of the gaseous and liquid states of matter," *Philosophical Transactions of the Royal Society of London*, vol. 159, pp. 575–590, 1869.

[4] P. Curie, "Propriétés magnétiques des crops è diverses températures," *Ann. Chim. Phys.*, vol. 5, pp. 289–405, 1895.

[5] P. Weiss, "L'hypothèse du champ moléculaire et la propriété ferromagnétique," *J. Phys. Theor. Appl.*, vol. 6, pp. 661–690, 1907.

[6] H. E. Stanley, *Introduction to Phase Transitions and Critical Phenomena.* International series of monographs on physics, Oxford University Press, 1971.

[7] E. A. Guggenheim, "The principle of corresponding states," *The Journal of Chemical Physics*, vol. 13, no. 7, pp. 253–261, 1945, http://dx.doi.org/10.1063/1.1724033.

[8] L. P. Kadanoff, "Scaling laws for Ising models near t_c," *Physics*, vol. 2, pp. 263–272, Feb 1966.

[9] J. Yeomans, *Statistical Mechanics of Phase Transitions.* Clarendon Press, 1992.

[10] F. Bundy, W. Bassett, M. Weathers, R. Hemley, H. Mao, and A. Goncharov, "The pressure-temperature phase and transformation diagram for carbon; updated through 1994," *Carbon*, vol. 34, no. 2, pp. 141 – 153, 1996.

[11] M. Blume, V. J. Emery, and R. B. Griffiths, "Ising model for the λ transition and phase separation in He^3-He^4 mixtures," *Phys. Rev. A*, vol. 4, pp. 1071–1077, Sep 1971.

[12] F. Y. Wu, "The Potts model," *Rev. Mod. Phys.*, vol. 54, pp. 235–268, Jan 1982.

[13] F. Y. Wu, "Erratum: The Potts model," *Rev. Mod. Phys.*, vol. 55, pp. 315–315, Jan 1983.

[14] L. Onsager, "Crystal statistics. i. a two-dimensional model with an order-disorder transition," *Phys. Rev.*, vol. 65, pp. 117–149, Feb 1944.

[15] S. T. Chui and J. D. Weeks, "Phase transition in the two-dimensional Coulomb gas, and the interfacial roughening transition," *Phys. Rev. B*, vol. 14, pp. 4978–4982, Dec 1976.

[16] R. H. Swendsen, "Monte Carlo studies of the interface roughening transition," *Phys. Rev. B*, vol. 15, pp. 5421–5431, Jun 1977.

[17] H. Nishimori, *Statistical Physics of Spin Glasses and Information Processing: An Introduction*. International series of monographs on physics, Oxford University Press, 2001.

[18] R. R. Netz and A. N. Berker, "Monte Carlo mean-field theory and frustrated systems in two and three dimensions," *Phys. Rev. Lett.*, vol. 66, pp. 377–380, Jan 1991.

[19] R. R. Netz and A. N. Berker, "Hard-spin mean-field theory: Formulation for Ising, xy, and other models," *Journal of Applied Physics*, vol. 70, no. 10, pp. 6074–6076, 1991, http://dx.doi.org/10.1063/1.350050.

[20] A. A. Migdal, "Phase transitions in gauge and spin-lattice systems," *Zh. Eksp. Teor. Fiz.*, vol. 69, p. 1457, 1975. [Sov. Phys. JETP **42**, 743 (1976)].

[21] L. P. Kadanoff, "Notes on Migdal's recursion formulas," *Annals of Physics*, vol. 100, no. 1, pp. 359 – 394, 1976.

[22] P. Bak, "Commensurate phases, incommensurate phases and the devil's staircase," *Reports on Progress in Physics*, vol. 45, no. 6, p. 587, 1982.

[23] P. Bak and R. Bruinsma, "One-dimensional Ising model and the complete devil's staircase," *Phys. Rev. Lett.*, vol. 49, pp. 249–251, Jul 1982.

[24] M. E. Fisher and W. Selke, "Infinitely many commensurate phases in a simple ising model," *Phys. Rev. Lett.*, vol. 44, pp. 1502–1505, Jun 1980.

[25] W. Selke and M. E. Fisher, "Two-dimensional ising models with competing interaction—a monte carlo study," *Zeitschrift für Physik B Condensed Matter*, vol. 40, no. 1, pp. 71–77, 1980.

[26] S. Ostlund, "Incommensurate and commensurate phases in asymmetric clock models," *Phys. Rev. B*, vol. 24, pp. 398–405, Jul 1981.

[27] M. Kardar and A. N. Berker, "Commensurate-incommensurate phase diagrams for overlayers from a helical Potts model," *Phys. Rev. Lett.*, vol. 48, pp. 1552–1555, May 1982.

[28] D. A. Huse and M. E. Fisher, "Domain walls and the melting of commensurate surface phases," *Phys. Rev. Lett.*, vol. 49, pp. 793–796, Sep 1982.

[29] D. A. Huse and M. E. Fisher, "Commensurate melting, domain walls, and dislocations," *Phys. Rev. B*, vol. 29, pp. 239–270, Jan 1984.

[30] R. G. Caflisch, A. Nihat Berker, and M. Kardar, "Reentrant melting of krypton adsorbed on graphite and the helical Potts-lattice-gas model," *Phys. Rev. B*, vol. 31, pp. 4527–4537, Apr 1985.

[31] A. N. Berker, S. Ostlund, and F. A. Putnam, "Renormalization-group treatment of a Potts lattice gas for krypton adsorbed onto graphite," *Phys. Rev. B*, vol. 17, pp. 3650–3665, May 1978.

[32] E. Ilker and A. N. Berker, "High q-state clock spin glasses in three dimensions and the lyapunov exponents of chaotic phases and chaotic phase boundaries," *Phys. Rev. E*, vol. 87, p. 032124, Mar 2013.

[33] E. Ilker and A. N. Berker, "Odd q-state clock spin-glass models in three dimensions, asymmetric phase diagrams, and multiple algebraically ordered phases," *Phys. Rev. E*, vol. 90, p. 062112, Dec 2014.

[34] C. Lupo and F. Ricci-Tersenghi, "Approximating the xy model on a random graph with a q-state clock model," *Phys. Rev. B*, vol. 95, p. 054433, Feb 2017.

[35] J. R. Banavar, M. Cieplak, and A. Maritan, "Monte Carlo mean-field theory," *Phys. Rev. Lett.*, vol. 67, pp. 1807–1807, Sep 1991.

[36] R. R. Netz and A. N. Berker, "Netz and Berker reply," *Phys. Rev. Lett.*, vol. 67, pp. 1808–1808, Sep 1991.

[37] A. N. Berker, A. Kabakçıoğlu, R. R. Netz, and M. C. Yalabık, "Hard-spin mean-field theory," *Turk. J. Phys.*, vol. 18, p. 354, 1994.

[38] A. Kabakçıoğlu, A. Nihat Berker, and M. Cemal Yalabık, "Closed-form solutions and free energy of hard-spin mean-field theory of a fully frustrated system," *Phys. Rev. E*, vol. 49, pp. 2680–2683, Apr 1994.

[39] H. Kaya and A. Nihat Berker, "Multiplicity of ordered phases in frustrated systems obtained from hard-spin mean-field theory," *Phys. Rev. E*, vol. 62, pp. R1469–R1472, Aug 2000.

[40] R. R. Netz, "Symmetry-breaking fields in frustrated Ising systems on square and cubic lattices: Inclusive and exclusive multiphase lines," *Phys. Rev. B*, vol. 46, pp. 1209–1212, Jul 1992.

[41] R. R. Netz, "Spin-enhanced ordering in fully frustrated Ising models," *Phys. Rev. B*, vol. 48, pp. 16113–16115, Dec 1993.

[42] B. Yücesoy and A. N. Berker, "Field-driven hysteresis of the $d = 3$ Ising spin glass: Hard-spin mean-field theory," *Phys. Rev. B*, vol. 76, p. 014417, Jul 2007.

[43] B. McCoy and T. Wu, *The two-dimensional Ising model*. Harvard University Press, 1973.

[44] A. N. Berker and S. Ostlund, "Renormalisation-group calculations of finite systems: order parameter and specific heat for epitaxial ordering," *Journal of Physics C: Solid State Physics*, vol. 12, no. 22, p. 4961, 1979.

[45] R. B. Griffiths and M. Kaufman, "Spin systems on hierarchical lattices. introduction and thermodynamic limit," *Phys. Rev. B*, vol. 26, pp. 5022–5032, Nov 1982.

[46] M. Kaufman and R. B. Griffiths, "Spin systems on hierarchical lattices. II. some examples of soluble models," *Phys. Rev. B*, vol. 30, pp. 244–249, Jul 1984.

[47] S. R. McKay and A. N. Berker, "Magnetic susceptibilities of cluster-hierarchical models," *Phys. Rev. B*, vol. 29, pp. 1315–1320, Feb 1984.

[48] M. Hinczewski and A. Nihat Berker, "Inverted Berezinskii-Kosterlitz-Thouless singularity and high-temperature algebraic order in an Ising model on a scale-free hierarchical-lattice small-world network," *Phys. Rev. E*, vol. 73, p. 066126, Jun 2006.

[49] D. Andelman and A. N. Berker, "Scale-invariant quenched disorder and its stability criterion at random critical points," *Phys. Rev. B*, vol. 29, pp. 2630–2635, Mar 1984.

[50] S. R. McKay, A. N. Berker, and S. Kirkpatrick, "Spin-glass behavior in frustrated Ising models with chaotic renormalization-group trajectories," *Phys. Rev. Lett.*, vol. 48, pp. 767–770, Mar 1982.

[51] S. R. McKay, A. N. Berker, and S. Kirkpatrick, "Amorphously packed, frustrated hierarchical models: Chaotic rescaling and spin-glass behavior," *Journal of Applied Physics*, vol. 53, no. 11, pp. 7974–7976, 1982, http://dx.doi.org/10.1063/1.330246.

[52] A. N. Berker and S. R. McKay, "Hierarchical models and chaotic spin glasses," *Journal of Statistical Physics*, vol. 36, no. 5, pp. 787–793, 1984.

[53] E. Ilker and A. N. Berker, "Overfrustrated and underfrustrated spin glasses in $d = 3$ and 2: Evolution of phase diagrams and chaos including spin-glass order in $d = 2$," *Phys. Rev. E*, vol. 89, p. 042139, Apr 2014.

[54] A. J. Bray and M. A. Moore, "Chaotic nature of the spin-glass phase," *Phys. Rev. Lett.*, vol. 58, pp. 57–60, Jan 1987.

[55] E. J. Hartford and S. R. McKay, "Ising spin-glass critical and multicritical fixed distributions from a renormalization-group calculation with quenched randomness," *Journal of Applied Physics*, vol. 70, no. 10, pp. 6068–6070, 1991, http://dx.doi.org/10.1063/1.350048.

[56] M. Nifle and H. J. Hilhorst, "New critical-point exponent and new scaling laws for short-range Ising spin glasses," *Phys. Rev. Lett.*, vol. 68, pp. 2992–2995, May 1992.

[57] M. Ney-Nifle and H. Hilhorst, "Renormalization theory and chaos exponents in random systems," *Physica A: Statistical Mechanics and its Applications*, vol. 194, no. 1–4, pp. 462 – 470, 1993.

[58] M. Cieplak, M. S. Li, and J. R. Banavar, "Universality and chaos in xy spin glasses," *Phys. Rev. B*, vol. 47, pp. 5022–5026, Mar 1993.

[59] F. Krząkała, "On temperature chaos in Ising and xy spin glasses," *EPL (Europhysics Letters)*, vol. 66, no. 6, p. 847, 2004.

[60] F. Krząkała and J.-P. Bouchaud, "Disorder chaos in spin glasses," *EPL (Europhysics Letters)*, vol. 72, no. 3, p. 472, 2005.

[61] M. Sasaki, K. Hukushima, H. Yoshino, and H. Takayama, "Temperature chaos and bond chaos in Edwards-Anderson Ising spin glasses: Domain-wall free-energy measurements," *Phys. Rev. Lett.*, vol. 95, p. 267203, Dec 2005.

[62] J. Lukic, E. Marinari, O. C. Martin, and S. Sabatini, "Temperature chaos in two-dimensional Ising spin glasses with binary couplings: a further case for universality," *Journal of Statistical Mechanics: Theory and Experiment*, vol. 2006, no. 10, p. L10001, 2006.

[63] P. Le Doussal, "Chaos and residual correlations in pinned disordered systems," *Phys. Rev. Lett.*, vol. 96, p. 235702, Jun 2006.

[64] T. Rizzo and H. Yoshino, "Chaos in glassy systems from a Thouless-Anderson-Palmer perspective," *Phys. Rev. B*, vol. 73, p. 064416, Feb 2006.

[65] H. G. Katzgraber and F. Krząkała, "Temperature and disorder chaos in three-dimensional Ising spin glasses," *Phys. Rev. Lett.*, vol. 98, p. 017201, Jan 2007.

[66] H. Yoshino and T. Rizzo, "Stepwise responses in mesoscopic glassy systems: A mean-field approach," *Phys. Rev. B*, vol. 77, p. 104429, Mar 2008.

[67] J. H. Pixley and A. P. Young, "Large-scale Monte Carlo simulations of the three-dimensional xy spin glass," *Phys. Rev. B*, vol. 78, p. 014419, Jul 2008.

[68] T. Aspelmeier, "Free-energy fluctuations and chaos in the sherrington-kirkpatrick model," *Phys. Rev. Lett.*, vol. 100, p. 117205, Mar 2008.

[69] T. Aspelmeier, "Bond chaos in the sherringtonâĂŞkirkpatrick model," *Journal of Physics A: Mathematical and Theoretical*, vol. 41, no. 20, p. 205005, 2008.

[70] T. Mora and L. Zdeborová, "Random subcubes as a toy model for constraint satisfaction problems," *Journal of Statistical Physics*, vol. 131, no. 6, pp. 1121–1138, 2008.

[71] N. Aral and A. N. Berker, "Chaotic spin correlations in frustrated Ising hierarchical lattices," *Phys. Rev. B*, vol. 79, p. 014434, Jan 2009.

[72] Q.-H. Chen, "Large-scale dynamical simulations of the three-dimensional xy spin glass," *Phys. Rev. B*, vol. 80, p. 144420, Oct 2009.

[73] T. Jörg and F. Krząkała, "The nature of the different zero-temperature phases in discrete two-dimensional spin glasses: entropy, universality, chaos and cascades

in the renormalization group flow," *Journal of Statistical Mechanics: Theory and Experiment*, vol. 2012, no. 01, p. L01001, 2012.

[74] W. de Lima, G. Camelo-Neto, and S. Coutinho, "Strange attractor in the Potts spin glass on hierarchical lattices," *Physics Letters A*, vol. 377, no. 40, pp. 2851 – 2855, 2013.

[75] W. Wang, J. Machta, and H. G. Katzgraber, "Chaos in spin glasses revealed through thermal boundary conditions," *Phys. Rev. B*, vol. 92, p. 094410, Sep 2015.

[76] V. Martin-Mayor and I. Hen, "Unraveling quantum annealers using classical hardness," vol. 5, pp. 15324 EP –, Oct 2015. Article.

[77] Z. Zhu, A. J. Ochoa, S. Schnabel, F. Hamze, and H. G. Katzgraber, "Best-case performance of quantum annealers on native spin-glass benchmarks: How chaos can affect success probabilities," *Phys. Rev. A*, vol. 93, p. 012317, Jan 2016.

[78] W. Wang, J. Machta, and H. G. Katzgraber, "Bond chaos in spin glasses revealed through thermal boundary conditions," *Phys. Rev. B*, vol. 93, p. 224414, Jun 2016.

[79] L. A. Fernandez, E. Marinari, V. Martin-Mayor, G. Parisi, and D. Yllanes, "Temperature chaos is a non-local effect," *Journal of Statistical Mechanics: Theory and Experiment*, vol. 2016, no. 12, p. 123301, 2016.

[80] P. Collet and J. Eckmann, *Iterated Maps on the Interval as Dynamical Systems*. Progress in Mathematical Physics, Birkhäuser Boston, 1980.

[81] R. Hilborn, *Chaos and Nonlinear Dynamics: An Introduction for Scientists and Engineers*. Oxford University Press, 2000.

[82] A. M. Ferrenberg and D. P. Landau, "Critical behavior of the three-dimensional Ising model: A high-resolution Monte Carlo study," *Phys. Rev. B*, vol. 44, pp. 5081–5091, Sep 1991.

[83] S. B. Kim, J. Ma, and M. H. W. Chan, "Phase diagram of $^3-^4$He mixture in aerogel," *Phys. Rev. Lett.*, vol. 71, pp. 2268–2271, Oct 1993.

[84] A. Falicov and A. N. Berker, "Correlated random-chemical-potential model for the phase transitions of helium mixtures in porous media," *Phys. Rev. Lett.*, vol. 74, pp. 426–429, Jan 1995.

[85] T. Çağlar and A. N. Berker, "Interface-roughening phase diagram of the three-dimensional Ising model for all interaction anisotropies from hard-spin mean-field theory," *Phys. Rev. E*, vol. 84, p. 051129, Nov 2011.

[86] E. A. Ames and S. R. McKay, "Calculated field cooled and zero field cooled magnetizations of the three-dimensional Ising spin glass using Monte Carlo hard-spin mean-field theory (abstract)," *Journal of Applied Physics*, vol. 76, no. 10, pp. 6197–6197, 1994, http://dx.doi.org/10.1063/1.358350.

[87] G. B. Akgüç and M. Cemal Yalabık, "Hard-spin mean-field theory of a three-dimensional stacked-triangular-lattice system," *Phys. Rev. E*, vol. 51, pp. 2636–2639, Mar 1995.

[88] J. E. Tesiero and S. R. McKay, "Criticality of the fully frustrated xy model: A study using Monte Carlo hard-spin mean-field theory (abstract)," *Journal of Applied Physics*, vol. 79, no. 8, pp. 6146–6146, 1996, http://aip.scitation.org/doi/pdf/10.1063/1.362052.

[89] J. L. Monroe, "Hard spin mean field theory for an Ising model with pair and three site interactions," *Physics Letters A*, vol. 230, no. 1, pp. 111 – 116, 1997.

[90] A. Pelizzola and M. Pretti, "Properties of some mean-field-like approximations for the triangular Ising antiferromagnet," *Phys. Rev. B*, vol. 60, pp. 10134–10144, Oct 1999.

[91] A. Kabakçıoğlu, "Hard-spin mean-field theory: A systematic derivation and exact correlations in one dimension," *Phys. Rev. E*, vol. 61, pp. 3366–3368, Apr 2000.

[92] O. S. Sarıyer, A. Kabakçıoğlu, and A. N. Berker, "Deep spin-glass hysteresis-area collapse and scaling in the three-dimensional $\pm J$ Ising model," *Phys. Rev. E*, vol. 86, p. 041107, Oct 2012.

[93] R. H. Swendsen, "Roughening transition in the solid-on-solid model," *Phys. Rev. B*, vol. 15, pp. 689–692, Jan 1977.

[94] D. Yeşilleten and A. N. Berker, "Renormalization-group calculation of local magnetizations and correlations: Random-bond, random-field, and spin-glass systems," *Phys. Rev. Lett.*, vol. 78, pp. 1564–1567, Feb 1997.

[95] M. J. P. Gingras and E. S. So/rensen, "Lack of reentrance in randomly frustrated three-dimensional xy ferromagnets," *Phys. Rev. B*, vol. 46, pp. 3441–3451, Aug 1992.

[96] G. Migliorini and A. N. Berker, "Global random-field spin-glass phase diagrams in two and three dimensions," *Phys. Rev. B*, vol. 57, pp. 426–431, Jan 1998.

[97] M. J. P. Gingras and E. S. Sørensen, "Evidence for a genuine ferromagnetic to paramagnetic reentrant phase transition in a Potts spin-glass model," *Phys. Rev. B*, vol. 57, pp. 10264–10267, May 1998.

[98] M. Hinczewski and A. N. Berker, "Multicritical point relations in three dual pairs of hierarchical-lattice Ising spin glasses," *Phys. Rev. B*, vol. 72, p. 144402, Oct 2005.

[99] C. N. Kaplan and A. N. Berker, "Quantum-mechanically induced asymmetry in the phase diagrams of spin-glass systems," *Phys. Rev. Lett.*, vol. 100, p. 027204, Jan 2008.

[100] C. Güven, A. N. Berker, M. Hinczewski, and H. Nishimori, "Reentrant and forward phase diagrams of the anisotropic three-dimensional Ising spin glass," *Phys. Rev. E*, vol. 77, p. 061110, Jun 2008.

[101] M. Ohzeki, H. Nishimori, and A. N. Berker, "Multicritical points for spin-glass models on hierarchical lattices," *Phys. Rev. E*, vol. 77, p. 061116, Jun 2008.

[102] V. O. Özçelik and A. N. Berker, "Blume-Emery-Griffiths spin glass and inverted tricritical points," *Phys. Rev. E*, vol. 78, p. 031104, Sep 2008.

[103] G. Gülpınar and A. N. Berker, "Quenched-vacancy induced spin-glass order," *Phys. Rev. E*, vol. 79, p. 021110, Feb 2009.

[104] C. N. Kaplan, M. Hinczewski, and A. N. Berker, "Infinitely robust order and local order-parameter tulips in apollonian networks with quenched disorder," *Phys. Rev. E*, vol. 79, p. 061120, Jun 2009.

[105] M. Demirtaş, A. Tuncer, and A. N. Berker, "Lower-critical spin-glass dimension from 23 sequenced hierarchical models," *Phys. Rev. E*, vol. 92, p. 022136, Aug 2015.

[106] J. Indekeu and A. Berker, "Molecular tail lengths, dipole pairings, and multiple reentrance mechanisms of liquid crystals," *Physica A: Statistical Mechanics and its Applications*, vol. 140, no. 1–2, pp. 368 – 375, 1986.

[107] J. O. Indekeu, A. N. Berker, C. Chiang, and C. W. Garland, "Reentrant transition enthalpies of liquid crystals: The frustrated spin-gas model and experiments," *Phys. Rev. A*, vol. 35, pp. 1371–1375, Feb 1987.

[108] P. E. Cladis, "New liquid-crystal phase diagram," *Phys. Rev. Lett.*, vol. 35, pp. 48–51, Jul 1975.

[109] F. Hardouin, A. M. Levelut, M. F. Achard, and G. Sigaud, "Polymorphisme des substances mésogènes a molécules polaires. I. physico-chimie et structure," *J. Chim. Phys.*, vol. 80, pp. 53–64, 1983.

[110] R. R. Netz and A. N. Berker, "Smectic-c order, in-plane domains, and nematic reentrance in a microscopic model of liquid crystals," *Phys. Rev. Lett.*, vol. 68, pp. 333–336, Jan 1992.

[111] S. Kumari and S. Singh, "Effect of electric field on reentrance transition in a binary mixture of liquid crystals," *Phase Transitions*, vol. 88, no. 12, pp. 1225–1235, 2015, http://dx.doi.org/10.1080/01411594.2015.1051799.

[112] S. Franz, G. Parisi, and M.A. Virasoro, "Interfaces and louver critical dimension in a spin glass model," *J. Phys. I France*, vol. 4, no. 11, pp. 1657–1667, 1994.

[113] S. Boettcher, "Stiffness of the Edwards-Anderson model in all dimensions," *Phys. Rev. Lett.*, vol. 95, p. 197205, Nov 2005.

[114] C. Amoruso, E. Marinari, O. C. Martin, and A. Pagnani, "Scalings of domain wall energies in two dimensional Ising spin glasses," *Phys. Rev. Lett.*, vol. 91, p. 087201, Aug 2003.

[115] J.-P. Bouchaud, F. Krząkała, and O. C. Martin, "Energy exponents and corrections to scaling in Ising spin glasses," *Phys. Rev. B*, vol. 68, p. 224404, Dec 2003.

[116] T. Çağlar and A. N. Berker, "Chiral Potts spin glass in $d = 2$ and 3 dimensions," *Phys. Rev. E*, vol. 94, p. 032121, Sep 2016.

[117] A. N. Berker and L. P. Kadanoff, "Ground-state entropy and algebraic order at low temperatures," *Journal of Physics A: Mathematical and General*, vol. 13, no. 7, p. L259, 1980.

[118] A. N. Berker and L. P. Kadanoff, "Ground-state entropy and algebraic order at low temperatures," *Journal of Physics A: Mathematical and General*, vol. 13, no. 12, p. 3786, 1980.

[119] A. Fukuda, Y. Takanishi, T. Isozaki, K. Ishikawa, and H. Takezoe, "Antiferroelectric chiral smectic liquid crystals," *J. Mater. Chem.*, vol. 4, pp. 997–1016, 1994.

[120] See Supplemental Material at http://link.aps.org/supplemental/10.1103/PhysRevE.95.042125 for extremely rich devil's staircase phase diagrams presented as four continuously and qualitatively changing videos.

[121] P. N. Timonin, "Ferrimagnetism of dilute Ising antiferromagnets," *Low Temperature Physics*, vol. 40, no. 1, pp. 36–41, 2014, http://dx.doi.org/10.1063/1.4850534.

[122] B. Derrida and G. Giacomin, "Log-periodic critical amplitudes: A perturbative approach," *Journal of Statistical Physics*, vol. 154, no. 1, pp. 286–304, 2014.

[123] M. F. Thorpe and R. B. Stinchcombe, "Two exactly soluble models of rigidity percolation," *Philosophical Transactions of the Royal Society of London A: Mathematical, Physical and Engineering Sciences*, vol. 372, no. 2008, 2013, http://rsta.royalsocietypublishing.org/content/372/2008/20120038.full.pdf.

[124] A. Efrat and M. Schwartz, "Lack of self-averaging in random systems–liability or asset?," *Physica A: Statistical Mechanics and its Applications*, vol. 414, pp. 137 – 142, 2014.

[125] C. Monthus and T. Garel, "Zero-temperature spin-glass–ferromagnetic transition: Scaling analysis of the domain-wall energy," *Phys. Rev. B*, vol. 89, p. 184408, May 2014.

[126] T. Nogawa and T. Hasegawa, "Transition-type change between an inverted Berezinskii-Kosterlitz-Thouless transition and an abrupt transition in bond percolation on a random hierarchical small-world network," *Phys. Rev. E*, vol. 89, p. 042803, Apr 2014.

[127] M. L. Lyra, F. A. B. F. de Moura, I. N. de Oliveira, and M. Serva, "Bose-einstein condensation in diamond hierarchical lattices," *Phys. Rev. E*, vol. 89, p. 052133, May 2014.

[128] V. Singh and S. Boettcher, "Scaling of clusters near discontinuous percolation transitions in hyperbolic networks," *Phys. Rev. E*, vol. 90, p. 012117, Jul 2014.

[129] Y.-L. Xu, X. Zhang, Z.-Q. Liu, X.-M. Kong, and T.-Q. Ren, "Robust thermal quantum correlation and quantum phase transition of spin system on fractal lattices," *The European Physical Journal B*, vol. 87, no. 6, p. 132, 2014.

[130] Y. Hirose, A. Oguchi, and Y. Fukumoto, "Infinitely multiple steps in magnetization of ferro- and antiferromagnetic Ising models with frustration on a diamond hierarchical lattice," *Journal of the Physical Society of Japan*, vol. 83, no. 7, p. 074716, 2014, http://dx.doi.org/10.7566/JPSJ.83.074716.

[131] V. S. T. Silva, R. F. S. Andrade, and S. R. Salinas, "Annealed Ising model with site dilution on self-similar structures," *Phys. Rev. E*, vol. 90, p. 052112, Nov 2014.

[132] Y. Hotta, "Self-avoiding walk on fractal complex networks: Exactly solvable cases," *Phys. Rev. E*, vol. 90, p. 052821, Nov 2014.

[133] S. Boettcher, S. Falkner, and R. Portugal, "Relation between random walks and quantum walks," *Phys. Rev. A*, vol. 91, p. 052330, May 2015.

[134] S. Boettcher and C. T. Brunson, "Classification of critical phenomena in hierarchical small-world networks," *EPL (Europhysics Letters)*, vol. 110, no. 2, p. 26005, 2015.

[135] Y. Hirose, A. Oguchi, and Y. Fukumoto, "Elucidation of ground-state spin configurations of Ising models in a magnetic field with frustration on a diamond hierarchical lattice," *Journal of the Physical Society of Japan*, vol. 84, no. 10, p. 104705, 2015, http://dx.doi.org/10.7566/JPSJ.84.104705.

[136] S. Boettcher and S. Li, "Real-space renormalization group for spectral properties of hierarchical networks," *Journal of Physics A: Mathematical and Theoretical*, vol. 48, no. 41, p. 415001, 2015.

[137] A. Nandy and A. Chakrabarti, "Engineering flat electronic bands in quasiperiodic and fractal loop geometries," *Physics Letters A*, vol. 379, no. 43âĂŞ44, pp. 2876 – 2882, 2015.

[138] Ç. Yunus, B. Renklioğlu, M. Keskin, and A. N. Berker, "Stepwise positional-orientational order and the multicritical-multistructural global phase diagram of the $s = 3/2$ Ising model from renormalization-group theory," *Phys. Rev. E*, vol. 93, p. 062113, Jun 2016.

[139] A. N. Berker, "Critical interactions for the triangular spin-s Ising model by a spin-restructuring transformation," *Phys. Rev. B*, vol. 12, pp. 2752–2758, Oct 1975.

[140] A. N. Berker and M. Wortis, "Blume-Emery-Griffiths-Potts model in two dimensions: Phase diagram and critical properties from a position-space renormalization group," *Phys. Rev. B*, vol. 14, pp. 4946–4963, Dec 1976.

[141] B. Nienhuis, A. N. Berker, E. K. Riedel, and M. Schick, "First- and second-order phase transitions in Potts models: Renormalization-group solution," *Phys. Rev. Lett.*, vol. 43, pp. 737–740, Sep 1979.

[142] D. Andelman and A. N. Berker, "q-state Potts models in d dimensions: Migdal-Kadanoff approximation," *Journal of Physics A: Mathematical and General*, vol. 14, no. 4, p. L91, 1981.

[143] A. N. Berker and D. R. Nelson, "Superfluidity and phase separation in helium films," *Phys. Rev. B*, vol. 19, pp. 2488–2503, Mar 1979.

[144] M. S. Cao and J. Machta, "Migdal-Kadanoff study of the random-field Ising model," *Phys. Rev. B*, vol. 48, pp. 3177–3182, Aug 1993.

[145] A. Falicov, A. N. Berker, and S. R. McKay, "Renormalization-group theory of the random-field Ising model in three dimensions," *Phys. Rev. B*, vol. 51, pp. 8266–8269, Apr 1995.

[146] K. Hui and A. N. Berker, "Random-field mechanism in random-bond multicritical systems," *Phys. Rev. Lett.*, vol. 62, pp. 2507–2510, May 1989.

[147] K. Hui and A. N. Berker, "Random-field mechanism in random-bond multicritical systems," *Phys. Rev. Lett.*, vol. 63, pp. 2433–2433, Nov 1989.

[148] M. Hinczewski and A. N. Berker, "Finite-temperature phase diagram of nonmagnetic impurities in high-temperature superconductors using a $d = 3$ tj model with quenched disorder," *Phys. Rev. B*, vol. 78, p. 064507, Aug 2008.

[149] H. Saleur, "The antiferromagnetic Potts model in two dimensions: Berker-Kadanoff phase, antiferromagnetic transition, and the role of Beraha numbers," *Nuclear Physics B*, vol. 360, no. 2, pp. 219 – 263, 1991.

[150] J. L. Jacobsen, J. Salas, and A. D. Sokal, "Spanning forests and the q-state Potts model in the limit q →0," *Journal of Statistical Physics*, vol. 119, no. 5, pp. 1153–1281, 2005.

[151] J. L. Jacobsen and H. Saleur, "The antiferromagnetic transition for the square-lattice Potts model," *Nuclear Physics B*, vol. 743, no. 3, pp. 207 – 248, 2006.

[152] Y. Ikhlef, "The antiferromagnetic Potts model," *Modern Physics Letters B*, vol. 25, no. 05, pp. 291–313, 2011, http://www.worldscientific.com/doi/pdf/10.1142/S0217984911025766.

[153] J. L. Jacobsen and C. R. Scullard, "Critical manifold of the kagome-lattice Potts model," *Journal of Physics A: Mathematical and Theoretical*, vol. 45, no. 49, p. 494003, 2012.

[154] J. L. Jacobsen and J. Salas, "A generalized Beraha conjecture for non-planar graphs," *Nuclear Physics B*, vol. 875, no. 3, pp. 678 – 718, 2013.

[155] C. R. Scullard and J. L. Jacobsen, "Potts-model critical manifolds revisited," *Journal of Physics A: Mathematical and Theoretical*, vol. 49, no. 12, p. 125003, 2016.

[156] R. Bondesan, S. Caracciolo, and A. Sportiello, "Critical behaviour of spanning forests on random planar graphs," *Journal of Physics A: Mathematical and Theoretical*, vol. 50, no. 7, p. 074003, 2017.

[157] J. Jacobsen, J. Salas, and C. Scullard, "Phase diagram of the triangular-lattice Potts antiferromagnet," *Journal of Physics A: Mathematical and Theoretical*, 2017.

[158] P. Bak and J. von Boehm, "Ising model with solitons, phasons, and "the devil's staircase"," *Phys. Rev. B*, vol. 21, pp. 5297–5308, Jun 1980.

[159] J. Marshall, V. Martin-Mayor, and I. Hen, "Practical engineering of hard spin-glass instances," *Phys. Rev. A*, vol. 94, p. 012320, Jul 2016.

[160] T. Çağlar and A. N. Berker, "Devil's staircase continuum in the chiral clock spin glass with competing ferromagnetic-antiferromagnetic and left-right chiral interactions," *Phys. Rev. E*, vol. 95, p. 042125, Apr 2017.

[161] Š. J. Širca and M. Omladič, "The JLS model with ARMA/GARCH errors," *Ars Mathematica Contemporanea*, vol. 13, no. 1, pp. 63–79, 2016.

[162] A. N. Berker, "Ordering under random fields: Renormalization-group arguments," *Phys. Rev. B*, vol. 29, pp. 5243–5245, May 1984.

Tolga Çağlar was born in Bursa, on June $18^{th}, 1987$. During his undergraduate studies at Koç University between 2007 and 2011, he was awarded full scholarship for his success in the university entrance exams. He started his academic career after completing the intensive course on phase transitions and renormalization-group theory, which was instructed by his future PhD thesis advisor, Prof. A. Nihat Berker, in July of 2008. After his graduation, he continued his research as a PhD candidate at Sabancı University, under Prof. Berker's supervision. Between 2011 and 2017, he published four articles in the *Physical Review E*, and another one was submitted before his dissertation defense. During his graduate studies, he presented his works in nine short talks (five of which are international) and one invited talk. He also worked as a teaching assistant in various undergraduate/graduate courses, including the courses with 'active learning', which are recently adapted to Sabancı University's curriculum. In June 22, 2017, he was awarded the Dr. Gürsel Sönmez Research Award for coming into prominence with outstanding research. Starting in September 2017, he is continuing his research on microbial ecosystems as a postdoctoral researcher, with the MIT led Simons Foundation collaboration, THE-ME, at the University of California San Diego.